



**BUILD UP AND OPERATION OF AN AXIAL TURBINE DRIVEN BY A
ROTARY DETONATION ENGINE**

THESIS

Jonathan R. Tellefsen, Second Lieutenant, USAF

AFIT/GAE/ENY/12-M39

**DEPARTMENT OF THE AIR FORCE
AIR UNIVERSITY**

AIR FORCE INSTITUTE OF TECHNOLOGY

Wright-Patterson Air Force Base, Ohio

APPROVED FOR PUBLIC RELEASE; DISTRIBUTION UNLIMITED

The views expressed in this thesis are those of the author and do not reflect the official policy or position of the United States Air Force, Department of Defense, or the United States Government. This material is declared a work of the U.S. Government and is not subject to copyright protection in the United States.

AFIT/GAE/ENY/12-M39

**BUILD UP AND OPERATION OF AN AXIAL TURBINE DRIVEN BY A
ROTARY DETONATION ENGINE**

THESIS

Presented to the Faculty

Department of Aeronautics and Astronautics

Graduate School of Engineering and Management

Air Force Institute of Technology

Air University

Air Education and Training Command

In Partial Fulfillment of the Requirements for the
Degree of Master of Science in Aeronautical Engineering

Jonathan R. Tellefsen

Second Lieutenant, USAF

March 2012

APPROVED FOR PUBLIC RELEASE; DISTRIBUTION UNLIMITED

**BUILD UP AND OPERATION OF AN AXIAL TURBINE DRIVEN BY A
ROTARY DETONATION ENGINE**

Jonathan R. Tellefsen

Second Lieutenant, USAF

Approved:

Paul I. King (Chairman)

Date

Frederick R. Schauer (Member)

Date

Captain Jay Rutledge (Member)

Date

Abstract

Detonation combustors provide advantages over current deflagration combustors due to their pressure gain and simplicity of design. Rotary detonation engines (RDEs) offer advantages over pulsed detonation engines (PDEs) due to a steadier exhaust and fewer total system losses. All previous research on turbine integration with detonation combustors has focused on utilizing PDEs to drive axial and centrifugal turbines. The objective of this thesis was the integration and testing of an axial turbine driven by a rotary detonation engine (RDE) to determine turbine operability. In pursuit of this objective, convergent nozzle sections were placed on the RDE to simulate the back-pressurization that would occur when placing the turbine behind the RDE. Nozzle testing showed that back-pressurizing the RDE increases the operational space of the RDE. Results from the nozzle testing were used to properly integrate the turbine with the RDE. The turbine was driven by the RDE with successful detonation runs, showing turbine operation with RDEs is possible. The RDE operated similarly for both nozzle and turbine testing, demonstrating that a nozzle can properly simulate the presence of a turbine behind a RDE.

Acknowledgments

I would first like to thank Dr. Fred Schauer for allowing me to work down in D-Bay during my time as an AFIT student. Working in D-Bay was fun and challenging at the same time (a difficult feat to accomplish) and the experiences and knowledge I gained will stay with me throughout my career. I would also like to thank Dr. Paul King, my thesis advisor, for his constant support and hours dedicated to discussing my project and helping me to interpret my results.

Special thanks to everyone in D-Bay who helped me finish this research project: Dr. John Hoke for all his help providing oversight on my research project; Rich Ryman, Justin Goffena, and Benjamin Naguy for helping with all of the welding, cutting, and shaping that went into the turbine plenum design; Curtis Rice for all the help with the experimental setup and testing; Andy Naples for designing the control program for the turbine and always having a joke about Jason; Brian, Rachel, and Chris for answering my myriad of questions; and last but certainly not least my compatriots Lt Jason Shank and Maj Lou Camardo for all their help and support as we tackled our projects together.

Mark Fernelius also played a pivotal role in my thesis by providing the CAD model for the circular plenum.

To 212, 214, and my Bible study group, thank you for all your support and keeping me sane over the past 18 months with all of the great times together (especially ping-pong and Super Smash Bros). Final thanks to my parents and siblings for all their loving support throughout my time at AFIT.

Jonathan Tellefsen

Table of Contents

Abstract.....	iv
Acknowledgments.....	v
List of Figures.....	ix
List of Tables.....	xviii
Nomenclature.....	xx
List of Abbreviations.....	xx
List of Symbols.....	xx
I. Introduction.....	1
Chapter Summary.....	2
II. Background and Previous Work.....	3
1. Background.....	3
2. Previous Research.....	6
III. Test Setup and Methodology.....	14
1. Facility.....	14
2. Engine Setup.....	15
3. Experimental Setups.....	20
A. 1.5 in and 1.17 in Nozzle Setup.....	20
B. Turbine Build Up and Experimental Setup.....	23
4. Data Collection.....	36
5. Data Reduction.....	36
A. PCB Wave Speed Sensitivity.....	36
B. Kulite Wave Speed Sensitivity.....	37
C. Linear Sensitivity.....	40
D. PCB Aliasing.....	44
E. PCB and Kulite Data Comparison.....	47
F. Chosen Data Reduction Values.....	49
G. Kulite Peak Pressures.....	50
H. Turbine Testing.....	51
6. Uncertainty.....	51
IV. Results.....	54

1. 1.5 in. Nozzle Testing	54
A. Kulite Pressure.....	54
B. Operational Space	55
C. Wave Speed Trends	57
D. RDE Start Up Transients	58
E. Turbine Integration.....	59
2. 1.17 in. Nozzle Testing	60
A. Detonation Channel Pressure.....	60
B. Operational Space	62
C. Wave Speed Trends	65
D. Nozzle Pressures.....	68
E. Turbine Integration.....	71
3. Turbine Testing	73
A. Cold Flow Testing	73
B. Operational Space	73
C. Wave Speed Trends	75
D. Turbine Pressures.....	75
E. Engine RPM.....	80
F. Catastrophic Failure	81
V. Conclusions.....	84
Future Work	86
Appendix A. Sensitivity Analysis.....	88
1. Linear Sensitivity	88
2. Sensitivity Analysis Data	91
3. Kulite and PCB Data Comparison	93
4. Turbine Data PCB sensitivity.....	96
Appendix B. Uncertainty	98
Appendix C. Shock Diamond Analysis	103
Appendix D. Catastrophic Failure Data.....	105
Appendix E. Thermocouple Data	109
Appendix F. Test Matrices.....	111

Appendix G. Turbine Testing Data.....	117
References.....	Error! Bookmark not defined.

List of Figures

Figure 1. Comparison of Brayton and Humphrey engine cycles on a T-s diagram.....	1
Figure 2. Engine cycle of a pulsed detonation engine	4
Figure 3. Fire sequence for operation of a rotary detonation engine	5
Figure 4. Schematic of the rotating detonation wave structure for an unwrapped view of an annulus (12).....	10
Figure 5. Outlet pressure and temperature for a 1.5 m circumference RDE with an H ₂ -air mixture at standard, stoichiometric conditions (12)	11
Figure 6. Cross-sections of converging-diverging nozzle configurations (14).....	12
Figure 7. Three in. rotary detonation engine.....	15
Figure 8. Propellant delivery system for 3 in. RDE rig	17
Figure 9. Standard run profile for pressures upstream and downstream of the air and hydrogen sonic nozzles	19
Figure 10. Experimental setup for 1.5 in. convergent nozzle on RDE	21
Figure 11. Experimental setup for 1.17 in. convergent nozzle on RDE	22
Figure 12. New circular plenum adapter for JetCat compressor and turbine	24
Figure 13. JetCat P-200 with the inlet, outer casing and nozzle removed.....	25
Figure 14. JetCat P-200 with the compressor stator vanes milled flush with the flow conditioner and the combustor and nozzle flange removed	26
Figure 15. JetCat with the inner jacket, compressor backing, plenum cap, and bearing lubricant line.....	27
Figure 16. JetCat position with respect to the circular plenum.....	28
Figure 17. Plenum disc used to stabilize and support the centrifugal compressor housing.....	29

Figure 18. Experimental setup for JetCat turbine testing using the 3 in. RDE.....	30
Figure 19. Turbine measurement locations for the JetCat turbine experiment.....	32
Figure 20. Schematic of plenum chamber showing dimensions and locations of turbine inlet measurements for turbine-RDE testing.....	33
Figure 21. Schematic of JetCat nozzle with dimensions and locations of turbine outlet measurements for turbine-RDE testing.....	33
Figure 22. Garrett speed sensor (used with permission by Garrett)	34
Figure 23. Lubricant delivery system to JetCat bearings for turbine testing.....	35
Figure 24. PCB average wave speed sensitivity analysis for variations in threshold, time hold, and points above the threshold.....	37
Figure 25. Kulite average wave speed sensitivity analysis for variations in the threshold, time holds, and points above the threshold	38
Figure 26. Wave speeds for PCB from time of flight code for 100 μ s hold time, 1 standard deviation threshold, and 3 points above threshold.....	39
Figure 27. Wave Speeds for Kulite from time of flight code for a 1 standard deviation threshold, a 120 μ s hold time, and 3 points above threshold	40
Figure 28. PCB pressure sensor data for a run with successful detonations.....	40
Figure 29. Four line linear fit of PCB data used to normalize PCB data.....	41
Figure 30. Sensitivity of PCB wave speed calculations to the number of linear equations created to normalize the data	42
Figure 31. Kulite pressure transducer data for a run with successful detonations.....	43
Figure 32. Sensitivity of Kulite wave speed calculations to the number of linear equations created to normalize the data.....	43

Figure 33. Points above threshold sensitivity analysis for wave speed velocities of Kulite and PCB data using a hold time of 120 μ s and a hold time of 1 standard deviation	44
Figure 34. Zoomed in view of PCB data with wave speed calculation variables.....	45
Figure 35. Histogram showing high speed detonation aliasing for a threshold of 1 standard deviation, a points above threshold of 1, and a hold time of 120 μ s.....	46
Figure 36. Kulite and PCB data comparison	47
Figure 37. Histogram of detonation wave speeds for a threshold of 1 standard deviation, a points above threshold of 2, and a hold time of 120 μ s	49
Figure 38. Peak pressures of Kulite data for the RDE run at $m=46.1$ and $\phi=1.07$ with the 1.5 in. nozzle installed.....	50
Figure 39. Kulite pressure data for unmodified RDE operation at $m=48.0$ lbm/min and $\phi=1.4$.	54
Figure 40. Kulite pressure data for RDE operated with 1.5 in. convergent nozzle at $m=48.5$ lbm/min and $\phi=1.02$	54
Figure 41. RDE operational map using 23% oxygen enriched air and hydrogen (2).....	55
Figure 42. RDE with 1.5 in. diameter convergent nozzle operating map using 23% oxygen enriched air	56
Figure 43. Dependence of average wave speed on equivalence ratio for successful detonation runs for the 1.5 in. nozzle using enriched air	57
Figure 44. High speed camera comparison of startup and steady operation for the 3 in. RDE with 1.5 in. nozzle	58
Figure 45. Video recording comparison of startup and steady operation for the 3 in. RDE with 1.5 in. nozzle	59

Figure 46. Pressure transducer 0.70 in. from detonation channel bottom for 1.17 in. nozzle testing using standard air at $m=42.4$ lbm/min and $\phi=1.06$	60
Figure 47. Total mass flow rate impact on average detonation channel pressure for 1.17 in. nozzle testing using standard air	61
Figure 48. RDE operating map with 1.17 in. diameter convergent nozzle section using standard air	62
Figure 49. RDE operating range for hydrogen and standard air	62
Figure 50. Fuel flow rate limit for the RDE with the 1.17 in. convergent nozzle run with standard air and hydrogen.....	64
Figure 51. RDE operating range for hydrogen-air with 6mm channel and 0.123 in ² gross oxidizer injection area with a defined transition (13)	64
Figure 52. Average wave speed dependence on the total mass flow rate, equivalence ratio, and the percentage of oxygen used for testing.....	65
Figure 53. Impact of equivalence ratio on RDE performance for 1.17 in. nozzle using standard air and hydrogen.....	66
Figure 54. Wave speed 51 point moving average for successful detonation RDE runs with the 1.17 in. convergent nozzle and standard air	67
Figure 55. Wave speed 51 point moving average profile for partial detonation RDE runs with the 1.17 in. convergent nozzle and standard air	68
Figure 56. Nozzle base and throat pressures at $m=34.3$ lbm/min and $\phi=1.15$	69
Figure 57. Pressure trends for RDE detonation channel and 1.17 in. nozzle in the detonation channel and at the nozzle base and nozzle exit.....	70
Figure 58. Turbine runs compared with 1.17 in. and 1.5 in. nozzle operational spaces.....	74

Figure 59. Comparison of turbine, 1.5 in. nozzle, and 1.17 in. nozzle average wave speeds	75
Figure 60. Compressor and turbine inlet and outlet pressures for a RDE-turbine run at $m=39.8$ lbm/min and $\phi=1.38$	76
Figure 61. Turbine pressures using a 150 point moving average and compressor pressure measurements for turbine-RDE testing at $m=39.8$ lbm/min and $\phi=1.38$	77
Figure 62. Turbine inlet and outlet pressure comparison with 1.17 in. nozzle pressure data.....	78
Figure 63. Compressor performance relation to turbine inlet pressure produced by RDE.....	79
Figure 64. Compressor pressure ratio dependence on RDE and compressor mass flow rate.....	80
Figure 65. Comparison of unprocessed RPM data with RPM data using a 150 point moving average at $m=39.8$ lbm/min and $\phi=1.38$	80
Figure 66. Comparison of the JetCat turbine before and after the catastrophic failure	82
Figure 67. RPM 150 point moving average for catastrophic failure at $m=41.8$ lbm/min and $\phi=1.31$	82
Figure 68. Velocity Histogram for PCB data for data reduction using 2 linear equations to normalize data	88
Figure 69. Velocity Histogram for PCB data for data reduction using 10 linear equations to normalize data	88
Figure 70. Velocity Histogram for PCB data for data reduction using 100 linear equations to normalize data2 Line Data Reduction of PCB data	89
Figure 71. Velocity Histogram for PCB data for data reduction using 200 linear equations to normalize data2 Line Data Reduction of PCB data	89
Figure 72. Velocity histogram for Kulite data for a $m=48.3$ lbm/min and $\phi=0.87$ for a threshold of 1 standard deviation, a time hold of 120 μ s, and a PAT of 4	93

Figure 73. Velocity histogram for PCB data for a $m=48.3$ lbm/min and $\phi=0.87$ for a threshold of 1 standard deviation, a time hold of 100 μ s, and a PAT of 4.....	93
Figure 74. Average wave speed histogram for a threshold of 1 standard deviation, a points above threshold of 2, and a hold time of 120 μ s.....	96
Figure 75. Average wave speed histogram for a threshold of 1 standard deviation, a points above threshold of 1, and a hold time of 120 μ s.....	97
Figure 76. Average wave speed histogram for a points above the threshold value of 2 for a threshold of 1 standard deviation and a points above threshold of 1 for a threshold of 2 standard deviations, both using a hold time of 120 μ s.....	97
Figure 77. Kulite pressure total sample uncertainty represented via error bars.....	98
Figure 78. Turbine inlet total sample uncertainty represented via error bars	98
Figure 79. Turbine outlet pressure total sample uncertainty represented via error bars.....	99
Figure 80. Compressor outlet total sample pressure uncertainty represented via error bars	99
Figure 81. Compressor inlet pressure uncertainty represented via error bars.....	100
Figure 82. Wave structures and shock diamonds in an underexpanded flow (20)	103
Figure 83. RPM data and 150 point moving average of RPM data for turbine catastrophic failure	105
Figure 84. Compressor mass flow rate for turbine catastrophic failure.....	105
Figure 85. Compressor inlet and outlet pressures for turbine catastrophic failure	106
Figure 86. Turbine inlet and outlet pressures for turbine catastrophic failure.....	106
Figure 87. Averaged Turbine inlet and outlet pressures for turbine catastrophic failure	107
Figure 88. Initial turbine inlet temperature for every run conducted on the day of the catastrophic failure	108

Figure 89. Maximum turbine inlet temperature reading for 1 and 2 second turbine runs using both standard and enriched air	109
Figure 90. Compressor and turbine inlet and outlet temperatures for a 1 second, standard air run at $m=23.8$ lbm/min and $\phi=1.37$	110
Figure 91. Compressor and turbine inlet and outlet temperatures for a 2 second, standard air run at $m=28.5$ lbm/min and $\phi=1.47$	110
Figure 92. Compressor and turbine inlet and outlet temperatures for a 1 second, enriched air run at $m=39.8$ lbm/min and $\phi=1.38$	110
Figure 93. RPM 150 point moving average and compressor mass flow rate 100 point moving average for a 2 second, standard air run at $m=24.8$ lbm/min and $\phi=1.7$	117
Figure 94. Compressor inlet and outlet pressures and 150 point moving average of turbine inlet and outlet pressures for a 2 second, standard air run at $m=24.8$ lbm/min and $\phi=1.7$	117
Figure 95. RPM 150 point moving average and compressor mass flow rate 100 point moving average for a 2 second, standard air run at $m=28.5$ lbm/min and $\phi=1.47$	117
Figure 96. Compressor inlet and outlet pressures and 150 point moving average of turbine inlet and outlet pressures for a 2 second, standard air run at $m=28.5$ lbm/min and $\phi=1.47$	118
Figure 97. RPM 150 point moving average and compressor mass flow rate 100 point moving average for a 1 second, enriched air run at $m=31.4$ lbm/min and $\phi=0.94$	118
Figure 98. Compressor inlet and outlet pressures and 150 point moving average of turbine inlet and outlet pressures for a 1 second, enriched air run at $m=31.4$ lbm/min and $\phi=0.94$	118

Figure 99. RPM 150 point moving average and compressor mass flow rate 100 point moving average for a 1 second, enriched air run at $m=30.9$ lbm/min and $\phi=1.13$	119
Figure 100. Compressor inlet and outlet pressures and 150 point moving average of turbine inlet and outlet pressures for a 1 second, enriched air run at $m=30.9$ lbm/min and $\phi=1.13$	119
Figure 101. RPM 150 point moving average and compressor mass flow rate 100 point moving average for a 1 second, enriched air run at $m=31.4$ lbm/min and $\phi=1.3$	119
Figure 102. Compressor inlet and outlet pressures and 150 point moving average of turbine inlet and outlet pressures for a 1 second, enriched air run at $m=31.4$ lbm/min and $\phi=1.3$ 120	
Figure 103. RPM 150 point moving average and compressor mass flow rate 100 point moving average for a 1 second, enriched air run at $m=35.5$ lbm/min and $\phi=1.27$	120
Figure 104. Compressor inlet and outlet pressures and 150 point moving average of turbine inlet and outlet pressures for a 1 second, enriched air run at $m=35.5$ lbm/min and $\phi=1.27$	120
Figure 105. RPM 150 point moving average and compressor mass flow rate 100 point moving average for a 1 second, enriched air run at $m=36.6$ lbm/min and $\phi=1.33$	121
Figure 106. Compressor inlet and outlet pressures and 150 point moving average of turbine inlet and outlet pressures for a 1 second, enriched air run at $m=36.6$ lbm/min and $\phi=1.33$	121
Figure 107. RPM 150 point moving average and compressor mass flow rate 100 point moving average for a 1 second, enriched air run at $m=37.9$ lbm/min and $\phi=1.28$	121

Figure 108. Compressor inlet and outlet pressures and 150 point moving average of turbine inlet and outlet pressures for a 1 second, enriched air run at $m=37.9$ lbm/min and $\phi=1.28$

..... 122

Figure 109. RPM 150 point moving average and compressor mass flow rate 100 point moving average for a 1 second, enriched air run at $m=41.1$ lbm/min and $\phi=1.34$ 122

Figure 110. Compressor inlet and outlet pressures and 150 point moving average of turbine inlet and outlet pressures for a 1 second, enriched air run at $m=41.1$ lbm/min and $\phi=1.34$

..... 122

List of Tables

Table 1. Propellant feed pressures for 3 in. RDE rig.....	16
Table 2. Area ratios for convergent nozzles placed on RDE.....	20
Table 3. Values used in time of flight code for wave speed data reduction	49
Table 4. Bias uncertainty values for pressure transducers used during testing	51
Table 5. PCB data linear normalization sensitivity analysis for MATLAB time of flight code ..	90
Table 6. Kulite data linear normalization sensitivity analysis for MATLAB time of flight code	90
Table 7. PCB Sensitivity Analysis Data	91
Table 8. Kulite Sensitivity Analysis Data	92
Table 9. Percent Difference between the Kulite and the PCB values of wave speed for a points above threshold value of 4 for the PCB	94
Table 10. Percent Difference between the Kulite and the PCB values of wave speed for a points above threshold value of 2 for the PCB	95
Table 11. 1.5 in. nozzle Kulite average wave speed error	100
Table 12. Nozzle PCB data average wave speed error	101
Table 13. Turbine PCB data error and scan rate.....	102
Table 14. Flow properties for Shock Diamond expansions and oblique shocks	104
Table 15. Kulite data test matrix for 1.5 in. nozzle testing.....	111
Table 16. PCB data test matrix for 1.5 in. nozzle testing	112
Table 17. PCB and average detonation channel pressure data test matrix for 1.17 in. nozzle testing.....	113
Table 18. PCB and nozzle pressure data test matrix for 1.17 in. nozzle testing.....	114
Table 19. PCB and RPM data for turbine testing	115

Table 20. Compressor inlet and outlet pressures, compressor mass flow rate, and turbine inlet and outlet pressure for turbine testing.....	116
---	-----

Nomenclature

List of Abbreviations

AFRL	Air Force Research Lab
C-J	Chapman-Juguet
DDT	Deflagration-to-detonation transition
DERF	Detonation Engine Research Facility
FS	Full scale
MAF	Mass air flow
NPSS	Numerical Propulsion Systems Simulation
PAT	Points above the threshold
PDC	Pulsed detonation combustor
PDE	Pulsed detonation engine
RDE	Rotary detonation engine
RPM	Revolutions per minute
SDC	Steady deflagration combustion
TSFC	Thrust specific fuel consumption

List of Symbols

A	Area
D	Diameter
h	Specific enthalpy
M	Mach number
n	Number of measurements
P	Pressure
P_t	Total pressure
P_{amb}	Ambient pressure
P_{sample}	Sample precision Error
P_{mean}	Mean precision Error
P_t	Total pressure
P_{th}	Throat pressure
R	Universal gas constant
S_x	Sample standard deviation
t	t-distribution value
T	Temperature
T_t	Total temperature
U_{bias}	Bias error
$U_{precision}$	Precision error
U_{Total}	Total error
V	Velocity
\dot{m}	Mass flow rate (lbm/min)
Φ	Equivalence ratio
γ	Ratio of specific heats

BUILD UP AND OPERATION OF AN AXIAL TURBINE DRIVEN BY A ROTARY DETONATION ENGINE

I. Introduction

Deflagration serves as the primary mode of combustion in the modern world, from the internal combustion engine used in vehicles to the turbofan engine employed in aircraft. After many years of research and development, further improvements in deflagration engines have become more difficult to attain, bringing about an interest in new combustion techniques that can revolutionize current engine cycles.

Pressure gain combustion produces less entropy than constant pressure combustion while providing the same performance. A comparison of the Brayton cycle, the standard gas turbine engine cycle using constant pressure combustion, and the Humphrey cycle, the pressure gain combustion cycle, is shown in Figure 1.

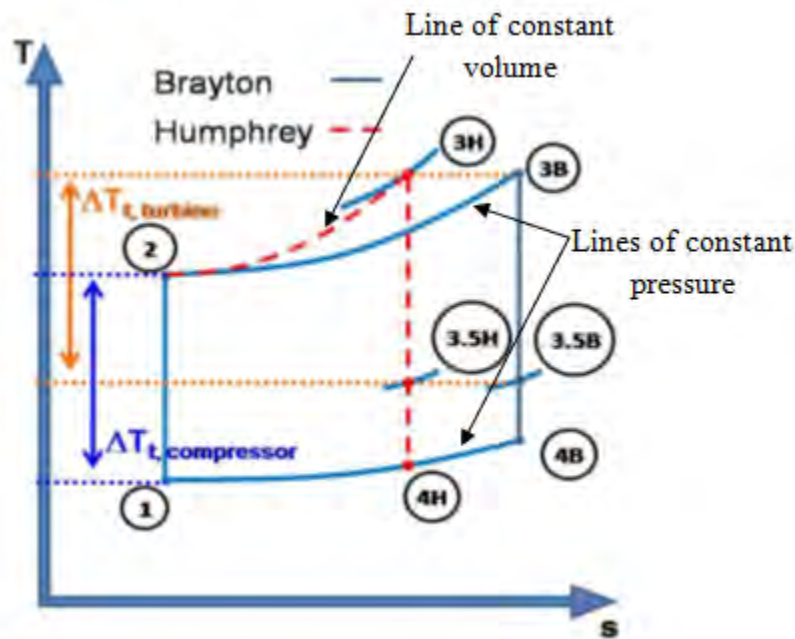


Figure 1. Comparison of Brayton and Humphrey engine cycles on a T-s diagram

The Brayton cycle in Figure 1 combusts along the line of constant pressure from point 2 to 3B, but the Humphrey cycle pressure increases due to the pressure gain combustion, reaching the intended temperature at point 3H on a higher pressure line than the Brayton cycle, resulting in a lower entropy state. Because of the potential benefits of increased thermal efficiency and decreased entropy, it is desired to incorporate pressure gain combustion systems with current gas-turbine engine technology. The rotary detonation engine (RDE) and the pulsed detonation engine (PDE) provide pressure gain combustion by the utilization of detonations.

The goal of this research was to investigate the operability of a turbine run by a RDE, since using the RDE to drive the turbine results in a Humphrey cycle for a gas-turbine engine due to the pressure gain of the RDE. Previous work examined the use of PDEs to power turbines, but no research has been performed on a turbine driven by a RDE, which offers advantages over the PDE in terms of mechanical simplicity and total system loss. This research focused on gathering quasi-steady state data of a radial compressor and axial turbine to determine the feasibility and benefits of incorporating an RDE with turbomachinery.

Chapter Summary

Chapter 2 contains a discussion on both PDEs and RDEs, and includes previous experimental and numerical research accomplished on PDE-turbine integration and RDE operation and performance. Chapter 3 covers the experimental procedure, test set-up, and data analysis techniques. Chapter 4 discusses the analysis and results of the experiments performed for this research. Chapter 5 states the conclusions of the research and offers recommendations on areas of future work.

II. Background and Previous Work

1. Background

A detonation is defined as a shock wave sustained by the energy released by combustion. The combustion process, in turn, is initiated by the shock wave compression and the resulting high temperatures. A detonation is similar to a normal shock because both are categorized by a pressure and temperature rise across the detonation front. For the inquisitive reader, detonation theory is explained by Turns (1) and Russo (2).

Petters and Felders (3) analyzed the possible benefits of pressure gain combustion using a Numerical Propulsion Systems Simulation (NPSS) program. A model embedded a pulse detonator combustor into the core of a high bypass turbofan, and simulated the modified engine at a cruise Mach number of 0.85 and an altitude of 35,000 ft. The results of the study showed that the modified turbofan had a 2% increase in thrust and an 11% reduction in thrust specific fuel consumption (TSFC) as compared to the conventional turbofan.

Because of the potential benefits of pressure gain combustion, much research has been accomplished in recent years utilizing PDE's for impulsive thrust as well as incorporating pressure gain combustion into the gas turbine engine cycle. Schauer et al. (4) and Glaser et al. (5) performed research on the incorporation of detonation based engines with turbomachinery, showing that a turbine can survive and perform similarly to a turbine run by deflagration. However, experimental research has yet to be performed on the feasibility of turbine integration with RDEs.

RDEs offer the same advantages of pressure gain combustion as PDEs with the added benefits of reduced complexity and fewer flow losses. PDEs create detonations by injecting reactants at the closed end of a tube, igniting the reactants to create a deflagration, and

developing the deflagration into a detonation using a deflagration to detonation transition (DDT) device. The detonation then travels down the tube to the open end, and new reactants are added at the closed end to repeat the process. A typical PDE engine cycle can be seen in Figure 2.



Figure 2. Engine cycle of a pulsed detonation engine

The three distinct phases of a PDE repeat in a cyclical nature, producing an unsteady flow at the tube exit with high peak pressures and temperatures during the fire phase followed by relatively low temperature and pressures during the purge and fill phases.

RDEs differ from PDEs in that RDEs utilize a detonation wave travelling transverse to the flow in an annulus. The detonation in an RDE only needs to be initiated once because the detonation wave travels transverse to the flow, as opposed to the PDE where the detonation flows through and out of the tube, requiring a DDT for every fire sequence. DDT is one of the largest sources of total system loss for detonation based engines, so reducing the number of

DDTs produces a more efficient engine. Additionally, since the RDE requires only one firing sequence, its frequencies of operation exist in the kHz range, whereas the PDE is limited to the Hertz range because of the need for a DDT during every ignition and the required minimum times of each phase (purge, fire, fill) in the PDC fire sequence. Higher frequencies lead to steadier exhaust that is beneficial for integration with turbomachinery.

RDEs are also less complex than PDEs because no moving parts are required. The PDE requires valves at the closed end of the tube to open and shut, bringing in fresh air and fuel that are used to produce each detonation. Thomas et al. (6) reported that the RDE overcomes this requirement by continuous filling of the region behind the detonation front with fresh reactants via open injectors; no valves are needed because the reactants operate under a favorable pressure gradient. The RDE operating cycle can be seen in Figure 3.

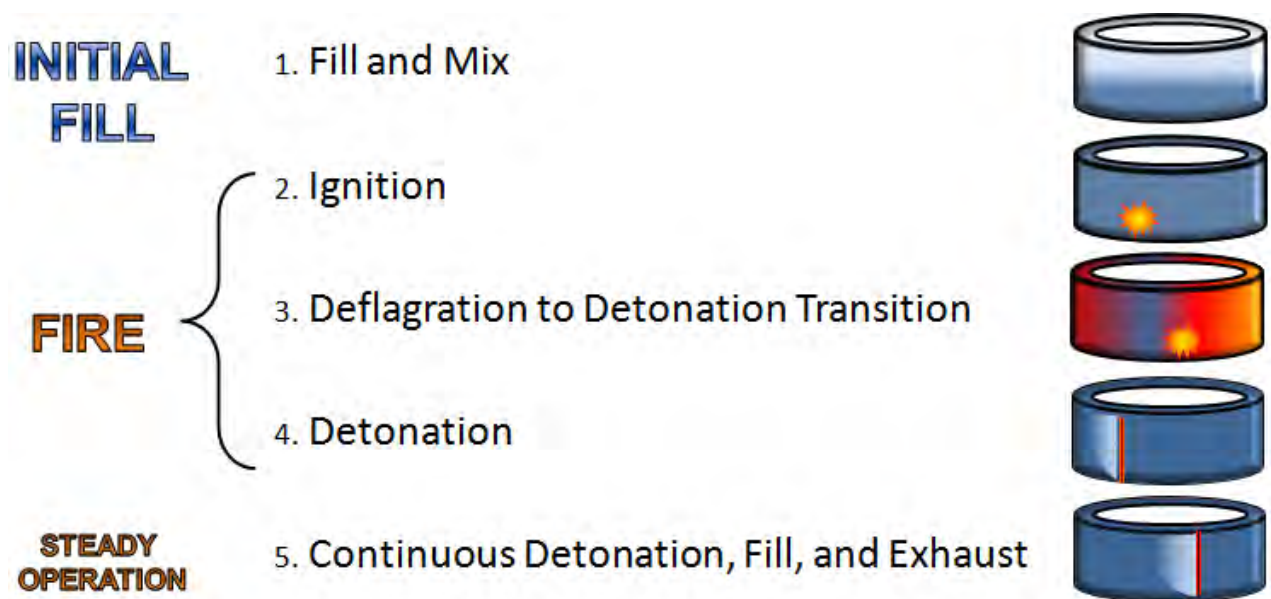


Figure 3. Fire sequence for operation of a rotary detonation engine

In Figure 3, the air and fuel travel axially, entering from the bottom and exhausting out the top, and are ignited by the detonation wave that travels transverse to the flow in the annulus. The thick red line in Figure 3 represents the detonation wave of the RDE travelling in the annulus.

2. Previous Research

Much research has been accomplished concerning the performance of turbines placed behind pulsed detonation combustors (PDCs). Schauer et al. (7) placed an automotive turbocharger behind two PDCs and ducted the compressor exit air flow to the PDCs to provide compressed air to the PDC inlet, making the system self-aspirated. A 25 minute self-aspirated run of the turbocharger was performed using this configuration with a 20% reduction in PDC thrust. The turbocharger turbine showed no pitting or signs of discoloration after the run, illustrating the survivability of a turbine driven by pulsed detonation. This research served as the building block for determining the ability of turbines to survive and operate in the unsteady environment of the PDC. Further work performed by Schauer et al. (4) analyzed more aspects of the flow properties as well as the turbine performance of the automotive turbocharger. The researchers placed dynamic pressure transducers along the detonation tube and the compressor flow of the turbocharger was measured upstream of the compressor with a mass air flow sensor. Results included pressure histories, wave speeds, thrust, and compressor power output. The turbine was run at nearly all significant conditions on the turbine map, including high pressure ratios and speeds of up to 135,000 RPM. The turbine experienced poor performance when run by the PDC, but since the turbine was not designed to be driven by pulsed detonation, the researchers concluded that the possibility existed to increase performance to existing levels in a gas turbine engine. The research performed by Schauer et al. (4) served as a gateway for continuing work conducted on turbines driven by detonation devices because it proved turbine

survivability and operability was achievable when running a turbine using the unsteady exhaust produced by detonations; the methodology of the experiment was followed closely for the current work, as similar measurements were taken to understand the operability of an axial turbine run by a RDE.

Research performed at the University of Cincinnati by Glaser, Caldwell, and Gutmark ((5); (8); (9)) looked at the performance of an axial turbine driven by a mixture of bypass and PDE exhaust gases. The researchers used a circular array of 6 PDC tubes run at up to 20 Hz. The bypass air was added at the end of the tubes and mixed with the PDC exhaust before entering the turbine. The percentage of PDC exhaust to bypass air ranged from 8% to 21%. The turbine was also driven by deflagration to make a comparison with the performance of the turbine when run using the PDCs and bypass air. The percentage of combusted products to bypass air ranged from 7.2% to 13.8%.

The turbine was connected to a torque cell and a water dynamometer was used to measure power. The turbine driven by the PDE and bypass air had comparable performance to the turbine driven by deflagration. The specific power and turbine efficiency increased when both the fill fraction and equivalence ratio were increased. The isentropic turbine efficiency was defined in this study as the ratio of actual work output to the ideal work output. The ideal work output was calculated by using the measured turbine inlet temperature and pressure ratio across the turbine section. Increases in operating frequency led to higher specific work from the turbine. The PDE driven turbine efficiencies compared favorably to the steady efficiencies of the turbine for the pressure ratio tested, providing incentive to pursue future work in the field.

The University of Cincinnati research relied on the use of bypass air to operate the turbine, and because of the low percentages of PDE exhaust gas to bypass air, the configuration

allowed for operation of the turbine nearer to a typical Brayton cycle; the study also used a dynamometer to measure turbine performance as opposed to a compressor. In the current work, the test set up utilized full admission of the RDE exhaust gases into the turbine and used a compressor as opposed to a dynamometer, since this is a more typical engine configuration, providing greater applicability to the results of the turbine testing.

Rouser et al. ((10); (11)) used a Garrett GT28 automotive turbocharger to determine the performance of a radial turbine using both full admission PDC and steady deflagration combustion (SDC). The important parameters to be determined in Rouser et al.'s study were power, specific power and specific fuel consumption. The researchers determined the power using compressor measurements because the compressor damped the impulses of the pulsed detonation engine, making the compressor relatively steady, although not completely steady.

The compressor specific work served as the primary performance characteristic analyzed for the experiment by Rouser et al. Testing revealed that specific work increased for an increase in equivalence ratio, up to an optimal value. Specific work also increased with operating frequency of the PDC, and increased frequency caused greater increases in specific work than changes in equivalence ratio. The compressor rotor achieved a quasi-steady behavior when increasing operational frequencies to 30 Hz. At approximately the same combustor inlet conditions, the specific work was calculated for the turbine driven both by SDC and PDC, and the PDC had a 41.3% improvement in specific work over SDC. Although the PDC has unsteady flow, the PDC power remained above the power extracted by the turbine driven by SDC for the entirety of the PDC cycle.

The current work integrated an axial turbine with a RDE, and since the previous research by Rouser et al. showed an increase in specific work with operating frequency, high values of specific work and a quasi-steady behavior were expected because of the high operational frequency of the RDE. Changes in equivalence ratio were used as a performance merit as was performed by Rouser et al. ((10); (11)).

The other type of pressure gain detonation engine currently being researched is the RDE. Thomas et al. (6) performed cold flow and combustion testing on an RDE rig at the Air Force Research Laboratory's (AFRL) Detonation Engine Research Facility (DERF). The researchers initiated a detonation in the RDE using a pre-detonator. The detonation transition from the pre-detonator to the main annulus was determined to be highly unsteady and an unpredictable event.

Turbines placed at the end of PDEs can experience maximum to minimum pressure ratios on the order of 20:1. An RDE, because the detonation wave travels around the annulus transverse to the flow direction, produces maximum to minimum pressure ratios of 5:1. The reduction of maximum to minimum pressure ratios provides another advantage for the RDE over the PDC when integrated with a turbine. Lower peak pressures produce a steadier flow, potentially allowing the turbine to operate nearer to a steady state condition.

Braun et al. (12) executed a computational cycle analysis to consider the performance of an RDE. The RDE has the potential to operate at a near steady state condition because the rotational frequency of the detonation wave around the annulus is in the range of 1-10 kHz. Because of this near steady state condition, the researchers using the computational cycle analysis assumed a steady RDE inlet and outlet. Braun et al. developed an unwrapped view of the detonation travelling around the annulus using the cycle analysis, as shown in Figure 4.

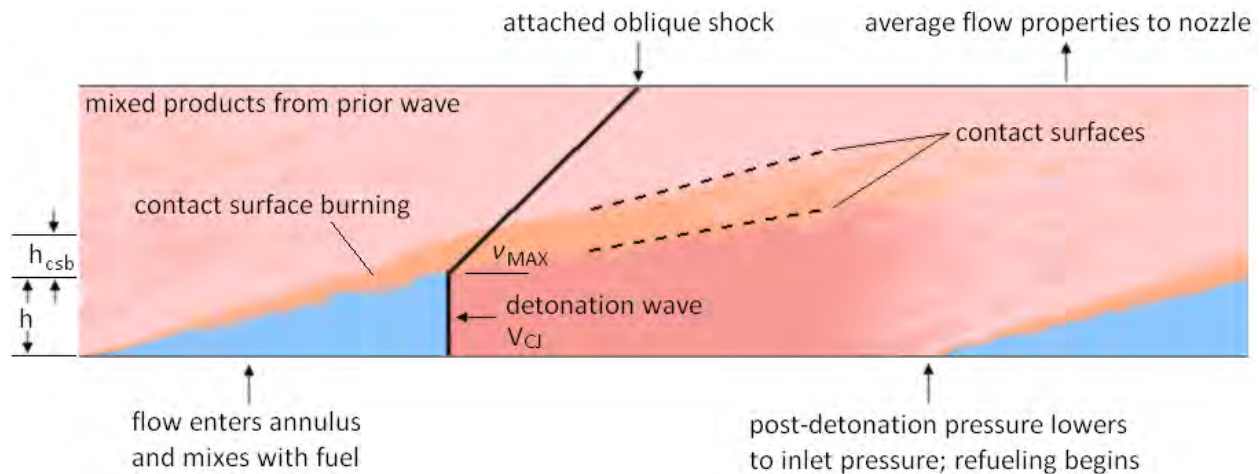


Figure 4. Schematic of the rotating detonation wave structure for an unwrapped view of an annulus (12)

The cycle analysis included a detonation wave propagating at the Chapman-Juguet (C-J) detonation velocity. An oblique shock resulted from the difference in the velocity of products from the current detonation and products of the previous detonation. Contact surface burning occurred between the fresh reactants and the hot products from the previous detonation.

Braun et al. (12) compared the detonation model with and without contact surface burning. The contact surface burning increased engine performance by reducing the pressure of the products more quickly to allow fresh reactants to enter the flow more quickly.

Braun et al. compared engine performance when operated with hydrogen and methane. The hydrogen resulted in a much higher specific impulse, but the operational space of the two fuels remained similar. The operational space consists of all combinations of fuel and air mass flow rates, typically reported as the total mass flow rate and equivalence ratio, that produce detonations.

The Braun et al. cycle analysis also resulted in pressures and temperatures expected at the RDE outlet. The expected RDE temperatures and pressures are shown in Figure 5.

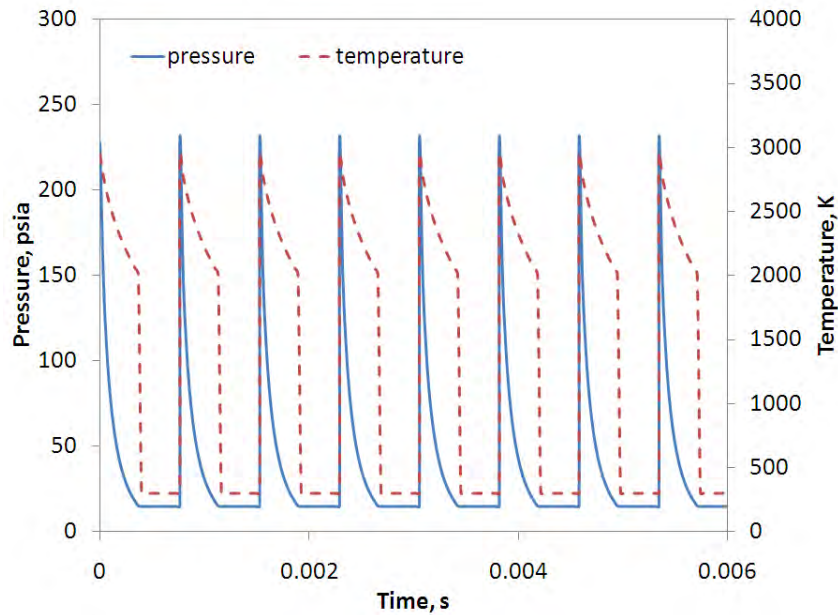


Figure 5. Outlet pressure and temperature for a 1.5 m circumference RDE with an H₂-air mixture at standard, stoichiometric conditions (12)

The cycle analysis predicts pressures up to 17 atm in the detonation channel and temperatures approaching 3,000 K. The combination of the high temperatures and pressures results in an extremely hostile environment for turbomachinery. Due to the harsh environment, the current research utilized a standoff between the turbine and the RDE outlet to allow the peak exhaust pressures and temperatures to be reduced by mixing before entering the turbine.

Russo (2) presented findings on the operability of the 3 in. RDE located at the DERF that was used as the basis for the current research performed. Russo accomplished testing to create operational spaces for enriched air (23% oxygen) and standard air (21% oxygen) for the 3 in. RDE. Suchocki (13) expanded the operational space of the 3 in. RDE using standard air, and took thrust measurements of the RDE at various operating conditions. The 3 in. RDE operational spaces served as a baseline for the RDE testing accomplished with the convergent

nozzles and the turbine because all testing for the current work was performed using the 3 in. RDE.

For the current research, convergent nozzle sections were tested before integrating the turbine to simulate the effects of back-pressurization on the RDE from the presence of a turbine in the exit flow. Shao et al. (14) accomplished a numerical study detailing the performance of a 53 mm diameter RDE with various nozzle sections placed in the RDE exhaust. The four nozzles studied are illustrated in Figure 6.

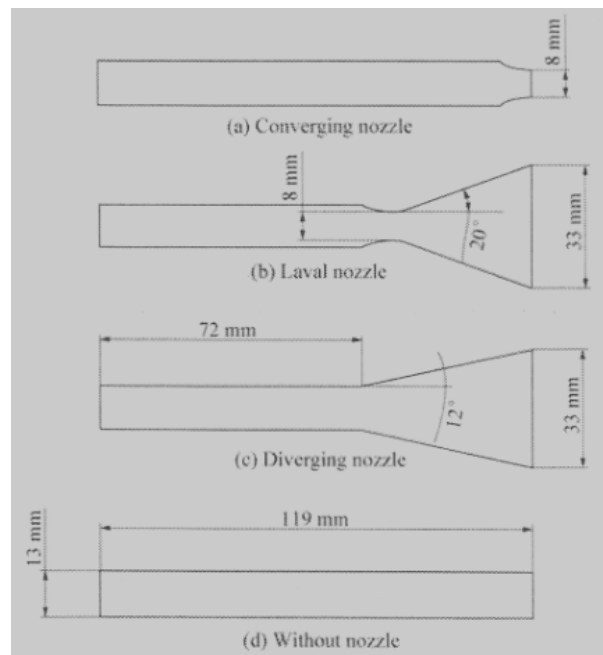


Figure 6. Cross-sections of converging-diverging nozzle configurations (14)

The flow remained subsonic in front of the nozzle throat, and then accelerated after the throat to Mach numbers greater than 2 as the detonation products flowed through the diverging section of the nozzle. All nozzles tested by Shao et al. increased the specific impulse and thrust of the RDE, with the diverging nozzle creating the most thrust and the Laval nozzle creating the highest gross specific impulse. The numerical study showed that the addition of nozzles resulted in

higher thrust and specific impulse, giving the expectation of increased performance for the RDE tested with the convergent nozzle sections for the current work.

Research performed by Bykovskii (15) showed that a wave speed of 1,100 m/s was the minimum velocity of detonations inside the RDE geometry tested for hydrogen-air mixtures. Research performed by Lee et al. (16) showed that a quasi-detonation regime occurred for hydrogen-air mixtures at a critical value on the order of 800 m/s in experimental testing using a pulsed detonation engine tube. Further research performed in this area by Karnesky et al. (17) considered wave speeds in the quasi-detonation regime, also considered the choked flame regime. The choked flame regime occurs when a combustible mixture in a detonation engine fails to undergo transition to detonation and the combustion wave consists of a turbulent flame that accelerates to a steady state supersonic velocity. A minimal loss of thrust between the detonation regime and the choked flame regime was recorded by Karnesky et al., with wave speeds 1,000 m/s and above producing a negligible difference in the impulse of the pulsed detonation engines. The conclusion that the choked flame regime produces similar thrust to a C-J detonation is promising for detonation engine applications, since the cycles that fail to reach the C-J detonation velocities will not necessarily cause a loss of performance. Russo (2) recorded many test runs with the 3 inch RDE that were considerably lower than the C-J speed of 1,950 m/s for hydrogen-air and nearer to the choked flame regime. The conclusions of Bykovskii (15), Lee (16), and Karnesky (17) aid research performed using the 3 in. RDE because the average wave speeds that remain above 1,100 m/s for a given run can be considered a successful detonation event although not reaching the C-J detonation velocity.

III. Test Setup and Methodology

1. Facility

All research was performed at the DERF in Building 71A, D-bay, at Wright Patterson Air Force Base, Ohio. The DERF and all its programs are under the AFRL Advanced Concepts Group. The DERF consists of a large engine test facility designed originally to test turbojet engines.

D-Bay consists of a main test cell with an isolated fuel room next to the test cell. A control room outside of the test cell serves as the primary station for testing, and personnel are protected from the test cell by a 2 ft wall of reinforced concrete. A compressor room is separated from both the test cell and the control room. The test cell is plumbed for compressed hydrogen and air from compressed gas tube trailers located outside of the building. The test cell holds several test stands, with the main test stand used for PDE design concepts. All RDE rigs operated at the DERF are located on the main floor next to the PDE test stand.

The control room remotely connects to all data acquisition devices and necessary components required to operate any of the various experiments performed in D-Bay. The control room consists of both a control panel and a control computer. The control panel provides power to operate switch valves that control the flow of fuel and oxidizers to the testing components, including the RDE and pre-detonator on the rig. The test cell has one primary point of entrance, and whenever this door is opened, the control panel automatically removes power from the critical components required for engine operation, such as the fuel valves, to ensure maximum safety while personnel are in the test cell. The control computer uses *LabView*® as the control software. The LabView software is capable of simultaneously collecting and recording data from 16 channels at rates of up to 5 MHz. The high speed data collected during testing may be

viewed quickly after testing, or may be saved for later analysis. Viewing data during testing allows for the accuracy and reasonableness of the data to be assessed to ensure all data acquisition systems are functioning properly. The program monitors fuel and oxidizer line pressures at key locations in the test cell and a load cell used to determine thrust from the 3 in. RDE.

2. Engine Setup

The RDE used for turbine testing, shown in Figure 7, was designed to operate on hydrogen and air.

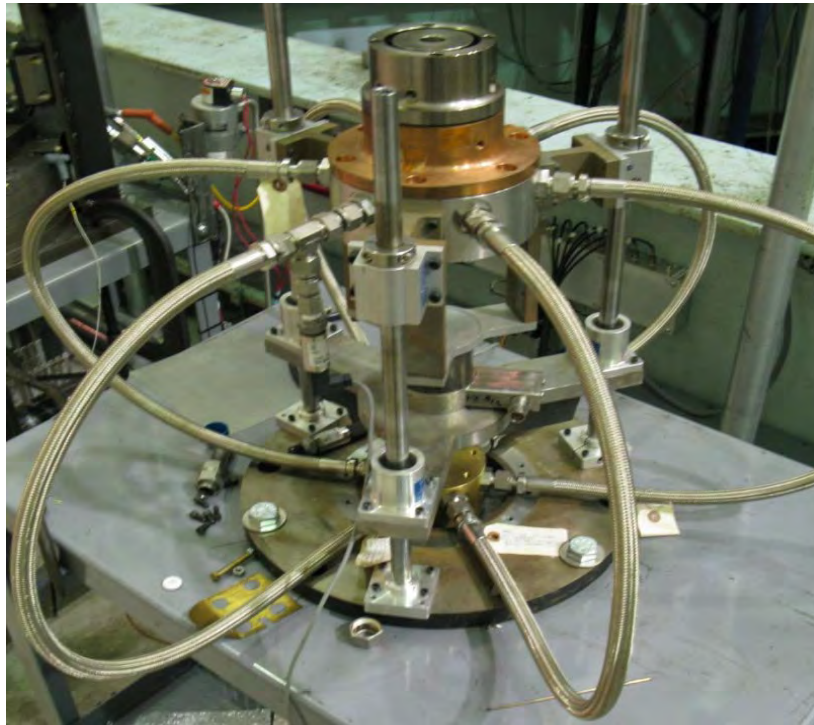


Figure 7. Three in. rotary detonation engine

The combustion chamber has a three in. outer diameter and length of four in. The lower section of the combustion chamber contains the detonation channel and is made of copper, while the upper section, which connects to the lower section via four socket cap screws, is made of

stainless steel. The combustion channel width is varied by changing the stainless steel center body diameter. The three possible channel widths are 2 mm, 6 mm, and 10 mm. All testing conducted for this research had a 6mm channel width, as this was determined to produce the best results from previous research by Russo (2). Hydrogen, which was used as the fuel for all testing, enters the RDE from beneath the engine, while air enters the RDE manifold from the side of the engine, and is then ducted to flow axially out of the RDE. The possible feed pressures available to the engine are a function of the sonic nozzle chosen for testing as shown in Table 1. All nozzle and turbine testing used the 0.252 in. air sonic nozzle and the 0.125 in. hydrogen sonic nozzle.

Table 1. Propellant feed pressures for 3 in. RDE rig

Standard air sonic nozzle diameter (in)	Feed pressure (psig), high	Feed pressure (psig), low
0.201	812	256
0.252 (used)	744	210
0.315	693	455
Enriched air sonic nozzle diameter (in)	Feed pressure (psig), high	Feed pressure (psig), low
0.201	565	287
0.252 (used)	729	322
Hydrogen sonic nozzle diameter (in)	Feed pressure (psig), high	Feed pressure (psig), low
0.063	585	90
0.125 (used)	561	90

The hydrogen and air enter the detonation channel where a detonation is developed tangentially to the flow via a spark plug initiated pre-detonator. Instrumentation on the RDE was set up on the lower copper section of the combustor, with three ports 0.75 in. from the bottom of the detonation channel and offset 120 degrees from each other, and two additional ports located 0.3 in. and 0.4 in from the detonation channel bottom. PCB Piezotronics® Piezoelectric dynamic pressure transducer, Kulite ® pressure transducer, and Honeywell® pressure transducer

data was collected using these ports. For all testing, the PCBs used were either model number S102A or 102M232, the Kulite pressure transducer model number was XCL-080, and the Honeywell pressure transducers used were either model TJE or TJF.

The delivery system for the propellant is illustrated in Figure 8. The mass flow rates of the propellants are controlled by dome-loaded pressure regulators which are fed by compressed nitrogen gas cylinders. The mass flow rates were adjusted by two methods during testing. Initially, the mass flow rates were adjusted by entering the test cell and setting the pressure regulator connected to the compressed cylinder to the desired pressure for testing. The control program was later updated so that the pressure regulators could be controlled from the control room. Air-driven valves quickly controlled the propellant flow during runs.

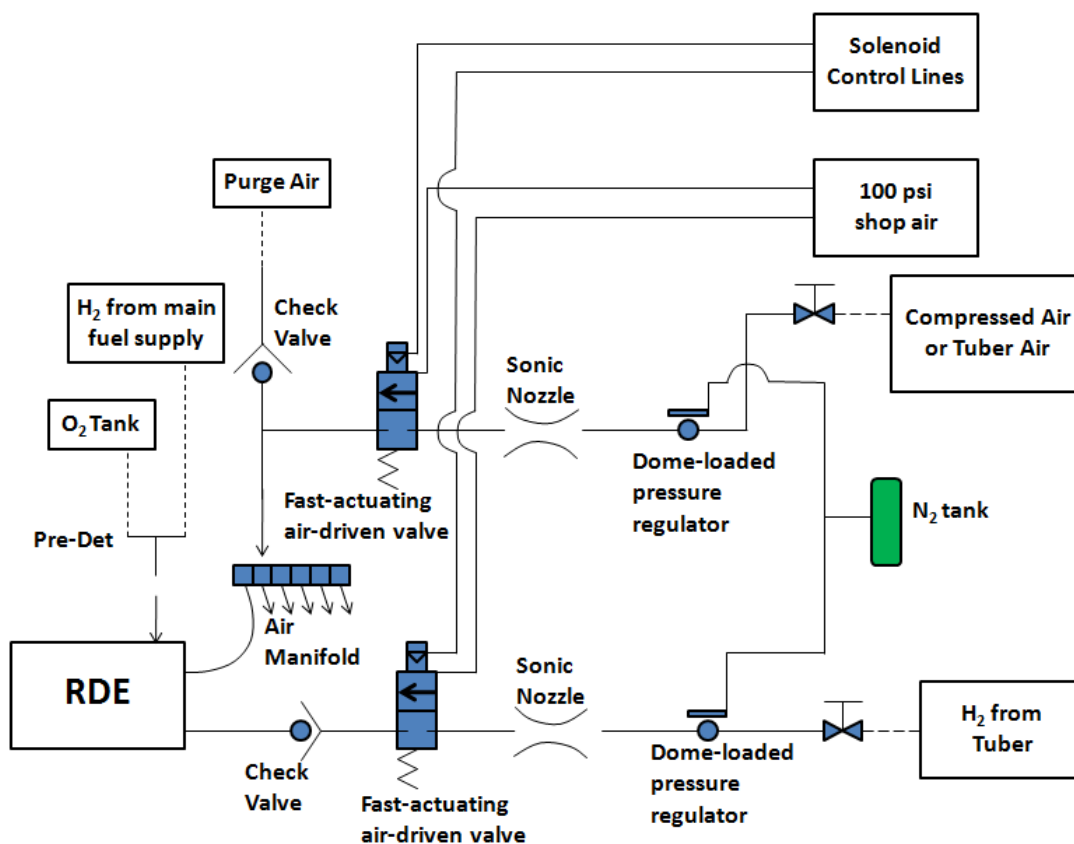


Figure 8. Propellant delivery system for 3 in. RDE rig

The operator defined the fuel establishing time, air establishing time, air operating time, and fuel operating time for each run. Establishing times are defined as the amount of time a propellant flows into the RDE before the pre-detonator is ignited, and operating times are the amount of time a propellant flows after the pre-detonator is ignited. The standard run for testing used an air establishing time of 2.5 sec, a fuel establishing time of 0.55 sec, an air operating time of 1 sec, and a fuel operating time of 0.75 sec. For a standard run, the pre-detonator was tested before every run by firing a minimum of three times to ensure that the pre-detonator was working properly. Next, the LabView program was activated which first ran air and fuel through the engine for 2.5 seconds and 0.55 seconds, respectively, before firing the pre-detonator. After the pre-detonator fired, the air and fuel continued to flow into the RDE for 1 sec and 0.75 sec, respectively, for an engine operation of 1 second from 2.5 seconds to 3.5 seconds into the run. The high speed data recorded only the measurements from the 1 second period of operation from 2.5 seconds to 3.5 seconds into the run, whereas the LabView control program measured and reported the air, hydrogen, and load cell data for 5 seconds, which included both before and after the engine operated. Pressures upstream and downstream of the air and fuel sonic nozzles typical for a run are shown in Figure 9. The upstream air and fuel pressures determined the mass flow rate of the run, and the upstream pressures needed to be at least 1.8 times the downstream pressure for the nozzle to be choked.

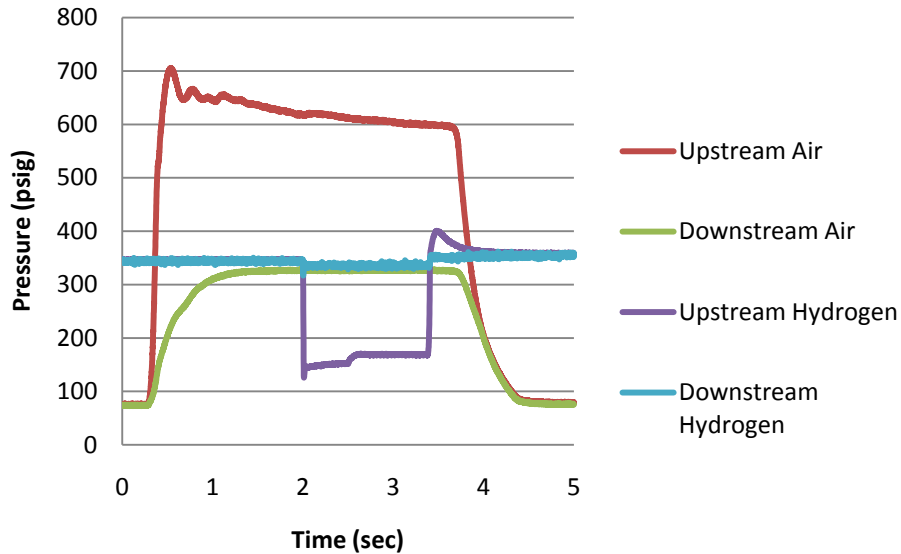


Figure 9. Standard run profile for pressures upstream and downstream of the air and hydrogen sonic nozzles

All nozzle testing reported occurred using the 1 second standard run profile discussed above. The data acquisition for nozzle testing used a scan rate of 1MHz for 1 second. Turbine testing was conducted with a lower fuel establishing time of 90 ms, and the fuel and air operating times were adjusted from a 0.2 second run for initial hot flow testing up to a 2 second run with a fuel operating time of 1.75 seconds and an air operating time of 2 seconds. The fuel operating time was always kept smaller than the air operating time so that unburnt hydrogen did not enter the test cell. The data acquisition for turbine testing used a scan rate of 250 kHz for 2 seconds or 500 kHz for 1 second. The scan rate had to be reduced for turbine testing because the data acquisition software could not support the addition of the pressure, mass air flow, and RPM sensors at a 1MHz scan rate for 1 second as was used for nozzle testing because the software did not have enough memory to store all the data points using a 1MHz scan rate

The air establishing time was set to 2.5 seconds so that the transients of the air upstream and downstream of the nozzle would be mostly eliminated by the time the fuel was added and

the pre-detonator was ignited. Testing was conducted using either air from the compressed gas tube trailer, which had a 23% molar concentration of oxygen, or standard air (21% oxygen).

3. Experimental Setups

A. 1.5 in and 1.17 in Nozzle Setup

The overall objective of the research was to operate a turbine using the RDE. Testing was accomplished using convergent nozzles placed at the RDE exit before turbine testing to simulate the presence of a turbine at the RDE exit. The convergent nozzle diameter was calculated from JetCat P-200 turbine operating conditions at the turbine stator vanes and applying a variation of the mass flow rate equation from Mattingly (18) shown as Eq. 1.

$$D_{reduced} = \sqrt{\frac{4\dot{m}RT}{\pi PV}} \quad (1)$$

As reported by JetCat, the maximum mass flow was 60 lbm/min, and the maximum pressure was 4 atmospheres. The temperature was calculated by performing a cycle analysis on the JetCat P-200, and the velocity was assumed to be sonic due to choking of the turbine stator vanes. A nozzle diameter of 1.17 in resulted in an equivalent area to the turbine stator vanes. Initially, the exit diameter was only reduced to 1.5 in. and tested on the RDE in an attempt to understand RDE operability as the exit diameter was reduced. Next, the exit diameter was reduced to 1.17 in to test the RDE at the reduced area equivalent to that of the choked turbine stator vanes. The RDE exit area, which was initially 2.05 in², was reduced by the nozzles to the values shown in Table 2.

Table 2. Area ratios for convergent nozzles placed on RDE

	D (in)	Area (in ²)	A _{nozzle} /A _{RDE}
Nozzle 1	1.5	1.767	0.862
Nozzle 2	1.17	1.075	0.488

The experimental setup for the RDE with the 1.5 in nozzle can be seen in Figure 10.



Figure 10. Experimental setup for 1.5 in. convergent nozzle on RDE

Three pressure measurements were taken in the combustion chamber of the RDE. The dynamic pressure was measured using a PCB dynamic pressure transducer located 0.3 in from the detonation channel bottom, and the static pressure was measured using a Kulite pressure transducer located 0.4 in. from the detonation channel bottom. The PCB was used to determine the pressure spikes from a passing detonation wave. The PCBs have a response time of less than $1\text{ }\mu\text{s}$, and using the C-J velocity of 1,950 m/s for hydrogen-air mixtures, a detonation wave takes $123\text{ }\mu\text{s}$ to travel around the detonation chamber, which allows adequate time for the PCB

between detonation wave passes. The Kulite pressure transducer was used for the same purposes as the PCB, as well as to measure the static pressure in the chamber. The Kulite rise time is $4\text{ }\mu\text{s}$, which gave it a slower response than the PCB, but still a fast enough response to adequately capture the passing detonation waves.

After determining the initial characteristics of a detonation wave with the 1.5 in. diameter nozzle, the 1.17 in. nozzle was tested on the RDE as shown in Figure 11.



Figure 11. Experimental setup for 1.17 in. convergent nozzle on RDE

The measurement techniques of the RDE used for the 1.17 in. convergent nozzle were the same as for that used on the 1.5 in. nozzle, except no Kulite pressure transducer was used and a 200 psi

Honeywell pressure transducer was placed 0.7 in. from the detonation channel bottom. The 200 psi pressure transducer was used to get an average pressure reading from the combustion chamber during a run. Three PCBs located 0.7 in. from the detonation channel bottom tracked the detonation wave speed. For the 1.17 in. nozzle testing, ports were added at three locations along the nozzle, as shown in Figure 11, and static pressure measurements were taken at the nozzle base and at the nozzle throat. These pressure ports were placed on the nozzle after the discovery of shock diamonds in the RDE exhaust for the 1.5 in. nozzle dictated a need to determine the pressures in the nozzle during testing to determine the flow characteristics from the nozzle base to the nozzle throat. The static pressure measurements were taken using one 100 psi and one 200 psi Honeywell pressure transducers with a standoff distance of 3.5 ft.

B. Turbine Build Up and Experimental Setup

After nozzle testing was completed, the second experimental setup was used to run a turbine using the RDE exhaust gases. The turbine used for testing was the JetCat P-200. A new circular plenum was designed and fabricated to duct the flow from the RDE to the axial turbine (see Figure 12). The compressor and turbine flow streams were separated so that the compressor took in ambient air while the turbine was fed products from the RDE. The compressor air flowed through the centrifugal compressor and out at a 90 degree angle via the compressor housing, while the RDE exhaust gases flow path went through the circular plenum and turned 90 degrees to enter the turbine before exiting through the attached nozzle.

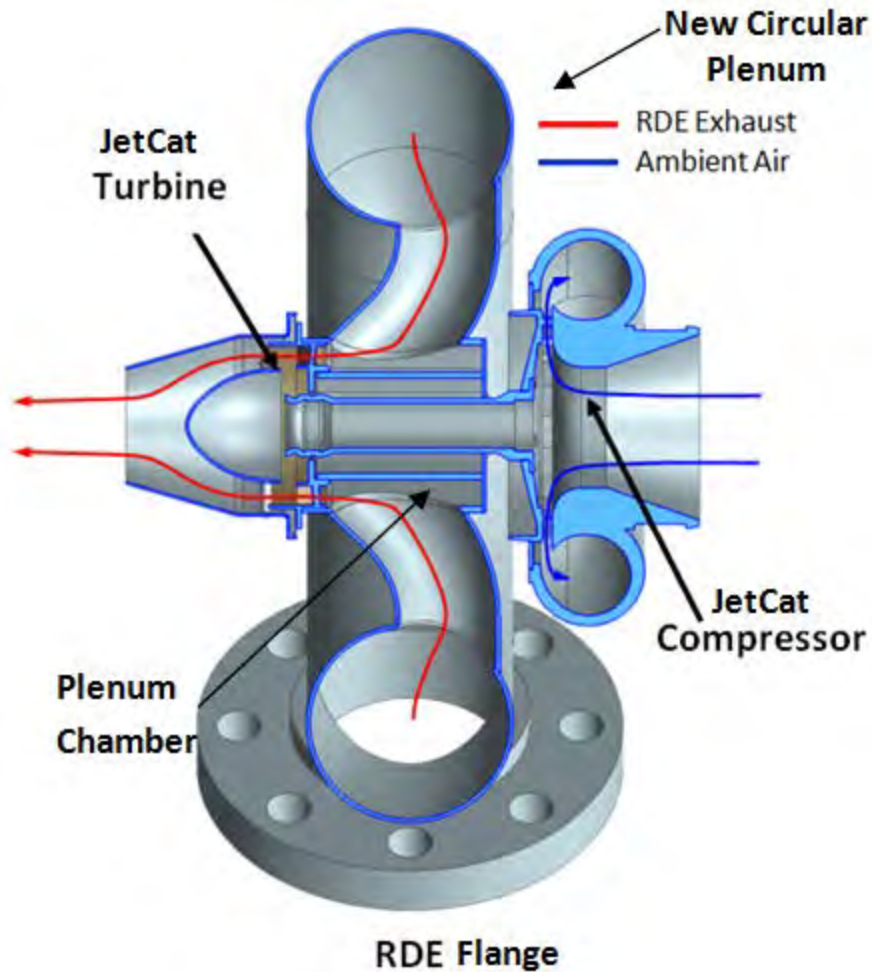


Figure 12. New circular plenum adapter for JetCat compressor and turbine

The JetCat nozzle was attached to the turbine exit so that the turbine would operate closely to the standard JetCat P-200 configuration. Because the RDE exhaust gases are at high temperatures and pressures (peaks up to 3,000 K and 200 psia as determined by Braun et al. (12)), the stand-off distance created by the plenum between the turbine and the RDE allows the unsteady flows at varying temperatures and pressures to mix, reducing the spikes in both pressure and temperature and allowing an increased level of confidence in turbine survivability. The circular plenum adapter also maintains the original JetCat design closely, so there is a higher confidence that the results can be compared with data obtained from running the JetCat using its

own combustion system. The primary disadvantage to this experimental setup is that turning the flow 90 degrees to enter the turbine could result in a substantial pressure drop across the plenum.

The JetCat P-200, shown in Figure 13, was altered to be placed on the RDE for testing.

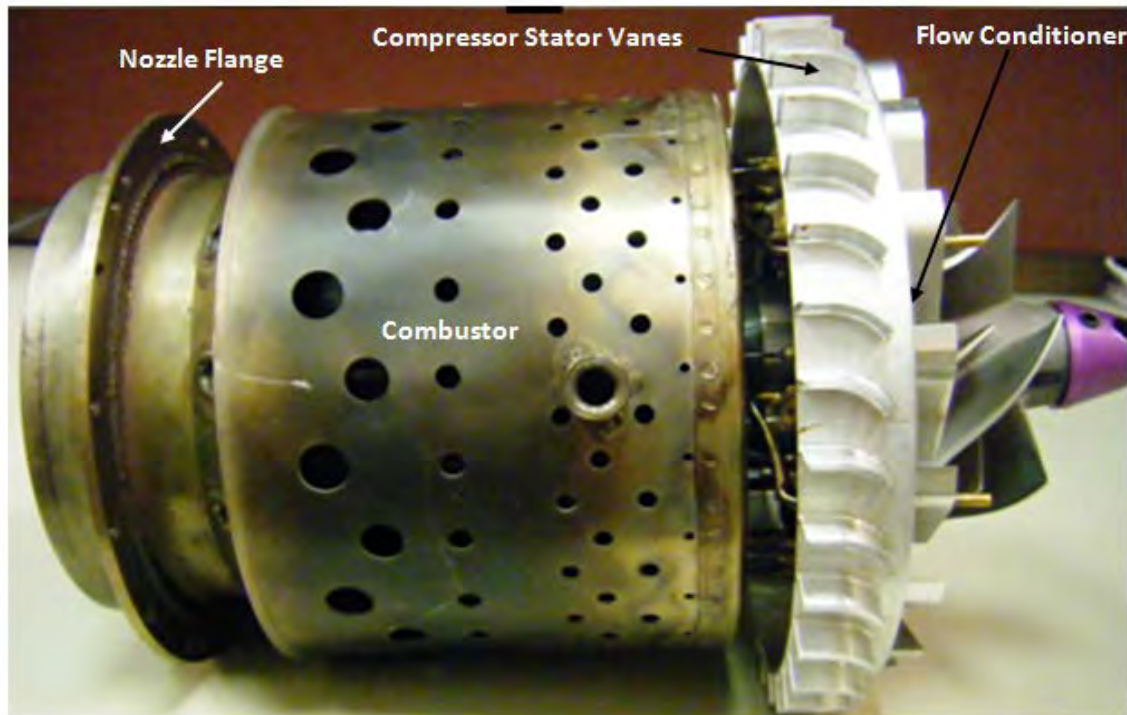


Figure 13. JetCat P-200 with the inlet, outer casing and nozzle removed

In order to keep the JetCat close to its original configuration, the JetCat combustor was removed, but the turbomachinery was kept intact. The nozzle flange was detached so that the JetCat would be able to slide into the circular plenum from the turbine side. The compressor stator vanes were milled flush with the flow conditioner so a compressor housing backing could be placed around and welded to the flow conditioner. The adjustments to the JetCat turbine are shown in Figure 14.

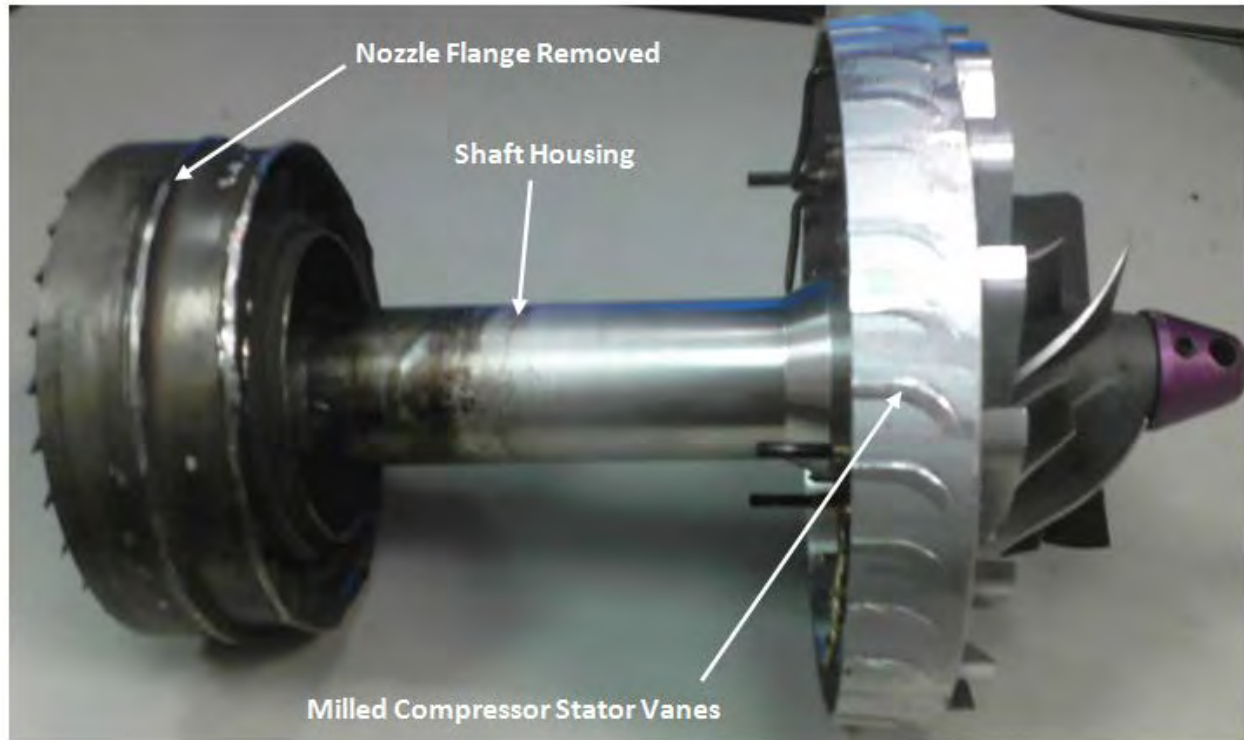


Figure 14. JetCat P-200 with the compressor stator vanes milled flush with the flow conditioner and the combustor and nozzle flange removed

After removing the combustor, nozzle flange, and compressor stator vanes, a newly fabricated stainless steel inner jacket was attached to the turbine casing to serve as a barrier between the hot exhaust gases of the RDE and the aluminum shaft housing, shown in Figure 14. A plenum cap was welded to the inner jacket to enclose the plenum chamber. An aluminum compressor backing was placed around and welded to the flow conditioner to enable a centrifugal compressor housing from a Garrett® turbocharger to be placed on the JetCat compressor. The JetCat centrifugal compressor was designed by JetCat and therefore had no stock centrifugal compressor housing. The dimensions of the JetCat inlet were measured, and a Garrett compressor housing, seen in Figure 15, was bored and machined to match the dimensions of the JetCat inlet to ensure that the compressor operated under the same conditions as with the inlet attached. Originally, both the main fuel line and the lubricant line, which was diverted from

the main fuel line, were routed through holes in the flow conditioner to provide the combustor with fuel and the bearings with lubricant. The lubricant flowed into the back of the compressor, where it was further compressed and coursed through the shaft housing to lubricate the shaft bearings. Because the centrifugal compressor housing blocked access to the holes used in the flow conditioner for routing the fuel and lubricant, the tubing for the bearing lubricants was rerouted through the cavity between the plenum chamber and the backside of the compressor to allow for bearing lubrication during testing. The main fuel line was removed because the RDE was being used as the combustor and therefore no combustor fuel was needed. The bearing lubricant line, the inner jacket, the plenum cap, and the compressor backing added to the JetCat are shown in Figure 15.

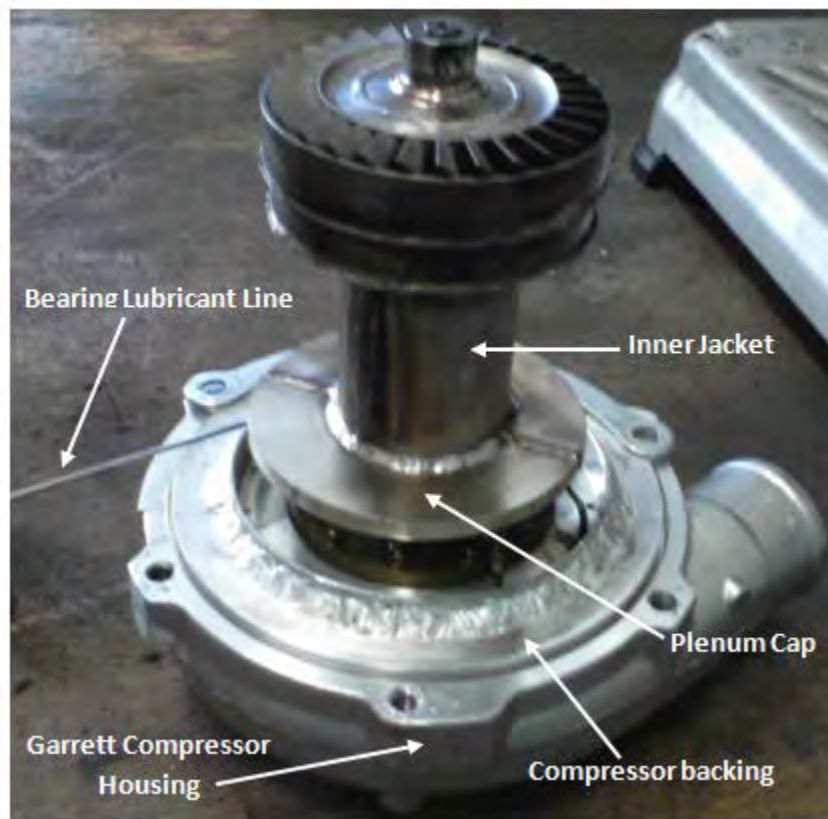


Figure 15. JetCat with the inner jacket, compressor backing, plenum cap, and bearing lubricant line

To integrate the JetCat with the plenum, the JetCat was placed through the outer jacket of the circular plenum as shown in Figure 16. The circular plenum was constructed of stainless steel, 4 in. pipe and welded together to ensure the plenum was sealed. From the viewpoint of Figure 16, the JetCat was placed behind the plenum and then slid out of the page through the outer jacket of the plenum. The outer jacket, inner jacket, and plenum cap served as the boundaries for the plenum chamber (labeled in Figure 12), which lies between the JetCat compressor and turbine in place of the JetCat combustor.

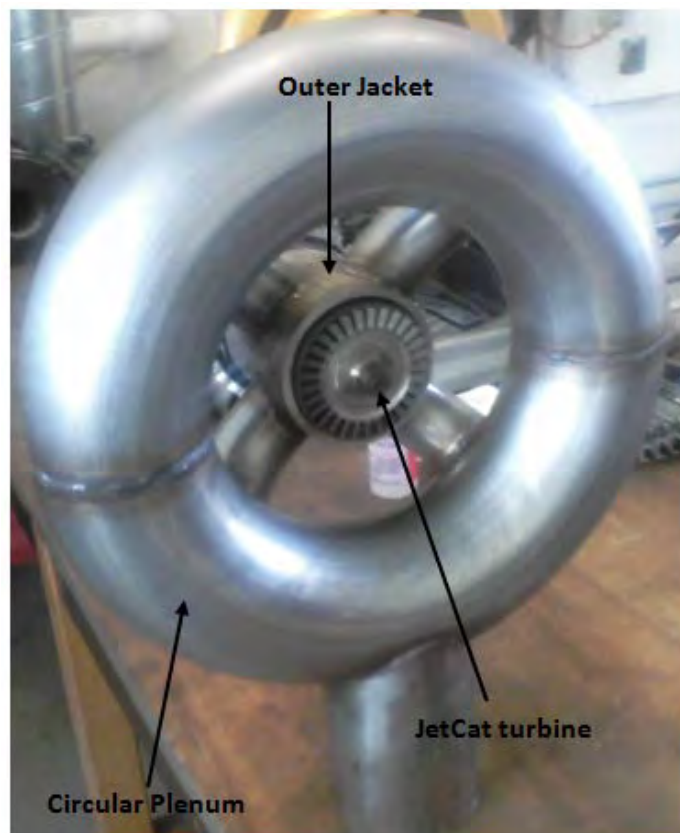


Figure 16. JetCat position with respect to the circular plenum

To seal the plenum chamber, the JetCat nozzle was reinstalled over the turbine housing and welded to the outer jacket. A stainless steel disc was welded to the plenum and the

compressor housing was bolted to the disc for stability and structural integrity of the JetCat, seen in Figure 17.

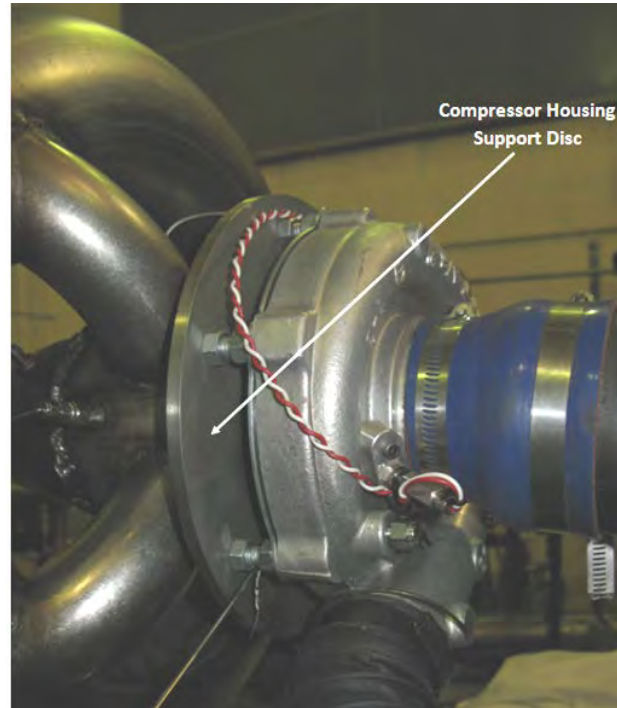


Figure 17. Plenum disc used to stabilize and support the centrifugal compressor housing

The experimental setup for the turbine testing can be seen in Figure 18 and Figure 19. The circular plenum in Figure 18 has the same orientation and flow path as is shown in Figure 12. Two flanges were created to connect the plenum to the RDE, with one flange welded to the plenum and the other flange fastened to the RDE with 4 socket cap screws. The flanges were connected with 6 ½ in hex screws, and a high temperature gasket was placed between the flanges for sealing. A unistrut was placed over the rig and the top of the plenum was attached to the unistrut for additional support.

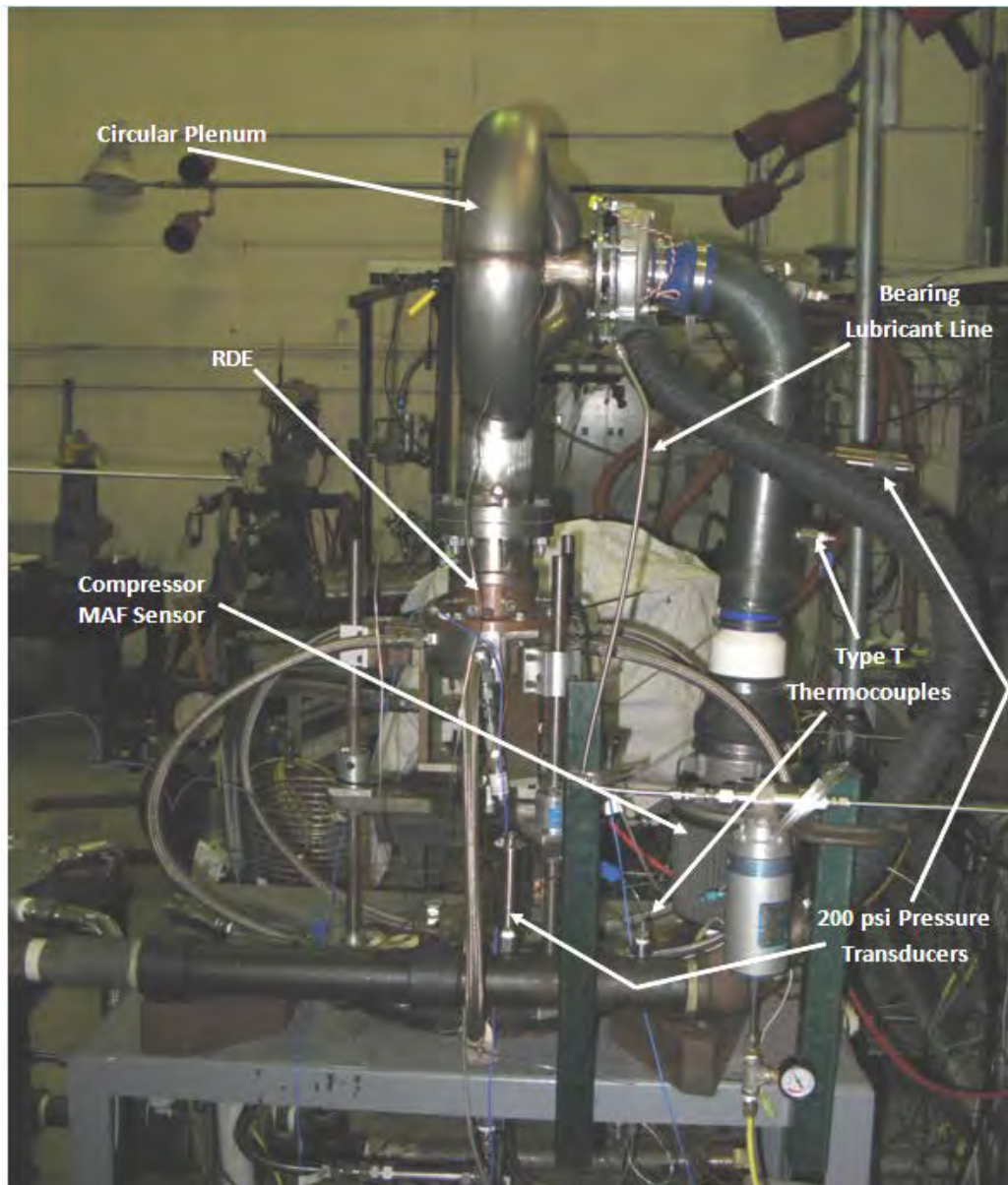


Figure 18. Experimental setup for JetCat turbine testing using the 3 in. RDE

The experiment was run at various RDE mass flow rates and equivalence ratios to determine turbine operability at differing RDE operating conditions. The primary measurements taken from the RDE were PCB measurements using the three 120 degree offset ports located 0.7 in. from the bottom of the detonation channel. These measurements were used to determine the

average wave speed in the detonation channel to determine whether a run had successful detonations.

The compressor mass flow rate was determined using a Pro-M® 92 mass air flow (MAF) sensor placed in front of the compressor inlet. The compressor MAF sensor was connected to the compressor inlet by 3 in. tubing that was straight for 12 in. before connecting to a 90 degree elbow that joined the tubing with the compressor inlet. The compressor temperature measurements were taken with a grounded, 1/8 in. diameter Omega® T type thermocouple located 4.2 in. from the MAF sensor, and the compressor pressure measurements were taken with a Honeywell 200 psi pressure transducer located 8.125 in. from the MAF sensor. The compressor outlet flowed through 2 ft of flexible tubing into a section of 2 in. steel tubing. The compressor outlet temperature measurement was taken with a T type thermocouple located 2.45 in. from the flexible tubing connection, and the compressor outlet pressure was measured using a Honeywell 200 psi pressure transducer located 8.25 in. from the flexible tubing connection. A compressor exit ball valve was placed at the end of the 2 in. tubing to force the compressor to run at specific operating conditions. The ball valve was located at the exit of the 2 in. tubing, which was located 32 in. from the flexible tubing connection.

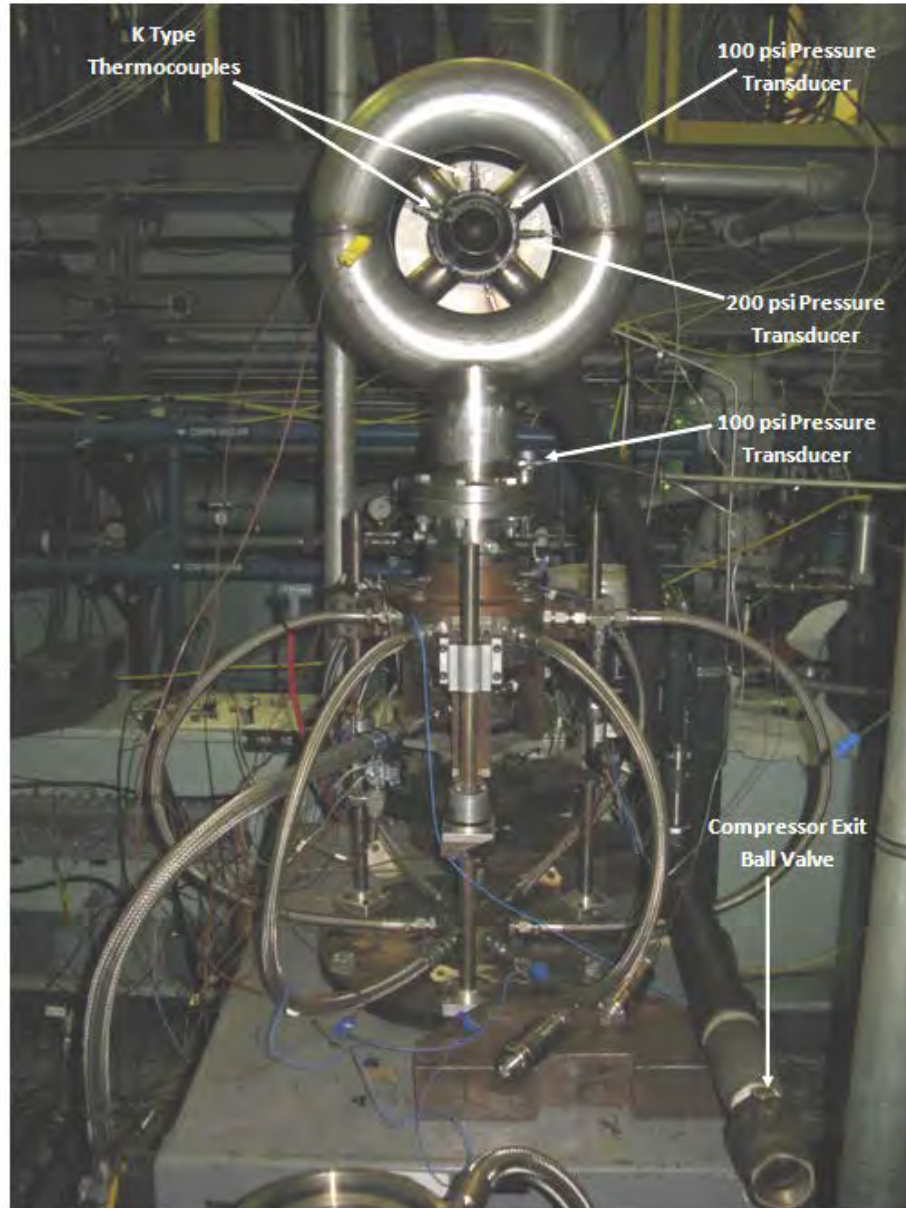


Figure 19. Turbine measurement locations for the JetCat turbine experiment

The turbine pressure and temperature measurements were taken in the plenum chamber before the turbine stator vanes and in the nozzle section after the exhaust passes through the turbine rotor blades. The turbine temperature measurements were taken with grounded, 1/8 in. diameter K type thermocouples. The plenum chamber pressure was taken with a 200 psi pressure transducer, and the pressure after the turbine rotor was taken with a 100 psi pressure

transducer. The locations of the turbine inlet and outlet measurements are illustrated in Figure 20 and Figure 21, respectively.

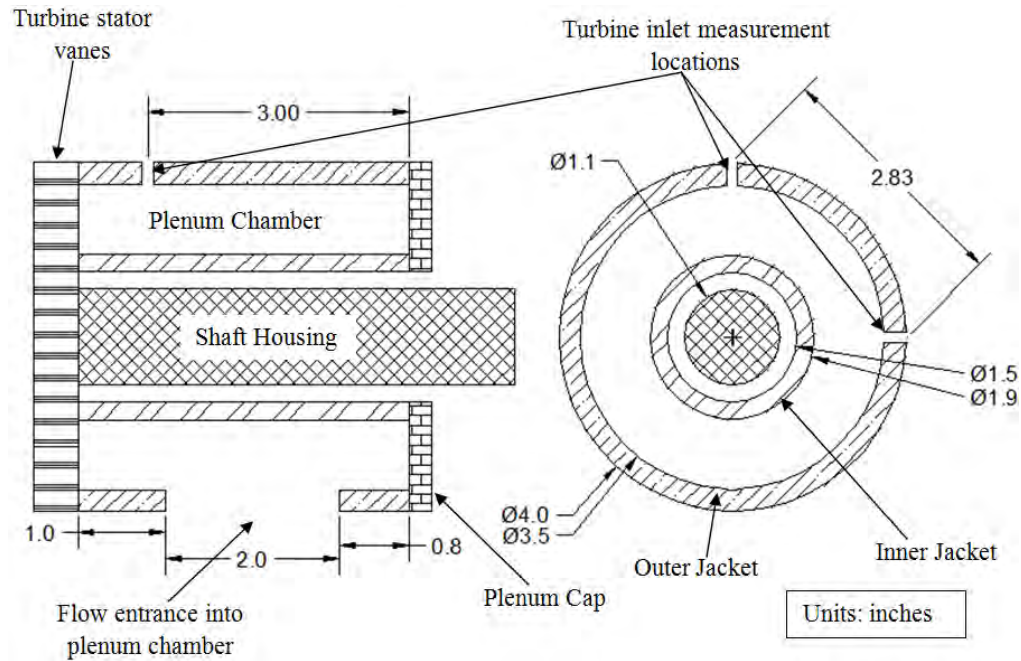


Figure 20. Schematic of plenum chamber showing dimensions and locations of turbine inlet measurements for turbine-RDE testing

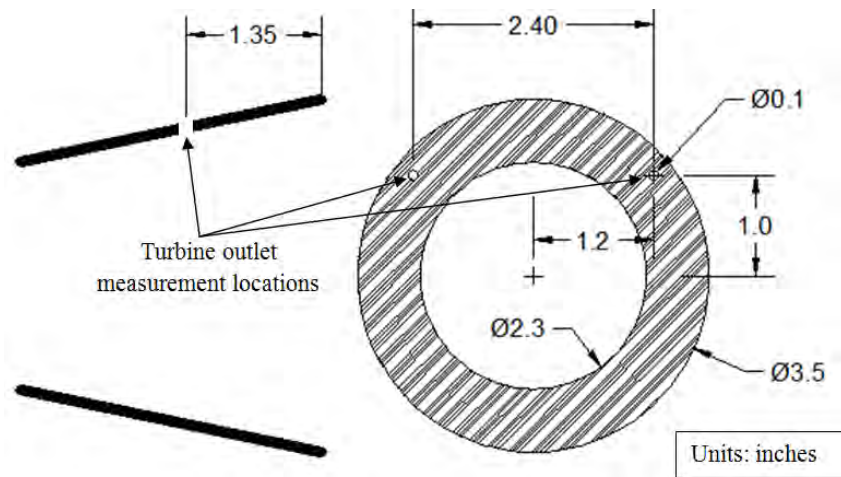


Figure 21. Schematic of JetCat nozzle with dimensions and locations of turbine outlet measurements for turbine-RDE testing

The turbine mass flow rate was equal to the RDE mass flow rate, which was set by the operator. Measurements were also taken from the base of the plenum during cold flow testing using a 100 psi pressure transducer located 0.8 in. above the plenum flange to determine the pressure variations from the plenum base to the plenum chamber.

The rotor speed was measured using a Garrett speed sensor that was positioned in the compressor housing, as shown in Figure 22, to measure blade arrival times. The sensor emits a magnetic field that is interrupted by passing blades. Rotor speed is determined by the difference in blade arrival times.

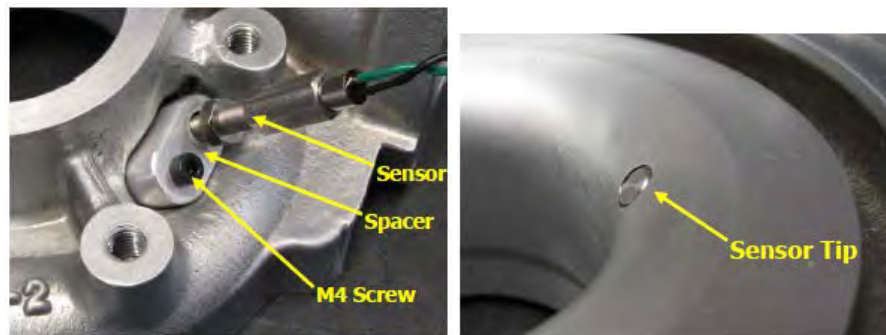


Figure 22. Garrett speed sensor (used with permission by Garrett)

A lubricant system was developed to feed the bearings in the JetCat turbine during operation. The JetCat turbines typically use a mixture of 95% kerosene, 5% synthetic turbine oil solution for lubrication, but for this testing a 95% JP-8, 5% synthetic turbine oil mixture was utilized due to previous testing at AFRL that had successfully operate JetCat turbines using JP-8 instead of kerosene. The lubricant flows into the JetCat bearings behind the compressor, and then flows through the shaft to the bearings located near the turbine. The lubricant then exits the shaft and is burned in the combustor. To lubricate the JetCat bearings, a pressurized fuel container was set to a pressure of 30 psig, which was the pressure of the lubricant at maximum

RPM for normal JetCat operation. The lubricant then passed through a Max Machinery® piston flow meter designed to read flow rates of 1 cc/min to 1800 cc/min. The maximum lubricant flow rate for the JetCat was 30 cc/min for a RPM of 112,000. A series of air-actuated ball valves were connected to the RDE control program so the control program could control the flow of the lubricant to the turbine. The control program, once activated, switched the lubricant ball valves to allow flow to the bearings for 1 second, and then checked the lubricant mass flow meter three times to ensure that lubricants were flowing at a minimum flow rate of 30 cc/min. The typical flow rate for testing was 35 cc/min. If all three measurements measured a flow rate of 30 cc/min or greater, the RDE sequence continued with the original sequence used for RDE and nozzle testing. Three manual ball valves were installed and a bypass fuel line was created so that fuel flow path could be changed to bypass the mass flow sensor if necessary. A check valve was also installed so that the lubricant could not flow backwards into the mass flow sensor. One air-actuated ball valve was located in the fuel room, and one was located near the turbine rig so that if the air-actuated ball valve near the rig was damaged or failed, the air-actuated ball valve in the fuel room would still cut flow of the lubricant to the turbine. The lubricant system is illustrated in Figure 23.

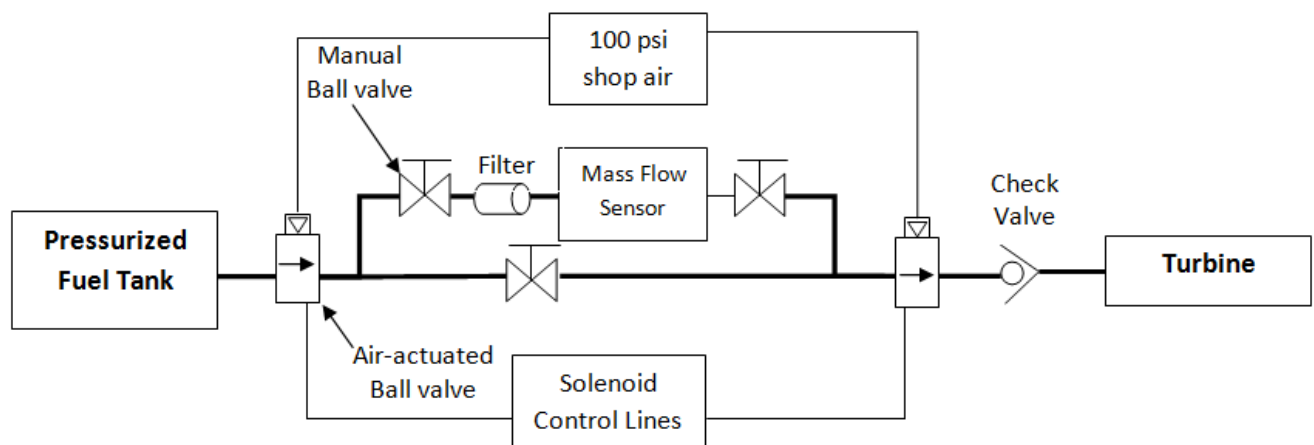


Figure 23. Lubricant delivery system to JetCat bearings for turbine testing

4. Data Collection

The average wave speed of a run determined whether or not the run had successful detonations. RDE runs with wave speeds greater than 1,100 m/s were considered successful runs as speeds greater than this could be considered a successful detonation run as reported by Bykovskii (15), Lee (16), and Karnesky (17).

5. Data Reduction

A. PCB Wave Speed Sensitivity

PCB data was collected during all testing of the RDE. Wave speeds were then determined using a time of flight code in MATLAB®. During RDE testing with the 1.5 in. nozzle attached, a Kulite pressure sensor was also used to determine both the wave speed and pressures in the detonation channel. The Kulite data was also analyzed via the time of flight code using MATLAB. The time of flight code determined the wave speeds in the detonation channel by measuring the time between pressure peaks and then dividing the circumference of the RDE channel by the time between peaks. The threshold value, the time hold, and the points above the threshold (PAT) were the three primary variables used in determining what was considered a peak pressure for use in calculating the wave speed of the run. The threshold value was determined by taking the average value of the data for each run and then choosing a threshold based on the number of standard deviations above the average. The time hold was determined by choosing a time period after the last known detonation in which no detonations could be recorded. The PAT determined how many consecutive data points were needed to be collected above the threshold to determine whether a detonation occurred or not. A PCB sensitivity analysis was done using these three primary variables and is shown in Figure 24.

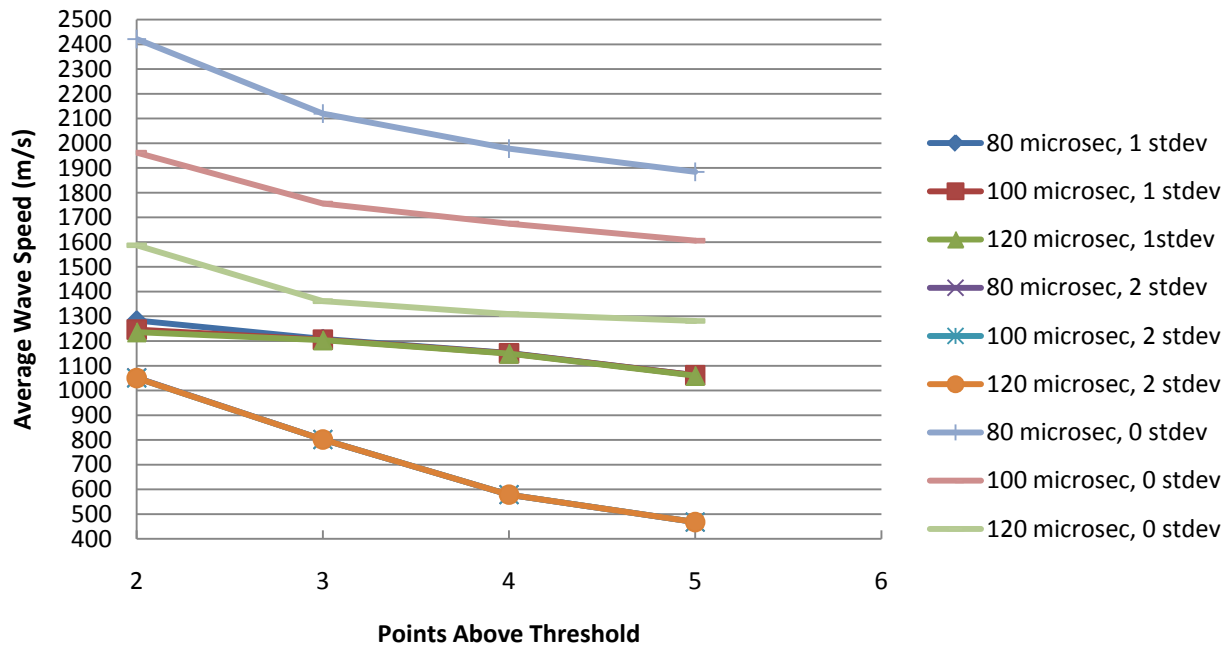


Figure 24. PCB average wave speed sensitivity analysis for variations in threshold, time hold, and points above the threshold

A threshold of 0 standard deviations resulted in the data being primarily reliant on the time hold for determining when a detonation occurred. A standard deviation of 2 was primarily affected by the number of PATs chosen, and so the values that were determined to produce the best wave speed data was a threshold of 1 standard deviation above the average, a hold time of 100 μ s.

B. Kulite Wave Speed Sensitivity

For the Kulite data, the time of flight program was varied over a wide range of possibilities for all three variables, with the results shown in Figure 25.

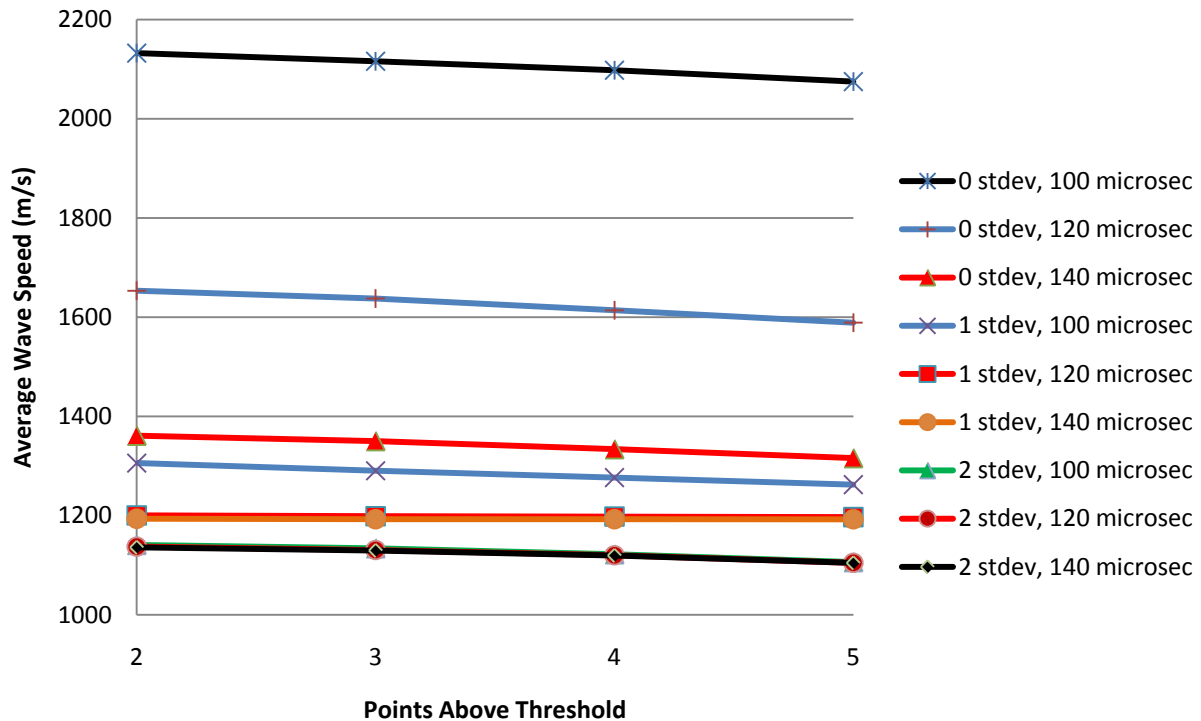


Figure 25. Kulite average wave speed sensitivity analysis for variations in the threshold, time holds, and points above the threshold

The least variation occurred for a threshold value 1 standard deviation above the average and a 120 or 140 μ s hold time, with the number of PATs mattering little in these cases. A PAT value of 4 was chosen because for a threshold 1 standard deviation above the mean, the percent probability of an erroneously high velocity is calculated as 0.17^x as shown by Russo (2), where x is the number of consecutive points above the threshold. Four consecutive points yields a 0.08% probability of an erroneously high velocity while yielding an average velocity that varies less than 0.1% from the average velocities found using 3 and 5 consecutive points above the threshold. Based on the results, the time of flight program used a threshold of 1 standard deviation above the average, a time hold of 120 μ s, and a PAT value of 4 to determine the detonation velocities for a run. These variables were determined based on what values gave the

most consistent results for the Kulite as well as which values closely matched the PCB results so as to have as little variation between the Kulite and PCB data reduction methods.

The PCB wave speed data produced two primary bands using the initially chosen values for the standard deviation, time hold, and PAT, with one band over 1,000 m/s and the other band in the 600 m/s band as shown in Figure 26.

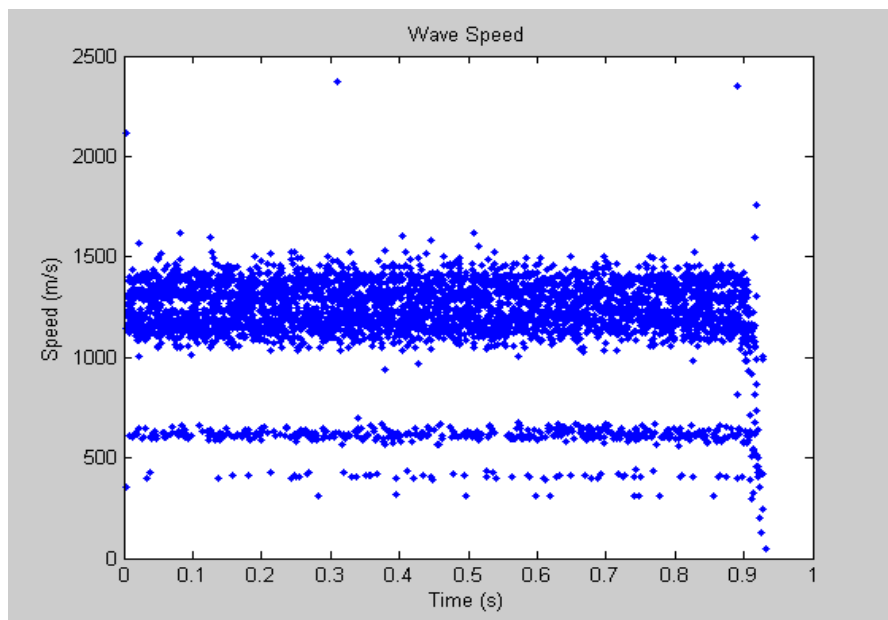


Figure 26. Wave speeds for PCB from time of flight code for 100 μ s hold time, 1 standard deviation threshold, and 3 points above threshold

This is contrasted with the Kulite wave speed data, shown in Figure 27, which showed a much more consistent pattern than the PCB data, with only one primary band that occurred with the majority of the velocities being greater than 1,000 m/s.

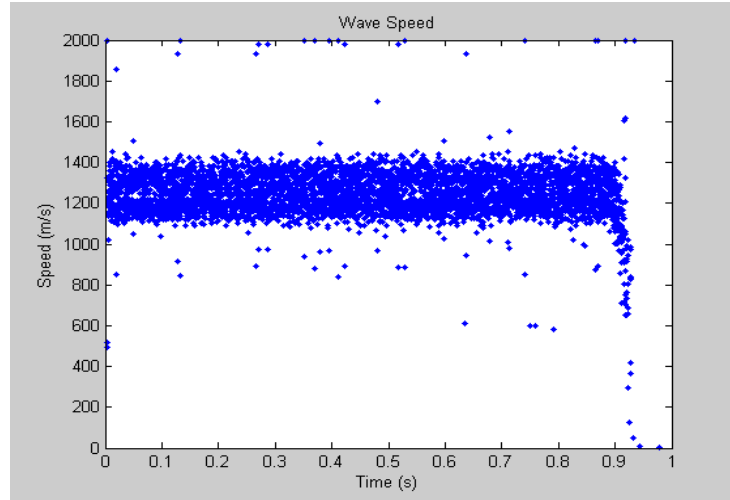


Figure 27. Wave Speeds for Kulite from time of flight code for a 1 standard deviation threshold, a 120 μ s hold time, and 3 points above threshold

C. Linear Sensitivity

The differences in data caused the Kulite average velocities to be higher than the PCB data, and the percent difference in the results can be seen in Appendix A. One of the reasons for the difference in the data between the Kulite and PCB was a result of the nature of the PCB data, as shown in Figure 28.

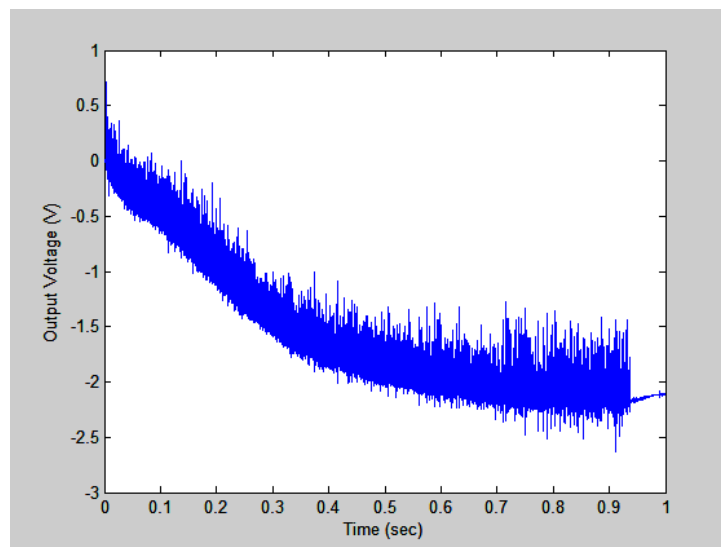


Figure 28. PCB pressure sensor data for a run with successful detonations

Because the detonation channel becomes extremely hot during the run, the PCB experiences thermal drift. Thermal drift manifests itself as the output voltage gradually decreasing throughout the run. The post-processing of this data uses a mean value to determine the peak pressures, but this cannot be accomplished without first normalizing the PCB data so that the data has a similar mean value. The time of flight code used in MATLAB splits up the data using break point locations and determines the linear trend for each section; an example of this is illustrated in Figure 29.

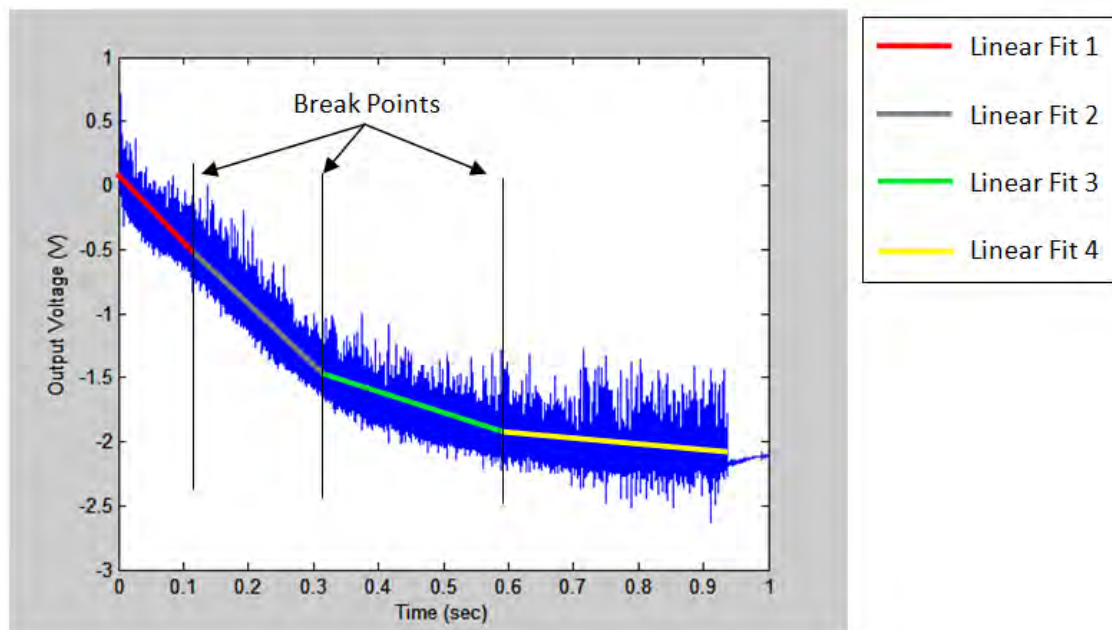


Figure 29. Four line linear fit of PCB data used to normalize PCB data

The code then removes the linear trend to normalize the data. However, this leads to errors as the PCB data is not completely linear in nature, so some data points become normalized either too high above or too low below the mean value, which may cause the time of flight code to find peak pressures where they do not exist or pass by peak pressures that should be accounted for in

determining wave speed. Thus, a sensitivity analysis was accomplished by changing the number of linear equations determined in the code, and the results are shown in Figure 30.

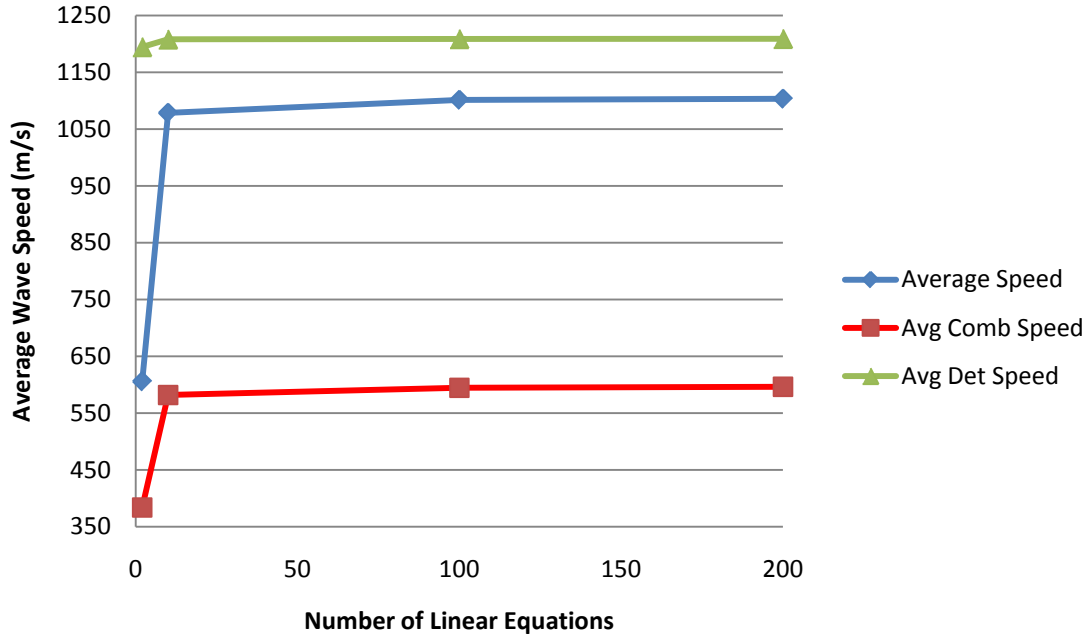


Figure 30. Sensitivity of PCB wave speed calculations to the number of linear equations created to normalize the data

It was determined that 10 lines gave the best solution, because the computational rigor was much lower, and there was only a 2.25% difference in the value for average wave speed between the 10 and 200 line scenarios. As the number of lines increased, the number of velocities calculated in the 600m/s band decreased, as shown in the velocity histograms in Appendix A.

The Kulite data did not experience the thermal drift that the PCB data did, so the Kulite data had no linear trend in the data as seen in Figure 31.

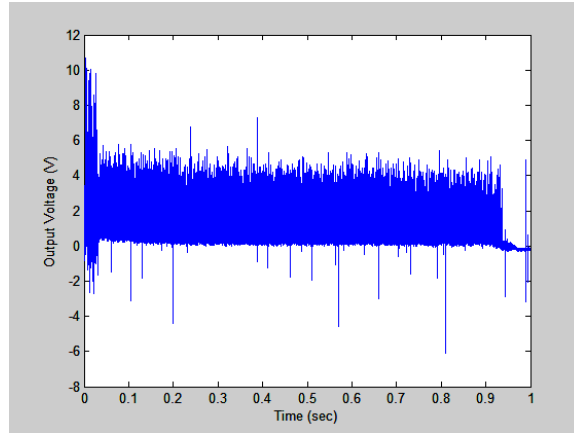


Figure 31. Kulite pressure transducer data for a run with successful detonations

Because of this, the sensitivity of the Kulite wave speed to the number of linear equations made for the data was negligible as seen in Figure 32.

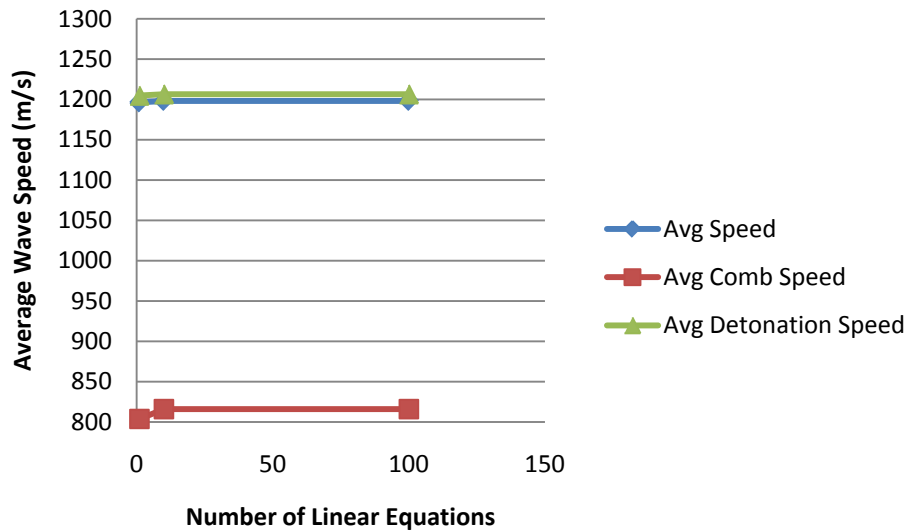


Figure 32. Sensitivity of Kulite wave speed calculations to the number of linear equations created to normalize the data

The largest error of all the data was the average combustion speed between 1 and 100 lines, where the error was 1.49% between the two values. Due to the small error and the reduction of computational rigor, only 1 linear equation was chosen to normalize the Kulite data.

D. PCB Aliasing

The other reason for the discrepancy in velocities between the PCB and Kulite data had to deal with the nature of the PCB data and the time of flight code used to determine the velocities. In the initial sensitivity studies of the PCB and Kulite data, the Kulite data showed much less variation as the number of points above the threshold was increased. A finer study was conducted on the affect of changing the number of points above the threshold for the PCB and Kulite data, with the results of the studies shown in Figure 33.

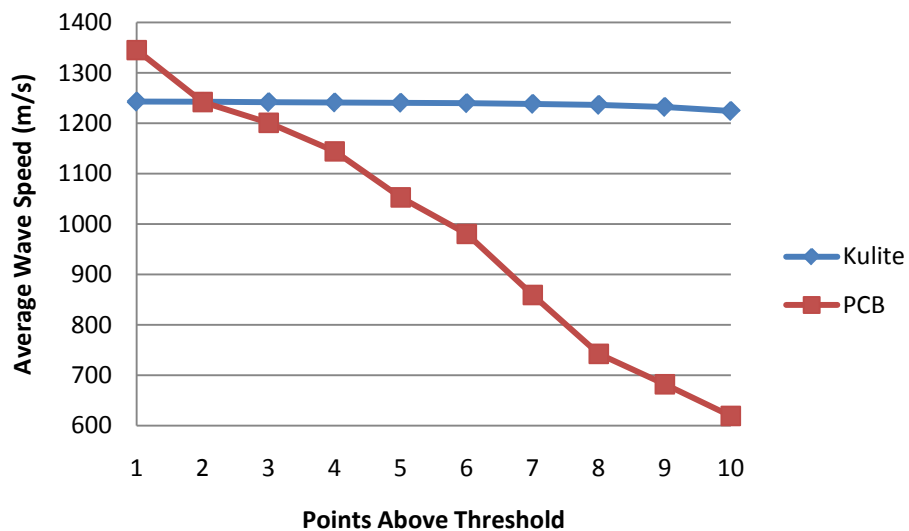


Figure 33. Points above threshold sensitivity analysis for wave speed velocities of Kulite and PCB data using a hold time of 120 μ s and a hold time of 1 standard deviation

The overall variation of the PCB average wave speed from 1 to 10 points above the threshold was 53.96%, whereas the Kulite data only varied 1.52% from 1 to 10 points above the threshold. The reason for the large variations in the PCB data and the lack of variation in the Kulite derives from the way the time of flight code is written and the nature of the data. A close up of the PCB data can be seen in Figure 34.

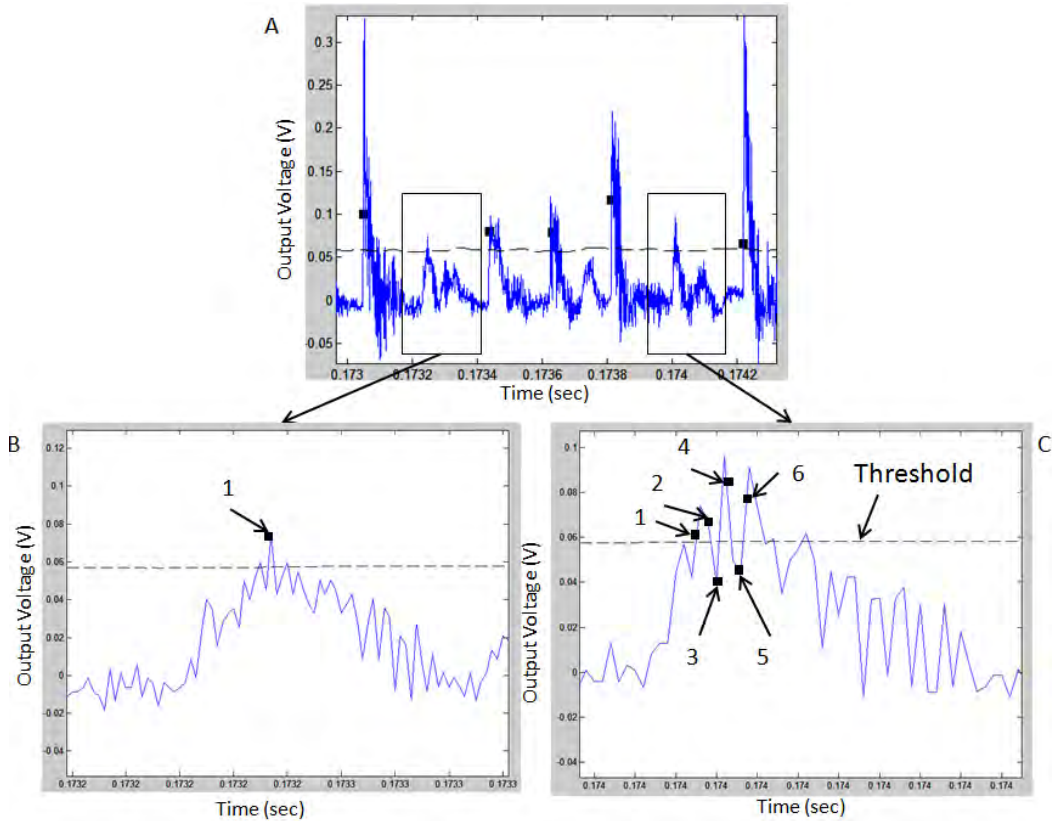


Figure 34. Zoomed in view of PCB data with wave speed calculation variables

The time of flight code with the originally determined values for the threshold, hold time, and PAT did not count the two zoomed in peaks in Figure 34B and C as can be seen because no black squares are present on those two peaks in Figure 34A. However, Figure 34B has a similar magnitude to two other peaks that are counted by the code in Figure 34A. The time of flight code does not count the peak in Figure 34C because the PCB data has a lot of variations in the data such that there may not be a large number of consecutive data points above the threshold value. As a result, the sensitivity of the wave speed to the PAT value is substantial, because although there could be many points that are above the threshold value, the points may not be consecutive points because points in between the points above the threshold value lie below the threshold. For example, in Figure 34C, 4 points (points 1, 2, 4, and 6), lie above the threshold,

so the time of flight code should read that as a detonation as long as the PAT is 4 or under.

However, due to the presence of points below the threshold (points 3 and 5), the code can only read the peak as a detonation for a PAT value of 2 and under. Thus, the higher the PAT value for the PCB data, the more likely it will be that a detonation event will not be recorded due to the variability of the PCB data, and the data will be aliased such that a lower detonation velocity is reported than actually occurred during the run.

Aliasing can also occur if the number of PATs is too high because the time of flight code will count the same detonation twice, resulting in a large number of high velocity detonations occurring, as seen in Figure 35. Because of this, it was important not to choose a PAT for the data reduction too high or the velocities calculated from the PCB data would over predict the velocities of the run.

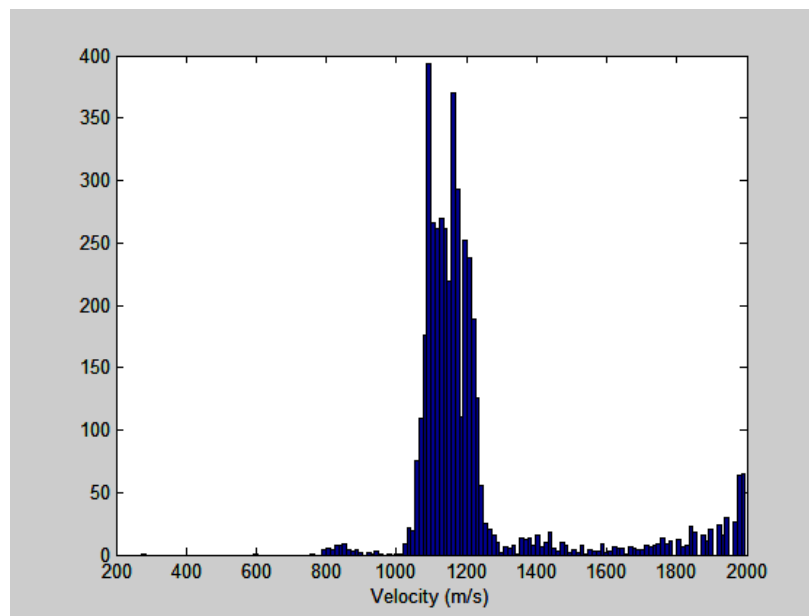


Figure 35. Histogram showing high speed detonation aliasing for a threshold of 1 standard deviation, a points above threshold of 1, and a hold time of 120 μ s

E. PCB and Kulite Data Comparison

The Kulite data does not have the issues that the PCB data does when using the time of flight code because the peak pressures occur more gradually, with fewer variations and more consecutive points above the threshold for each peak. A comparison of the Kulite data with the PCB data can be seen in Figure 36.

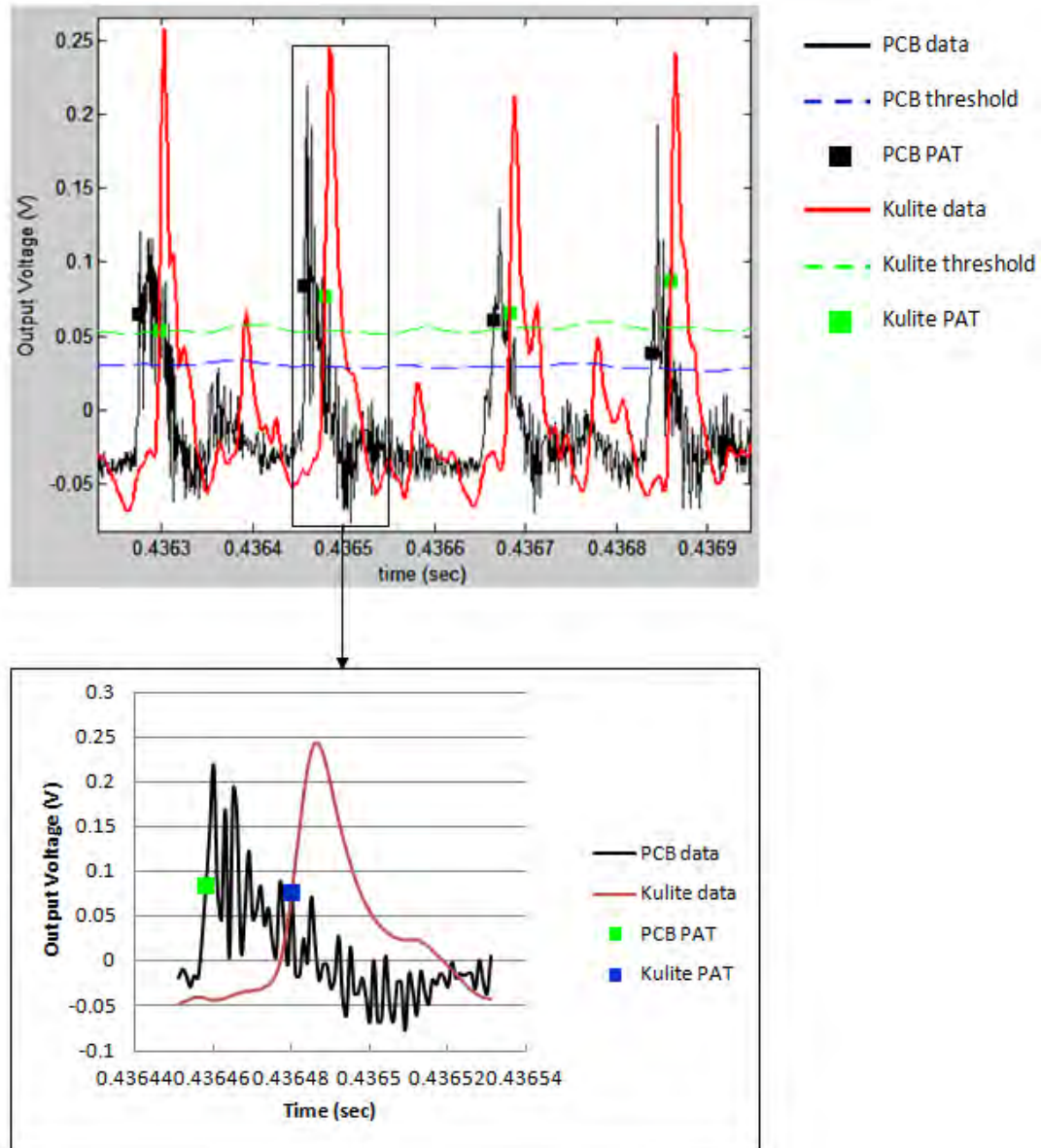


Figure 36. Kulite and PCB data comparison

The Kulite output voltages were reduced 10X for comparison with the PCB data. The Kulite response time was slower being that its rise time is higher than the PCB, but the response was much smoother. This accounts for the Kulite data being similar regardless of the number of PATs chosen because the Kulite pressure transducer reads many consecutive PATs for each peak, whereas the PCB data does not read as many consecutive PATs because some of the data falls below the PCB threshold due to the large variations in the data. The time difference between the Kulite and PCB PAT varied stochastically over the runs, but both the PCB data and the Kulite data recorded each detonation pass consistently, with the PCB always responding before the Kulite data. The first Kulite PAT did not consistently line up with a specific PCB data point after the PCB PAT, but the number of points between the data consistently remained below 10 points, which equates to 10 μ s. Because the Kulite and PCB differences were negligible, it was concluded that the difference in wave speed velocities between the two data sets was primarily due to the data reduction techniques used in the time of flight code. For the sensitivity analysis performed and presented in Figure 33, the Kulite and PCB average wave speed had the lowest percent difference for a PAT value of 2 for the PCB data. A PCB PAT value of 2 also gave a histogram with the least amount of data points outside of the primary detonation wave speed band as seen in Figure 37.

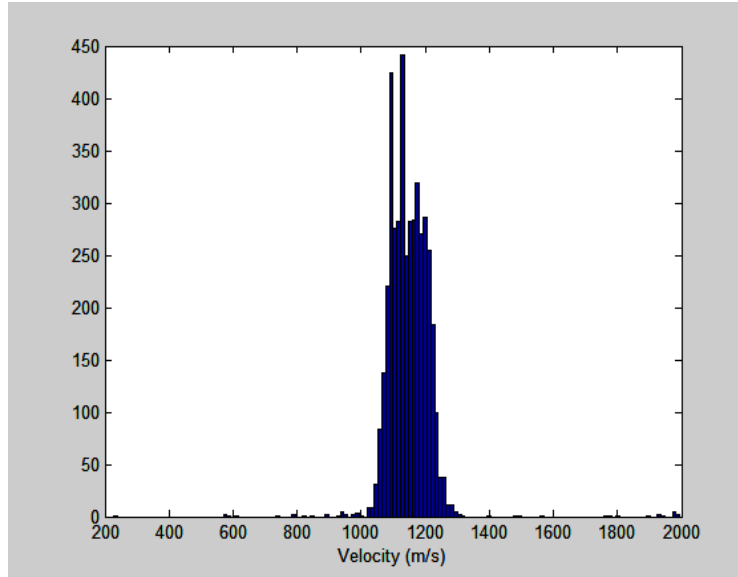


Figure 37. Histogram of detonation wave speeds for a threshold of 1 standard deviation, a points above threshold of 2, and a hold time of 120 μ s

F. Chosen Data Reduction Values

The final data reduction values for the Kulite and PCB data are shown in Table 3.

Table 3. Values used in time of flight code for wave speed data reduction

		Time Hold (μ s)	Threshold (st dev above avg)	Points Above Threshold
Initial	Kulite	120	1	4
	PCB	100	1	4
Final	Kulite	120	1	4
	PCB	120	1	2

The difference between the Kulite and PCB wave speeds reduced greatly when using a PAT of 2 for the threshold value. The percent error in the PCB data also reduced when moving from a PAT value of 4 to 2. The time holds of the two different data sets were equal for consistency between the data sets. Using the initial wave speed data reduction values produced an average percent difference between the Kulite and PCB average wave speeds of 9.10% with a standard deviation of 4.21%; by changing the PCB PAT to 2, the average percent difference between the Kulite and PCB average wave speeds was reduced to 0.83% with a standard

deviation of 0.70%. A full comparison of the wave speed results of the different data reduction methods is available in Appendix A.

G. Kulite Peak Pressures

The peak pressures of the Kulite data were found using MATLAB to determine the average peak pressures of the detonation during each test run. Figure 38 shows the data points treated as the peak pressures.

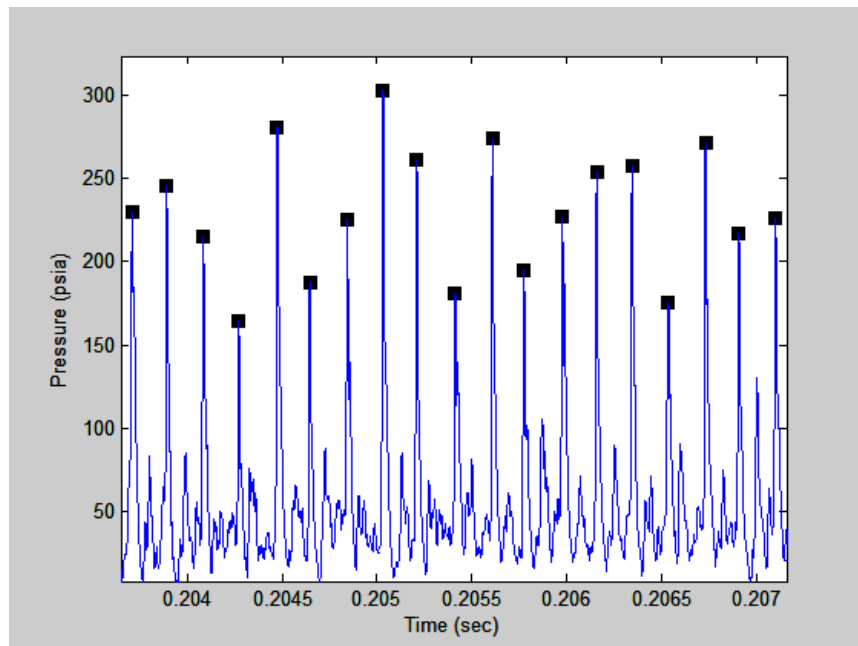


Figure 38. Peak pressures of Kulite data for the RDE run at $\dot{m}=46.1$ and $\phi=1.07$ with the 1.5 in. nozzle installed

The code picked out each peak pressure, denoted by the black square in Figure 38, by comparing a given data point on a peak with the next data point. If a data point had a larger value than the next consecutive data point, it was treated as the peak pressure for that peak, and the code continued onto the next peak. Every peak pressure was stored and the average of the peak pressures was determined. The code also calculated the average pressure for all data points.

H. Turbine Testing

For turbine testing, the scan rate was varied from 1 MHz to 250 kHz or 500 kHz, depending on the length of the run. Because of this, the PCB data did not produce the same results because fewer data points occurred above the threshold. The code was changed to count a pressure peak as a detonation if either a single point was two standard deviations above the average or if two consecutive points were one standard deviation above the average. A comparison of these histograms is available in Appendix A.

6. Uncertainty

Uncertainty is determined by combining the bias error inherent in the measurement device with the precision error in the data, and is found via Eq. 2.

$$U_{Total} = \sqrt{U_{Bias}^2 + U_{Precision}^2} \quad (2)$$

Bias error comprises of the estimated maximum fixed error that arises from the data measurement technique, and precision error arises from the imprecision of the measurements (19). The bias error of the T-type thermocouples used to collect the compressor inlet and outlet temperatures is either 0.75% of the full scale (FS) value or 1.8 °F, whichever is greater. The pressure transducers have thermal issues affecting the data, with all important errors considered in Table 4.

Table 4. Bias uncertainty values for pressure transducers used during testing

	Accuracy	Hysteresis	Natural Frequency	Compensated Temperature Range	Thermal Zero Shift	Thermal Sensitivity Shift
Kulite Pressure Transducer	0.1% FS	0.5% FS	1000 kHz	80 °F-180 °F	1% FS/ 100 °F	1%/100 °F
Honeywell 100 psi Pressure Transducer	0.10% FS	0.05% FS	4.6 kHz	60 °F -160 °F	0.0025% FS/ °F	0.0025%/°F
Honeywell 200 psi Pressure Transducer	0.10% FS	0.05% FS	7 kHz	60 °F -160 °F	0.0025% FS/ °F	0.0025%/°F

The bias error for Kulite testing assumed an upper temperature limit of 480° to calculate the thermal zero and sensitivity shift because this temperature was nearly double the operating temperature range. For the turbine testing, the temperature of the pressure transducers was assumed to rise to 500°F during testing because a 1/8 in. diameter, 3.5 ft tube was used to give the pressure transducers a standoff in order to keep the thermal error low.

The sample precision error was calculated using Eq. 3, where t is determined based on the desired confidence interval and S_x is the standard deviation of the sample.

$$P_{sample} = t * S_x \quad (3)$$

The value of t was chosen to be 2 for all uncertainty calculations because this gave a 95% confidence interval for sample sizes larger than 30 (19). The total sample error for the Kulite data was ± 20 psi ($\sim 9\%$) at the peaks and ± 5 psi ($\sim 8.8\%$) for the baseline pressure. The total sample error for both the turbine inlet and outlet was ± 1 psi, and the total sample error for the compressor inlet and outlet was ± 0.2 psi and ± 0.8 psi, respectively. The total sample data error is presented in Appendix B. in the form of error bars on the data.

Equation 4 was used for determining the precision error for a mean value, where n is the number of times the variable was measured.

$$P_{mean} = \frac{t * S_x}{\sqrt{n}} \quad (4)$$

The mean error for the turbine pressure measurements was kept under 1% for all compressor pressure measurements and under 3% for all turbine measurements.

The uncertainties in the total mass flow rates, air mass flow rates, fuel mass flow rates, and equivalence ratios were calculated by Russo (2), who also developed the uncertainty analysis

for the average wave speeds. A full list of all average wave speed errors for the nozzle and turbine testing is available in Appendix B.

IV. Results

1. 1.5 in. Nozzle Testing

A. Kulite Pressure

Nozzle testing was accomplished to determine the effect of back-pressurization on RDE operability. Kulite pressure data was taken and compared to RDE runs with and without the 1.5 in. nozzle. The typical pressure data for the unmodified RDE and the RDE with the nozzle can be seen in Figure 39 and Figure 40, respectively.

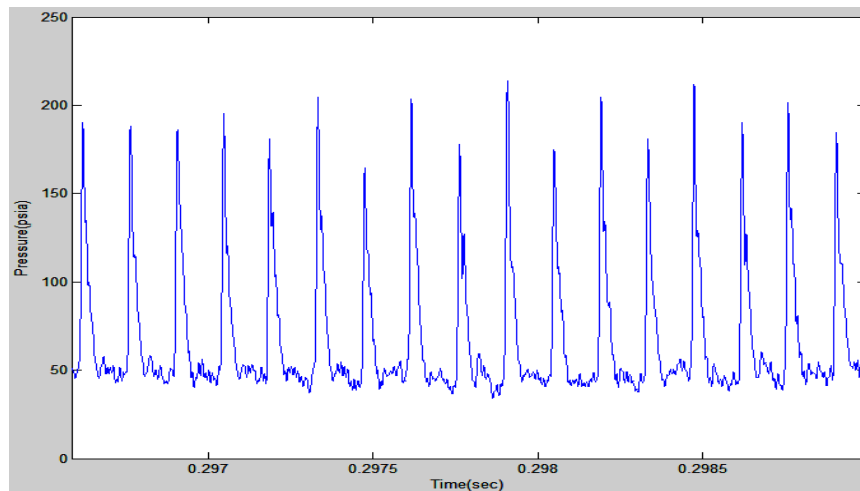


Figure 39. Kulite pressure data for unmodified RDE operation at $\dot{m}=48.0$ lbm/min and $\phi=1.4$

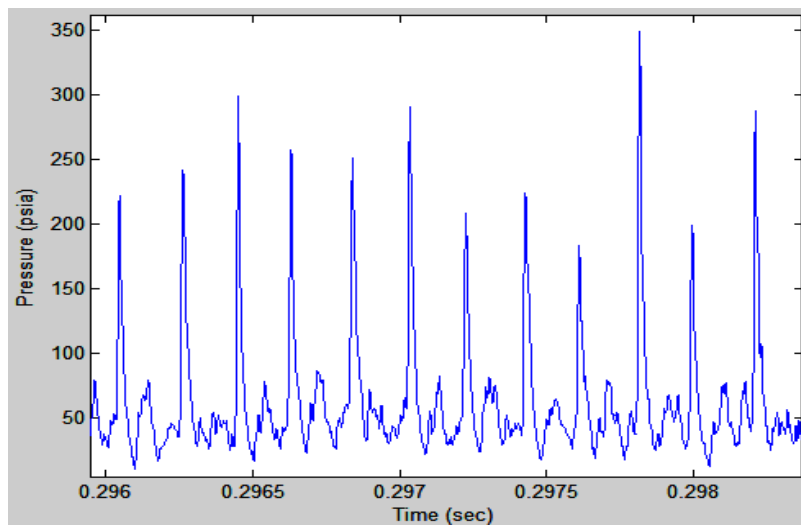
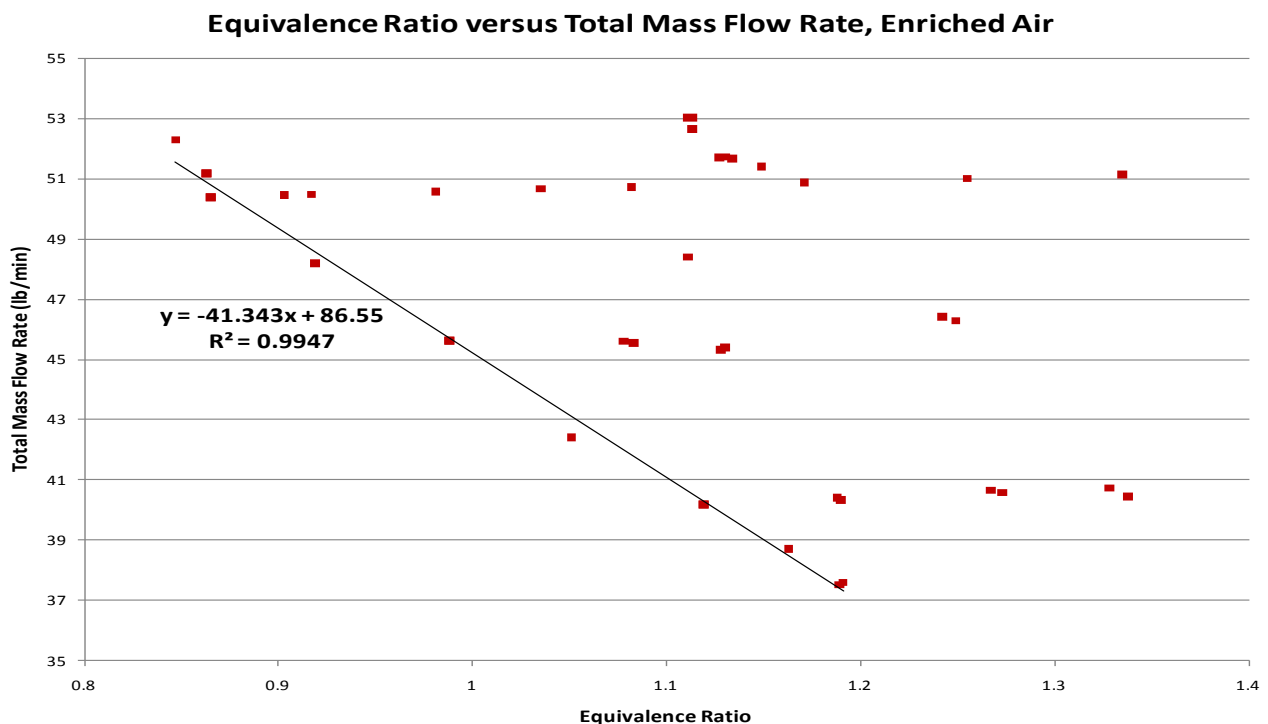


Figure 40. Kulite pressure data for RDE operated with 1.5 in. convergent nozzle at $\dot{m}=48.5$ lbm/min and $\phi=1.02$

The unmodified RDE run (Figure 39) has a consistent pattern, with peak pressures between 180 and 217 psia and a baseline pressure that remains quasi-steady at 45 psia. Peaks for the RDE with the nozzle (Figure 40) vary more than the unmodified RDE from 123 to 364 psia, and the baseline pressure fluctuates between 11 and 76 psia. The circumferential detonation velocities, found by dividing the circumference of the detonation chamber by the time between peaks showed speeds without the nozzle at 1,660 m/s and 1,325 m/s for the RDE with the 1.5 in. nozzle. Faster detonation speeds correlate to more consistent engine operation as well as operation closer to the C-J conditions.

B. Operational Space

Previous testing by Russo (2) produced an operability map for the RDE as shown in Figure 41.



Testing conducted with a 1.5 in. nozzle with enriched air produced the operability map shown in Figure 42.

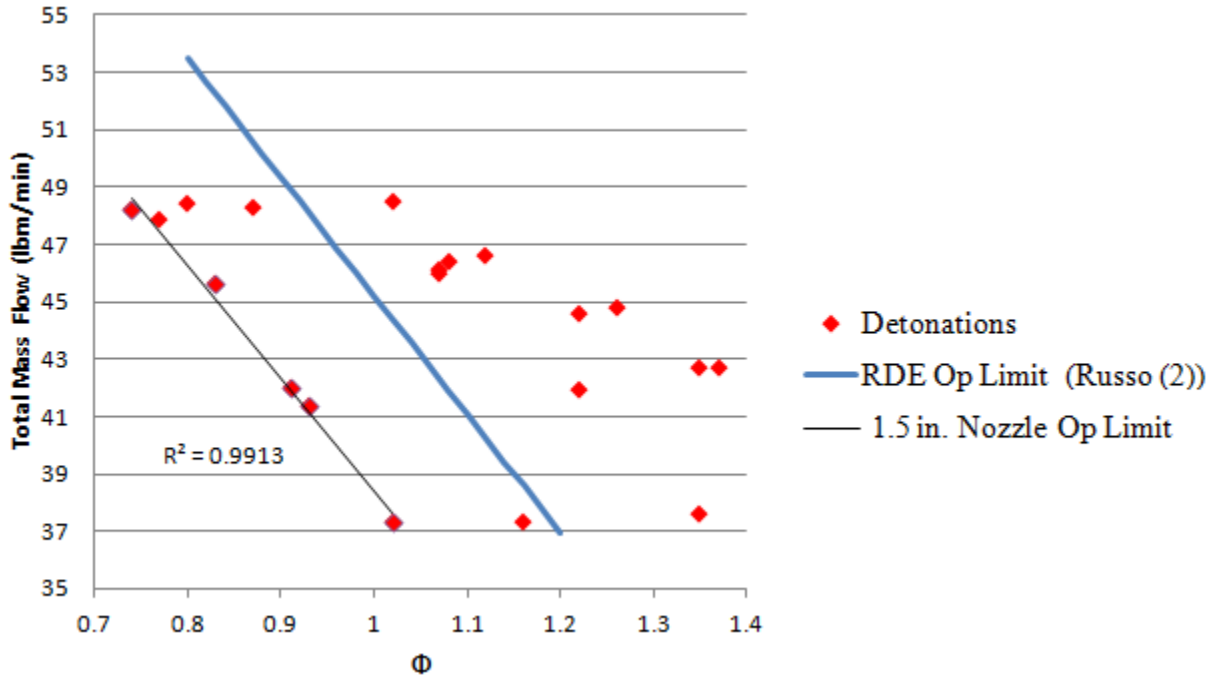


Figure 42. RDE with 1.5 in. diameter convergent nozzle operating map using 23% oxygen enriched air

For both operating maps, the operational limits are denoted by the two trend lines shown in Figure 42. The operability limit denotes the transition between successful and unsuccessful detonation runs, with unsuccessful runs occurring below and to the left of the operability limit, and successful runs occurring to the right and above of the operability limit. The heavy blue line in Figure 42 is the RDE operating limit from Figure 41 (Russo (2)). As seen in Figure 42, the RDE operating map with the convergent nozzle was able to run at lower ϕ ratios for a given mass flow rate. This lower limit capability was beneficial for integrating the JetCat turbine with the RDE since lower ϕ ratios result in lower operating temperatures, which reduced the risk of

overheating the JetCat turbine in the early stages of testing, and provide a larger operational range for throttling the engine.

Although the convergent nozzle allowed for RDE operation at lower ϕ , the nozzled RDE was not able to achieve mass flow rates as high as the unmodified RDE due to a malfunction with the pre-detonator. Higher mass flows may be achievable by increasing the pressures feeding the pre-detonator to counteract the larger pressurization of the chamber due to the nozzle that may prevent the pre-detonator from firing correctly. Increasing the feed pressures to the pre-detonator will ensure a proper fire sequence for the pre-detonator which will then ignite the chamber at higher mass flows.

C. Wave Speed Trends

The average wave speed of the run depended linearly on the equivalence ratio as shown in Figure 43.

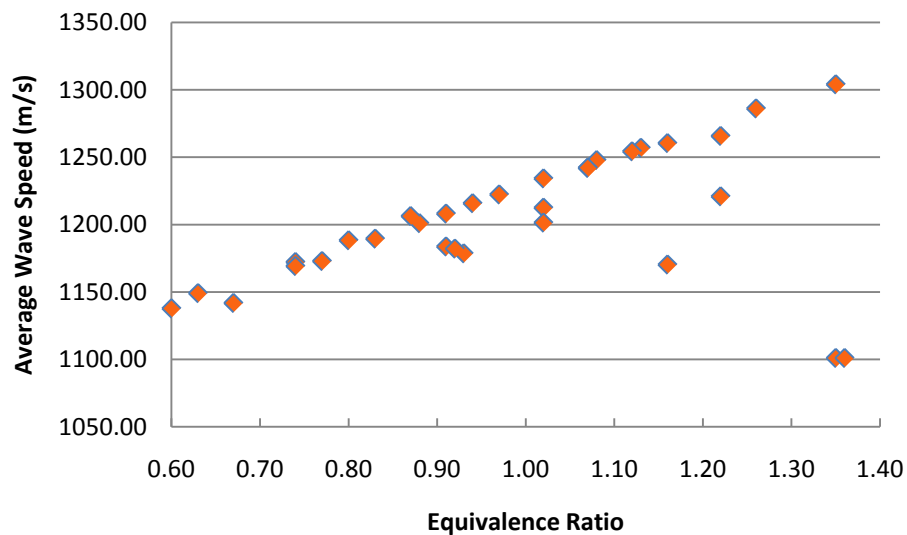


Figure 43. Dependence of average wave speed on equivalence ratio for successful detonation runs for the 1.5 in. nozzle using enriched air

The equivalence ratio, which provided the same linear trend with the average wave speed as the equivalence ratio, was the primary variable discovered that produced a trend in RDE wave speed performance. The RDE wave speed increases 13% from an equivalence ratio of 0.6 to 1.36, indicating a small dependence of wave speed on equivalence ratio.

D. RDE Start Up Transients

Both a video recording and a high speed camera were used to take video of the nozzled and open exhaust, particularly focusing on the shock diamonds that formed when the nozzle was added to the RDE. The high speed camera was also used to view the unsteady nature of the RDE start up. A comparison of the footage for both steady operation and startup is shown in Figure 44 and Figure 45.

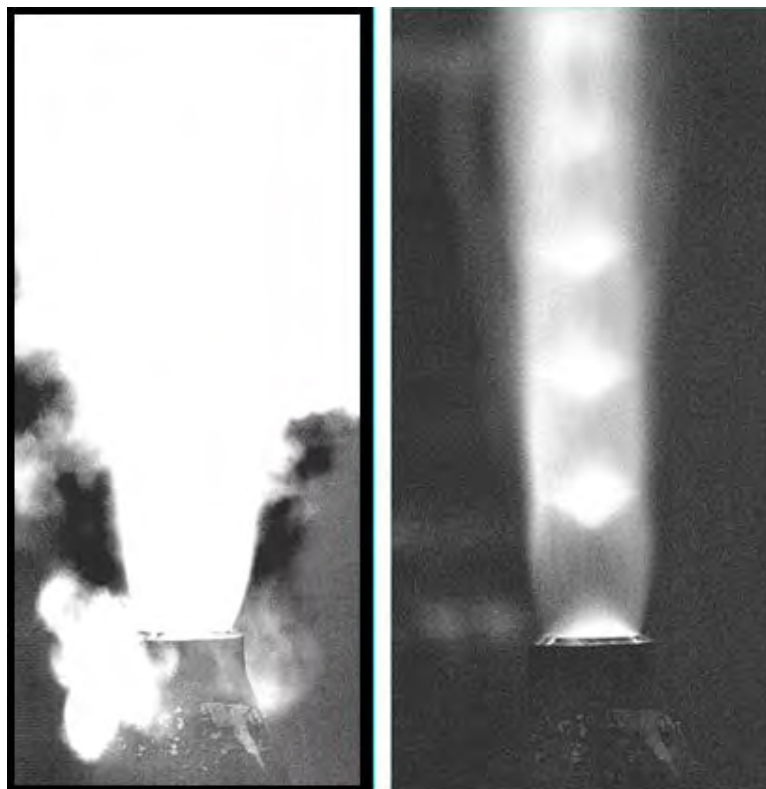


Figure 44. High speed camera comparison of startup and steady operation for the 3 in. RDE with 1.5 in. nozzle

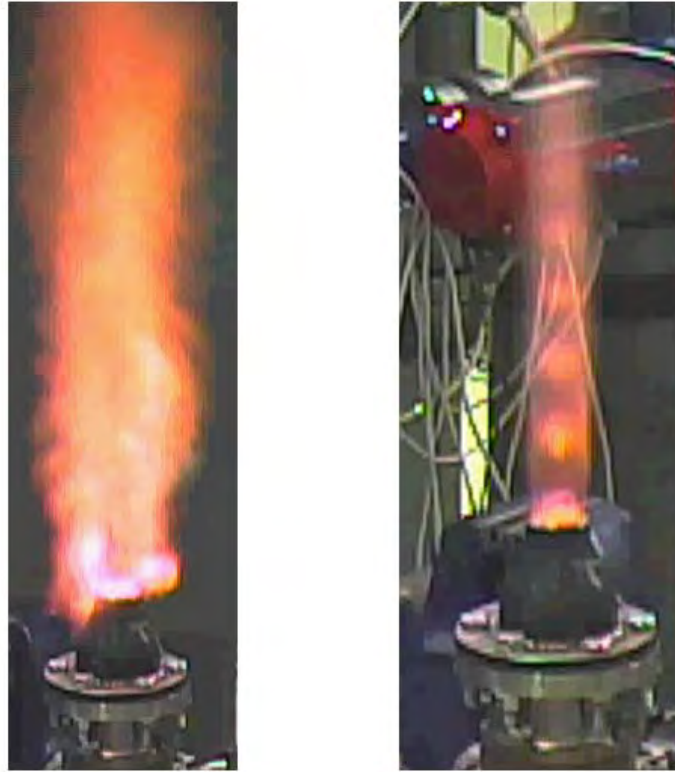


Figure 45. Video recording comparison of startup and steady operation for the 3 in. RDE with 1.5 in. nozzle

A large flame develops at ignition because air and fuel are flowed through the RDE before the pre-detonator ignites the reactants in the chamber. Once ignited, the fuel and air released prior to ignition are burned outside of the RDE detonation channel, causing a large flame outside of the nozzle.

E. Turbine Integration

The 1.5 in. nozzle testing with the RDE produced several insightful conclusions that were used when integrating the turbine for testing. First, without external control, the RDE startup could feed reactants into the plenum and turbine, which upon ignition in the combustion chamber using the pre-detonator could cause turbine burn and thus turbine failure. To prevent reactants flowing into the plenum and turbine, the fuel establishing time was minimized. By reducing the

fuel establishing time, fewer unburned reactants would enter the plenum before the pre-detonator fired. Second, the addition of the nozzle had a caused slower detonation velocities in the RDE. Although the detonation velocities were lower, the RDE operational space became less restrictive, with successful runs occurring at lower equivalence ratios for the same mass flow rate. Third, the shock diamonds indicated high pressures, at the nozzle exit, with the nozzle throat pressure calculated to be 2 atms by the shock diamond analysis tabulated in Appendix C for an RDE run with a mass flow rate of 41.9 lbm/min, and a ϕ of 1.22.

2. 1.17 in. Nozzle Testing

A. Detonation Channel Pressure

A second nozzle with a diameter of 1.17 in., which was calculated to be an area equivalent to the area of the turbine stator vanes, reduced the exit area of the RDE by 50%. A 200 psi pressure transducer was used to determine the average pressure in the detonation channel. The detonation channel pressure, similarly to the total pressure at the nozzle exit, helped to determine the operability of the JetCat with the 3 in. RDE. The pressure transducer response during a run is shown in Figure 46.

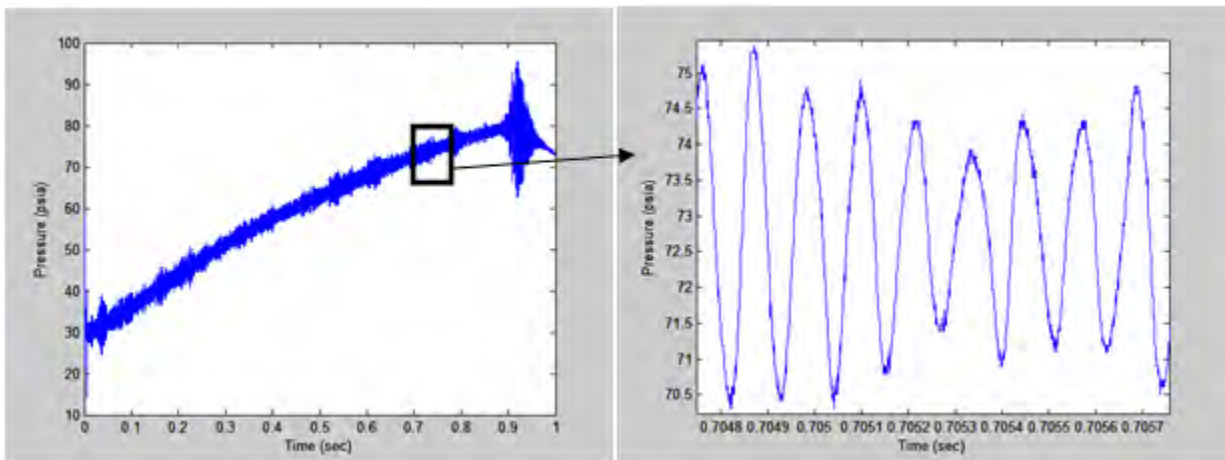


Figure 46. Pressure transducer 0.70 in. from detonation channel bottom for 1.17 in. nozzle testing using standard air at $\dot{m}=42.4$ lbm/min and $\phi=1.06$

As seen in Figure 46, the combustion chamber pressure rose slowly over the duration of the run and began to settle at an average pressure near the end of the test. Sinusoidal oscillations occurred in the pressure data with an average frequency for the runs of 2.15 kHz. The amplitude remained below 3 psia for most of the run, but increased to 15 psia after 0.9 seconds. The amplitude of the pressure oscillations increased at the end of the run for every test.

The pressure reading at the end of the test was considered the average pressure for the run. The average pressure for each run was recorded and plotted versus the mass flow rate as shown in Figure 47. The average chamber pressure increases linearly with an increase in the total mass flow rate. The detonation channel pressure data was useful for turbine testing because the detonation channel pressures provided starting parameters to work with in determining where to operate the turbine.

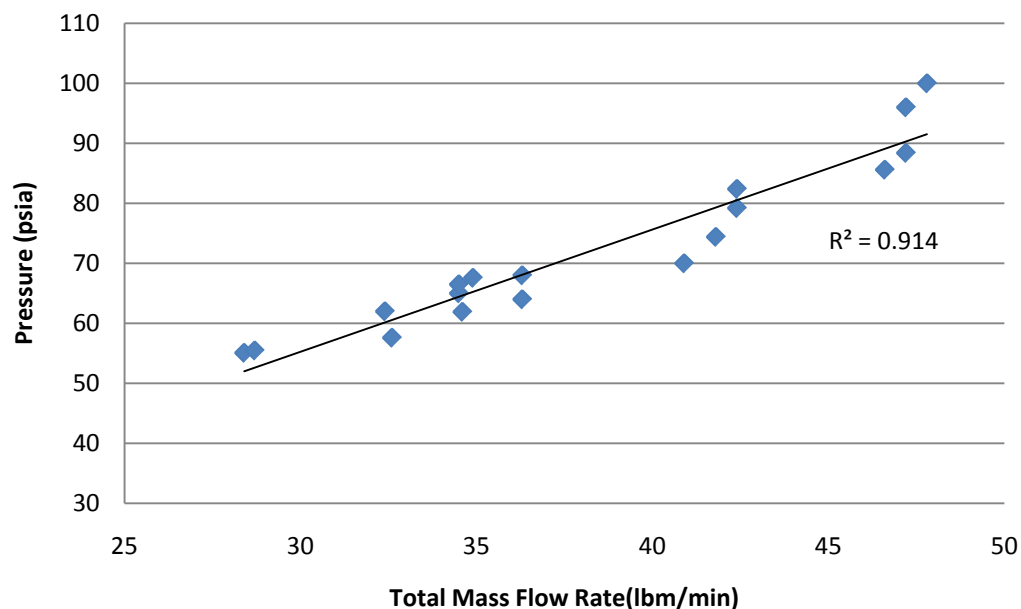


Figure 47. Total mass flow rate impact on average detonation channel pressure for 1.17 in. nozzle testing using standard air

B. Operational Space

The RDE run with the 1.17 in. nozzle was tested using standard air, and produced a smaller operational space, shown in Figure 48, than the RDE run with the 1.5 in. nozzle using 23% oxygen enriched air.

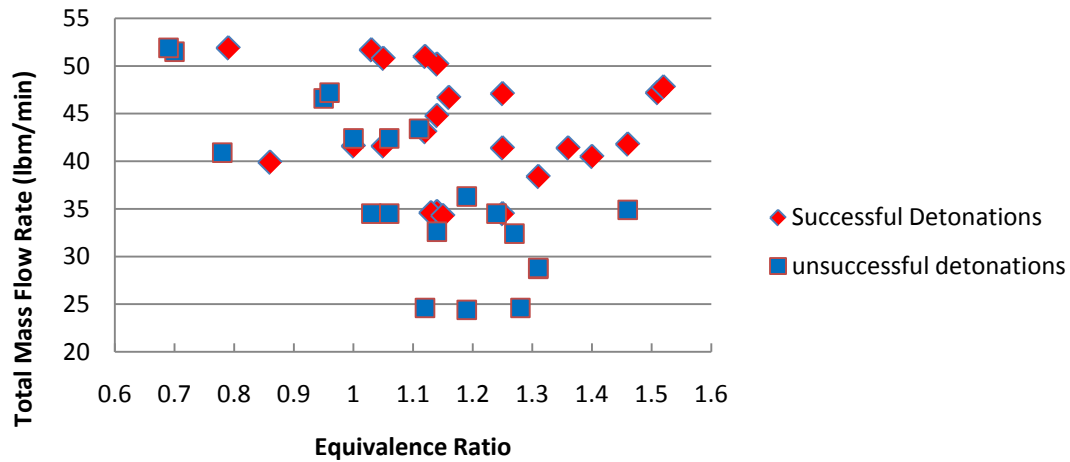


Figure 48. RDE operating map with 1.17 in. diameter convergent nozzle section using standard air

An operational space was initially developed for the three in. RDE run on standard air and hydrogen by Russo (2) and was later updated by Suchocki (13), shown in Figure 49.

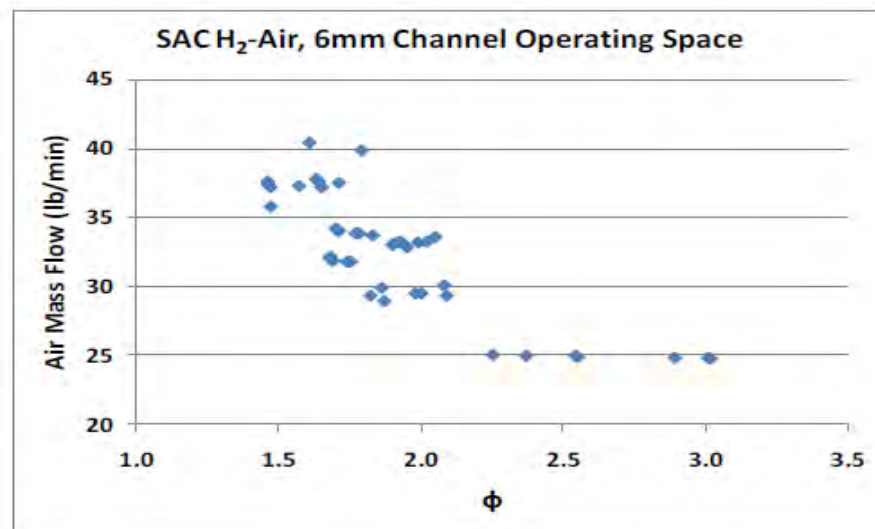


Figure 49. RDE operating range for hydrogen and standard air

The differences between the operational spaces between the 1.17 in. nozzle in Figure 48 and the RDE run on standard air in Figure 49 are similar to those found between operational spaces of the 1.5 in. nozzle and the RDE run on enriched air seen in Figure 41 and Figure 42. Two different nozzles (1.5 in. and 1.17 in.) tested under two varying conditions (standard air vs. enriched air) increase the confidence that nozzles change the RDE operation space. No clear operability limits were determined for the nozzled standard air testing due to the existence of detonation runs and non-detonation runs overlapping on the operational space. There still seems to be a somewhat linear boundary between the equivalence ratio and the mass flow rate such that for higher mass flow rates, detonations are achievable with lower equivalence ratios. Comparing the operational space of the RDE in Figure 49 with that of the 1.17 in. convergent nozzle in Figure 48, for the same mass flow rates, a lower equivalence ratio was achievable with the nozzle attached, or conversely, for the same equivalence ratio, a lower mass flow rate was achievable.

Testing performed by Suchocki (13) discovered that below a fuel flow rate of 1.55 lbm/min, a detonation was not possible for standard air runs. The 1.17 in. nozzle data showed a similar trend, as seen in Figure 50.

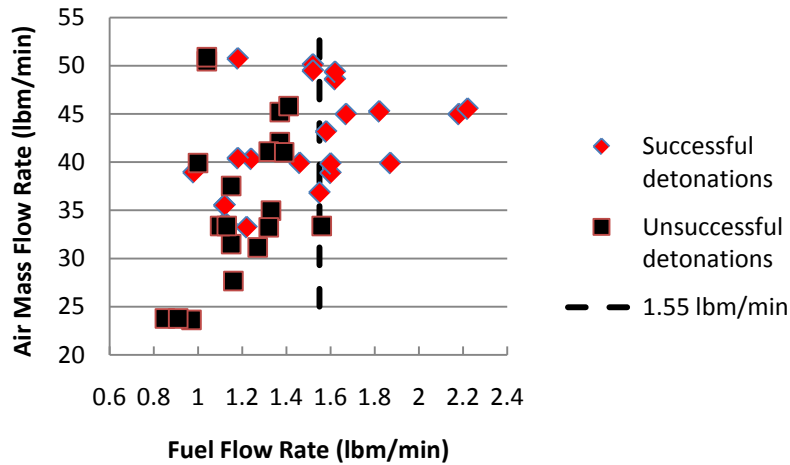


Figure 50. Fuel flow rate limit for the RDE with the 1.17 in. convergent nozzle run with standard air and hydrogen

Although detonations occurred below the value determined by Suchocki (13), every run but one occurring above the 1.55 lbm/min fuel flow rate was a successful detonation run.

Suchocki did not see any successful detonation runs below the 1.55 lbm/min rate as is seen in Figure 51.

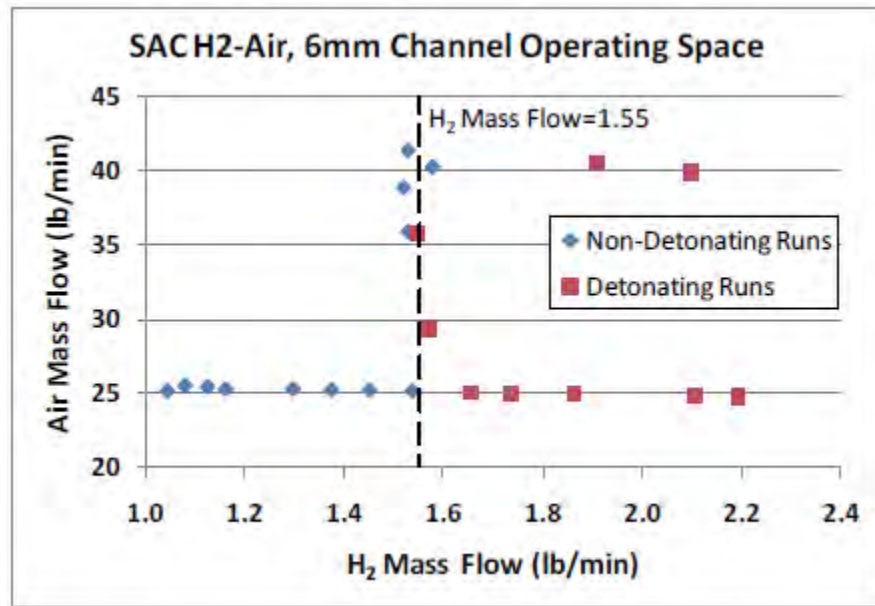


Figure 51. RDE operating range for hydrogen-air with 6mm channel and 0.123 in² gross oxidizer injection area with a defined transition (13)

Though a similar trend occurs between the RDE run with and without the 1.17 in. nozzle, the runs with the 1.17 in. nozzle were sometimes successful below a fuel flow rate of 1.55 lbm/min and were able to achieve higher air mass flows rates with a fuel flow rate of 1.55 lbm/min, which equates to lower equivalence ratios since for a constant fuel flow rate, as the air mass flow rate increases, the equivalence ratio decreases.

C. Wave Speed Trends

The 1.5 in. nozzle, enriched air average wave speeds were compared with the 1.17 in. nozzle, standard air runs, shown in Figure 52. For both the 1.5 in. nozzle and the 1.17 in. nozzle, the average wave speed increases linearly with equivalence ratio for all mass flow rates. All enriched air runs (1.5 in. nozzle) had higher average wave speeds than the standard air runs (1.17 in. nozzle). A drop off occurs for extremely high equivalence ratios, but more data is needed to confirm that the average wave speed will decrease at high equivalence ratios.

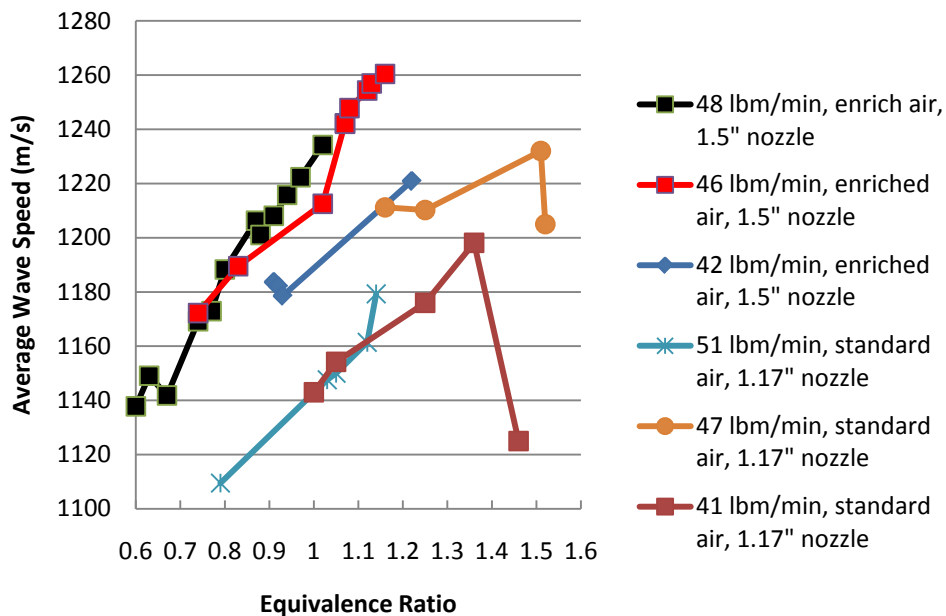


Figure 52. Average wave speed dependence on the total mass flow rate, equivalence ratio, and the percentage of oxygen used for testing

RDE performance was determined using three PCBs separated by 120 degrees around the RDE. The performance of the RDE was primarily impacted by the equivalence ratio of the run, with variations in equivalence ratio having a mostly linear trend with the average wave speed for the run shown in Figure 53.

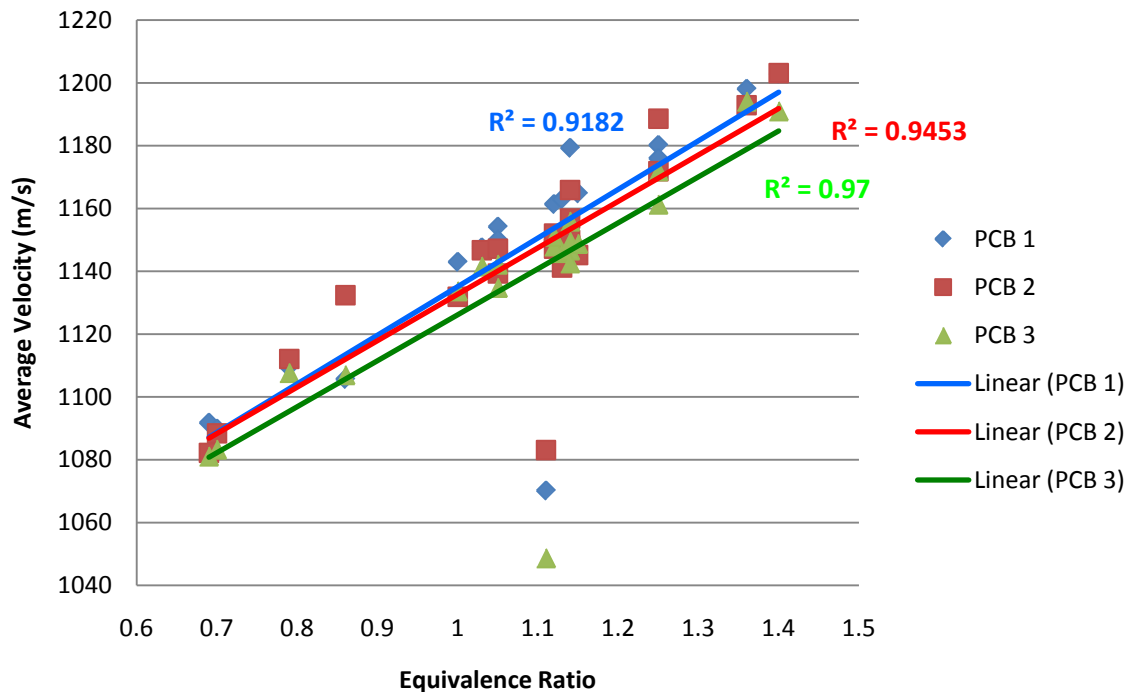


Figure 53. Impact of equivalence ratio on RDE performance for 1.17 in. nozzle using standard air and hydrogen

The data contained only one run outside of the linear trend of the data. Thus, these data points were considered outliers, and the linear trend lines established and the reported R^2 values were determined by excluding the outlier run. The PCBs varied little in the value for average wave speed, with a maximum difference of 3.18%. An increase in equivalence ratio of 100% produced an increase in the detonation velocity of only 10%. Equivalence ratio has a limited impact on the performance of the RDE, and this is beneficial because lower equivalence ratios

allow for less fuel burn, and reducing fuel burn with a minimal performance reduction can reduce operational cost.

Three primary wave speed modes were discovered for the 1.17 in. nozzle run conditions. First, successful detonations produced a consistent wave speed throughout the duration of the run as shown in Figure 54.

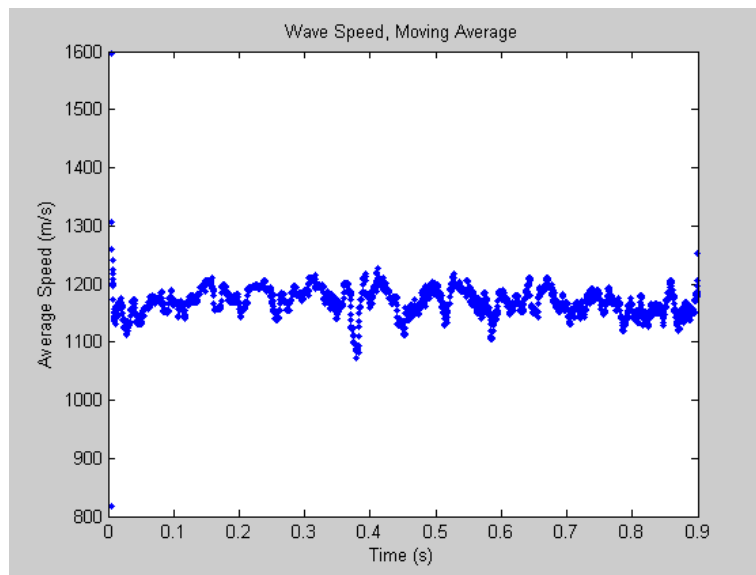


Figure 54. Wave speed 51 point moving average for successful detonation RDE runs with the 1.17 in. convergent nozzle and standard air

Some fluctuations in wave speed occur in Figure 54, but overall the wave speed stays consistent and a detonation exists in the channel for the duration of the run. Second, unsuccessful runs produced two types of modes. The first mode was similar to that of the detonations seen in Figure 54 except that the wave speed is much lower and cannot be categorized as a detonation. The third mode was an unsuccessful run that produced detonations for some of the run, but not enough to get the average wave speed high enough to be considered a successful detonation run. The runs with a dip in average wave speed were considered to be partial detonation runs, and had a wave speed run profile as seen in Figure 55.

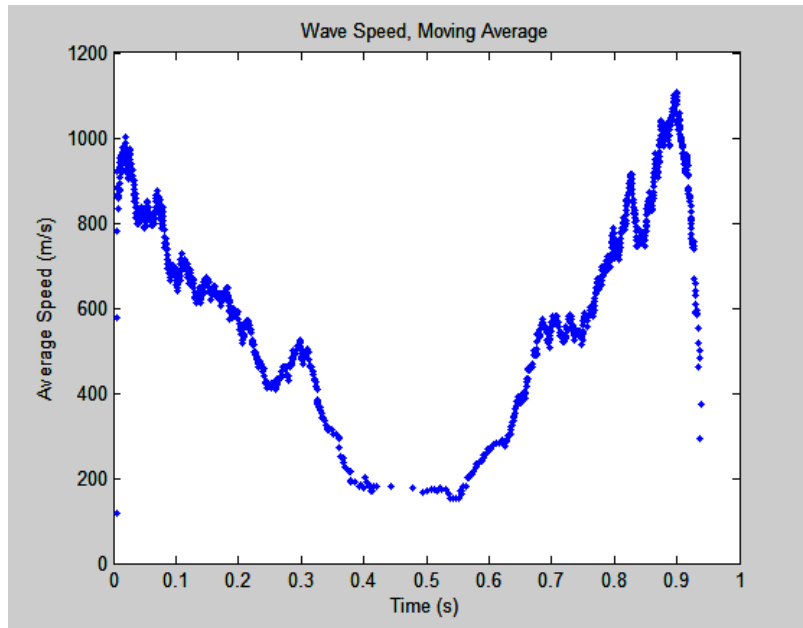


Figure 55. Wave speed 51 point moving average profile for partial detonation RDE runs with the 1.17 in. convergent nozzle and standard air

In the partial detonation runs, the wave speed initially was high, dropped near the midpoint of the run, but then the detonations began to reinitiate toward the end of the run. The reinitiating of the detonation toward the end of the run was an interesting phenomenon, but due to thermal management issues, runs were limited to 1 second, and no conclusion could be made as to whether the detonation would reinitiate and produce a consistent wave speed, continue to oscillate between detonations and deflagration in the chamber in a periodic or stochastic manner, or cease to detonate at all.

D. Nozzle Pressures

Due to the discovery of the shock diamonds upon initial testing, it was desired to see the pressure changes that occurred from the nozzle base to the nozzle throat to determine the Mach number at the RDE exit plane as compared to the nozzle throat. If the pressure increased from the nozzle base to the throat, the nozzle would have acted as a supersonic diffuser for a supersonic exit flow from the RDE that is slowed to a lower supersonic or sonic value at the

nozzle throat. If the pressure decreased from the nozzle base to the throat, the nozzle would have acted as an expander for a subsonic exit velocity that is sped up to a sonic velocity at the nozzle throat. The numerical study performed by Shao et al. (14) determined that the RDE contained subsonic flow in front of the nozzle throat.

The nozzle pressure data, seen in Figure 56, increased over the 1 second run until achieving a quasi-steady state value at the end of the run. The average pressure was determined using the detonation channel pressure method where the average pressure for the run was considered to be the value at the end of the test.

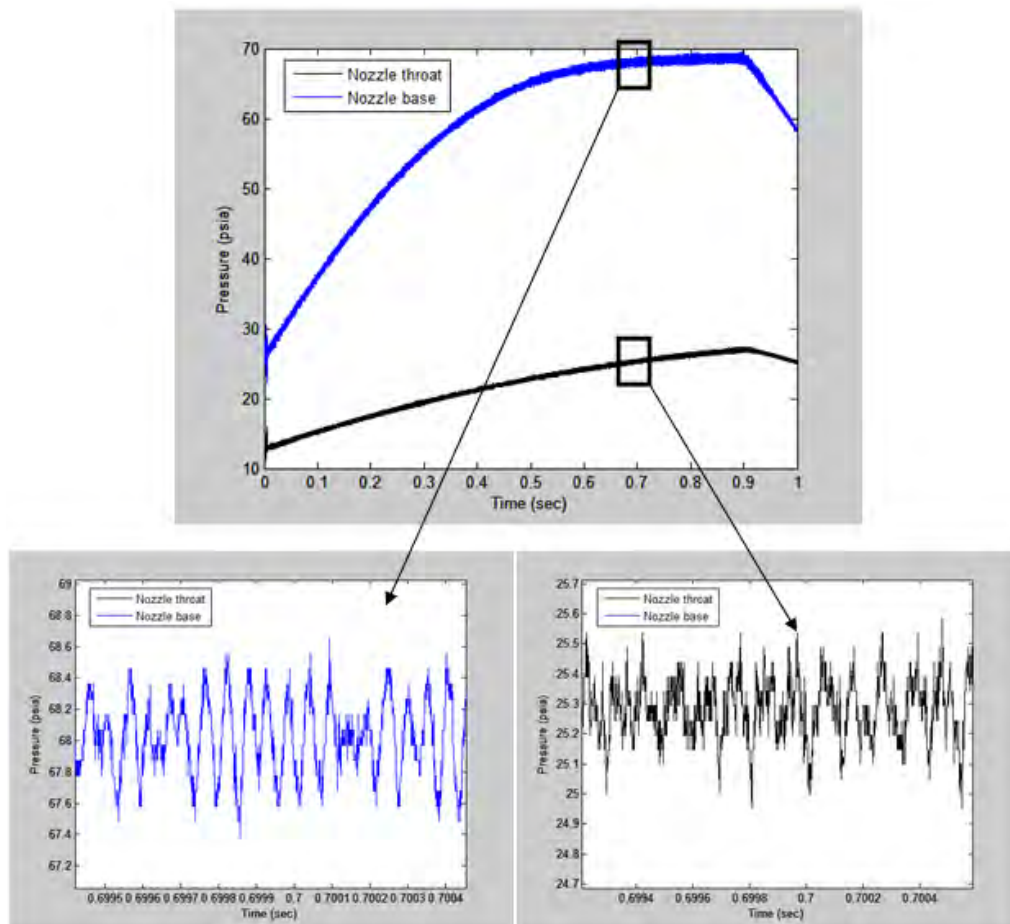


Figure 56. Nozzle base and throat pressures at $\dot{m}=34.3$ lbm/min and $\phi=1.15$

As with the detonation channel pressure in Figure 46, the nozzle base and throat measurements experienced oscillations during the run. The frequency of the nozzle pressures could not be accurately determined because the data did not closely approximate a sine wave whereas the detonation channel pressure in Figure 46 had a consistent sine wave pattern. The amplitude of the pressure oscillations was small, staying below 1 psia for each run.

The average baseline pressures produced a linear increase with the total mass flow rate similarly to the RDE chamber pressure shown in Figure 47. The values from Figure 47 are also plotted on the graph shown in Figure 57 for comparison.

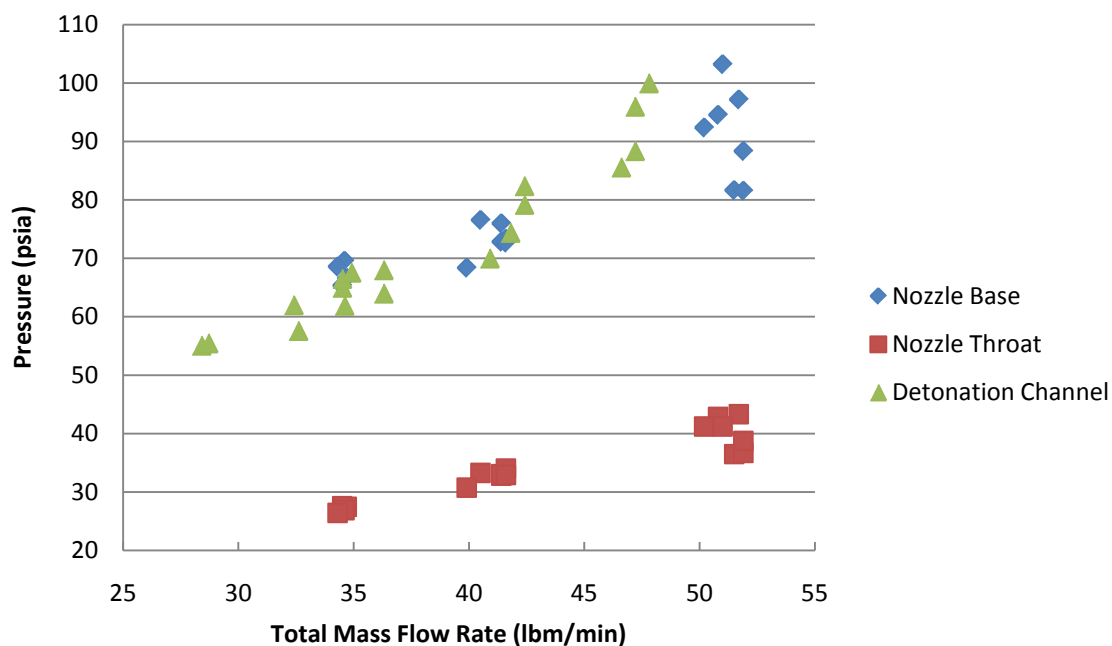


Figure 57. Pressure trends for RDE detonation channel and 1.17 in. nozzle in the detonation channel and at the nozzle base and nozzle exit

For all mass flow rate conditions, the nozzle throat pressure is less than the nozzle base pressure, and the detonation channel pressures coincide well with the nozzle base pressures. The results show that the nozzle acts as an expander and brings the RDE exhaust from a subsonic

velocity to the local speed of sound at the nozzle exit. Because the pressure at the nozzle exit is greater than the atmospheric pressure, the nozzle is underexpanded and produces shock diamonds as was seen for all successful detonation tests. The pressure ratio of the throat pressure to the ambient pressure ranged from 1.8 to 2.94 for the various mass flows and equivalence ratios tested. The pressure ratio range coincides with an initial shock diamond analysis performed with the 1.5 in. nozzle using enriched air that predicted a throat-to-ambient pressure ratio of 1.8. Because the initial shock diamond analysis did not take into account all of the shock diamonds, it was predicted that the pressure ratios could be higher than 1.8, and the results of the pressure measurements show that the shock diamond analysis underestimated the pressure ratios.

E. Turbine Integration

Because of the startup transients seen by both the video recording and the high speed camera during the 1.5 in. nozzle testing, the 1.17 in. nozzle was tested with reduced fuel establishing times so as to minimize the amount of detonable products that would exist in the circular plenum before the ignition of the pre-detonator. All testing for the reduction of the fuel establishing time was conducted at an average total mass flow rate of 41.3 lbm/min and an equivalence ratio of 1.25; this point was chosen because it was in the middle of the operational space for the 1.17 in. nozzle and because preliminary calculations determined that a mass flow rate of approximately 40 lbm/min with exit temperatures and pressures similar to that of the RDE would choke the turbine. The pre-detonator was only fired once because if the detonation wave did not immediately ignite, more reactants would feed into the plenum before the pre-detonator was able to fire again, which would have increased the likelihood of igniting the reactants in the plenum, or if given enough time the reactants may have entered the turbine causing turbine burn. Minimizing the fuel establishing time reduces the equivalence ratio at the beginning of the run if

the establishing time is short enough, causing ignition of the reactants to be more difficult. The fuel establishing time was gradually reduced from its original value of 550 ms until a limit was determined where the reactants would not light because not enough fuel was present when the pre-detonator fired. The fuel establishing time was reduced from 550 ms to 90 ms, where a fuel establishing time of 90 ms consistently lit the reactants in the RDE during turbine testing.

The performance of the RDE was also a consideration when dropping the fuel establishing time. The average wave speeds for each run was determined to discover whether the detonation velocities reduced as the fuel establishing time was reduced. The average wave speeds remained largely unchanged, with detonation velocities varying between 1,166 and 1,203 m/s. Because the fuel establishing time made little difference on the average wave speed of the detonations, the primary concern was getting the RDE to light at the low fuel establishing times. The results from reduced fuel establishing time testing produced the last set of needed data to successfully integrate the turbine with the RDE.

The turbine inlet temperature was considered for turbine integration with the RDE because the hydrogen-air was used for fuel as opposed to a standard hydrocarbon such as JP-8. The adiabatic flame temperature for a hydrogen-air mixture was determined via Mattingly's Equilibrium Combustion of Ideal Gases program (20) to be between 2,300 and 2,400 K depending on the pressure, temperature, and equivalence ratio of the combustion. The maximum turbine inlet temperature of the JetCat was determined to be 1,460 K by performing a cycle analysis on the JetCat at the maximum compressor pressure ratio and RPM. Running the RDE exhaust into the JetCat turbine produced much higher turbine inlet temperatures, creating a survivability issue for the JetCat turbine. The primary objective of the research was to achieve quasi-steady state data to determine JetCat operability, so although JetCat survivability was

important, testing the integration of an axial turbine with a RDE for the first time ever was of more importance. Because of the higher turbine inlet temperature created by the RDE exhaust, the time between RDE runs was increased to help decrease the thermal load on the turbine.

3. Turbine Testing

A. Cold Flow Testing

Cold flow testing was conducted with the turbine to ensure that the lubricant system, control program, and all measurements were working before the RDE was fired. The engine RPM became stable under cold flow after 2 seconds, with the RPM varying from 45,000 to 60,000 for air mass flow rates of 33.4 lbm/min to 64 lbm/min, respectively. The air establishing time, or the time from that the air is flowed through the RDE before the pre-detonator was ignited, was set to 2.5 seconds so that the turbine RPM would be steady before the pre-detonator fired, and to reduce the load on the turbine once the RDE was fired. Achieving a cold flow steady state RPM before igniting the RDE helped the RPM reach a steady state value once the RDE was fired, which was advantageous due to the short run time. Bringing the RPM to a steady state value also provided a good baseline for data acquisition.

B. Operational Space

For RDE-turbine testing, the nozzle operational spaces were used to determine a starting point, and the turbine was initially operated in regions where detonations would not occur to get a baseline of operation for the turbine before running full detonation runs into the turbine. Figure 58 shows a comparison of all turbine testing points with the successful nozzle detonation runs. Figure 58 includes the successful nozzle detonations from Figure 42 and Figure 48, and the operability limits from Figure 41 and Figure 42.

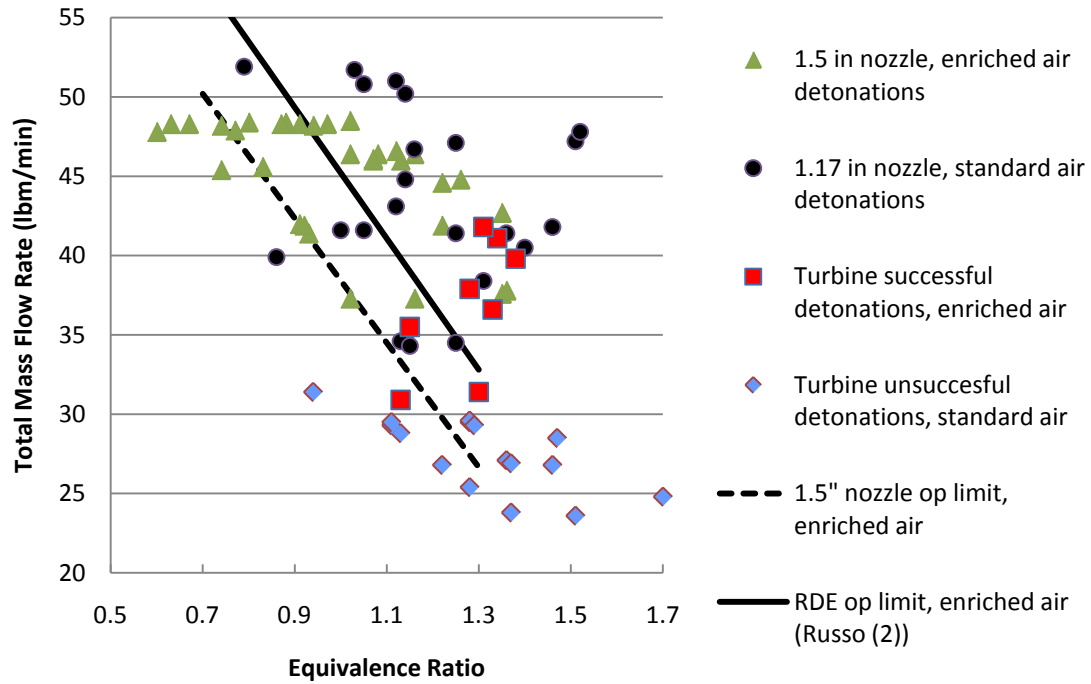


Figure 58. Turbine runs compared with 1.17 in. and 1.5 in. nozzle operational spaces

After initial testing with standard air, testing was switched to enriched air so that detonations could be achieved at lower equivalence ratios and mass flows. All successful detonation runs shown in Figure 58 were run with enriched air, and all unsuccessful runs were run with standard air except for one enriched air run which occurred at a $\dot{m}_{total} = 31.4 \text{ lbm/min}$ and $\phi = 0.92$. Once detonations were achieved at lower mass flow rates with enriched air and the turbine operability was consistent, testing was moved toward the middle of the RDE operational space (see Figure 58) to see the effect on turbine performance. The RDE had detonation runs with the turbine attached that occurred at lower mass flow rates and equivalence ratios than the RDE operation limit for enriched air shown in Figure 58, showing that the turbine expands the operational space of the RDE in the same manner as the nozzles due to the back-pressurization of the RDE.

C. Wave Speed Trends

The average wave speeds of the RDE run with the turbine also coincided with the wave speeds of the RDE runs with the nozzles attached, as shown in Figure 59.

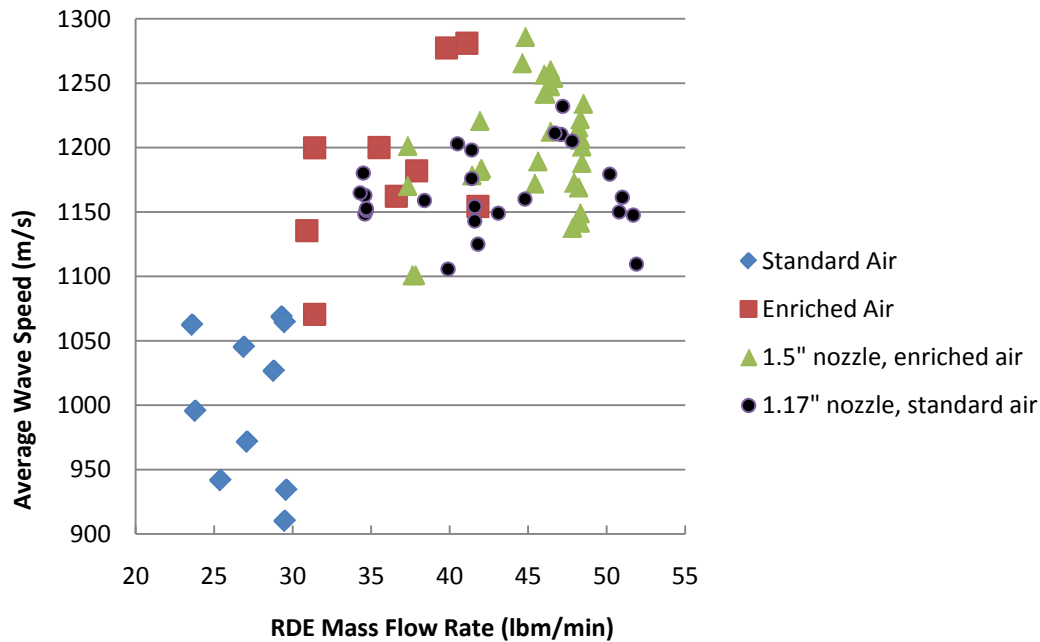


Figure 59. Comparison of turbine, 1.5 in. nozzle, and 1.17 in. nozzle average wave speeds

The average wave speeds show that successful detonation runs (average wave speed > 1,100 m/s) only occurred for the enriched air runs, but it also shows that the standard air runs were approaching detonations. Wave speed variations at given mass flows are determined by the equivalence ratio.

D. Turbine Pressures

During turbine testing, pressure measurements were taken at the inlet and outlet of both the compressor and the turbine. Fluctuations occurred in both the turbine inlet and outlet pressure measurements because of the unsteady flow coming out of the RDE. Analyzing the frequency response of the turbine pressure data, it was determined that the average frequency of the turbine inlet pressure measurement was 8.6 kHz, and the average frequency of the turbine

outlet pressure was 5.75 kHz, indicating that the turbine removed some of the unsteadiness of the flow. The raw data and a zoomed in view showing the oscillations in the pressure measurement data is shown in Figure 60.

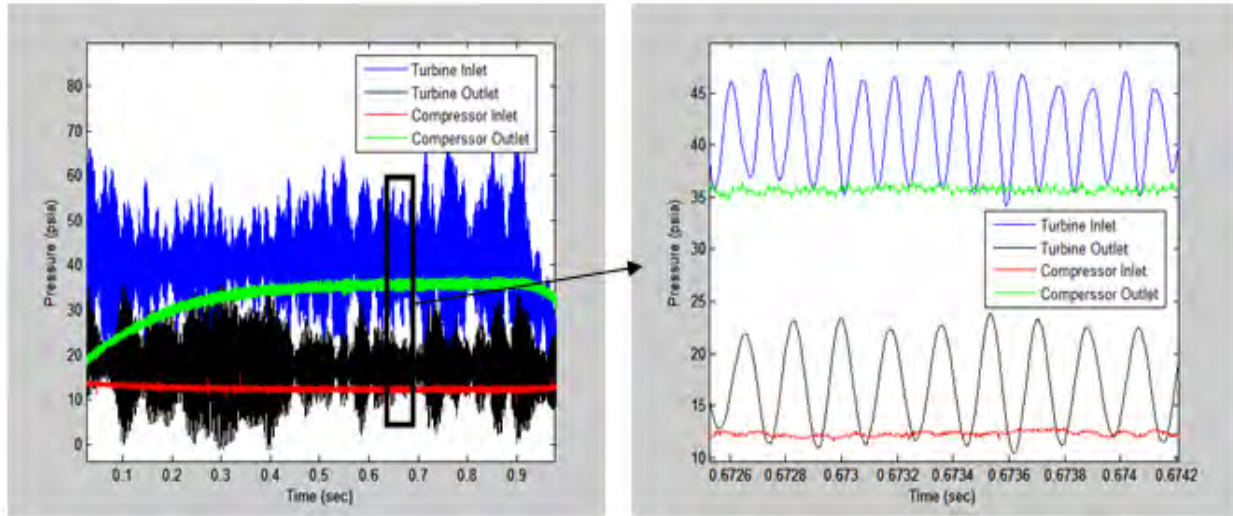


Figure 60. Compressor and turbine inlet and outlet pressures for a RDE-turbine run at $\dot{m}=39.8$ lbm/min and $\phi=1.38$

Oscillations in the pressure data were also seen in the pressure data from the detonation channel in Figure 46 as well as the nozzle base and throat pressure data in Figure 56. However, the amplitude of the oscillations for the turbine pressure data was much greater than the variation of both the detonation channel and nozzle pressure data. The fluctuations and large amplitudes seen in the turbine pressure data occurred due to either electrical noise or the interaction of the flow with the turbine or plenum chamber.

A 150 point moving average of the turbine pressures was taken to eliminate some of the transients of the data to determine an average pressure value at the inlet and outlet for a given run. The pressure data for the turbine and compressor for the averaged data is shown in Figure 61.

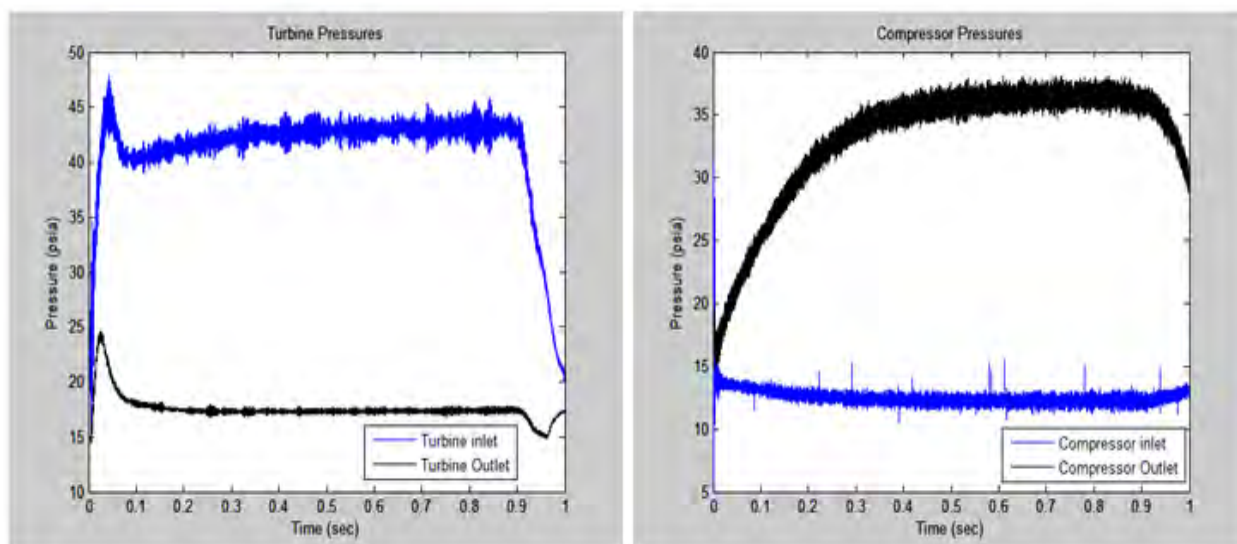


Figure 61. Turbine pressures using a 150 point moving average and compressor pressure measurements for turbine-RDE testing at $\dot{m}=39.8$ lbm/min and $\phi=1.38$

A pressure spike occurred in the turbine at the beginning of testing due to the air and fuel establishing times of the RDE. The fuel establishing time was minimized during nozzle testing, but the value could not be lowered below 90 ms, so the plenum was partially filled with combustible reactants when the pre-detonator fired for the first time. The extra reactants in the plenum combusted upon ignition of the pre-detonator, and this caused the pressure spike in the turbine pressure data. After the initial pressure spike, the average pressures for both the compressor and the turbine reach a quasi-steady state value near the end of the one second run.

The steady state values at the end of the runs were considered the average pressure for each run. The average turbine inlet and outlet pressures are shown in Figure 62. The turbine inlet pressure increases linearly with increasing RDE mass flow rate, with a peak pressure of 45 psia. The JetCat P-200 has a compressor pressure ratio of 4 at maximum RPM, which equates to a turbine inlet pressure of 56.8 psia for the test conditions. The RDE never achieves a pressure of 56.8 psia, but the turbine still achieved maximum RPM for most of the runs.

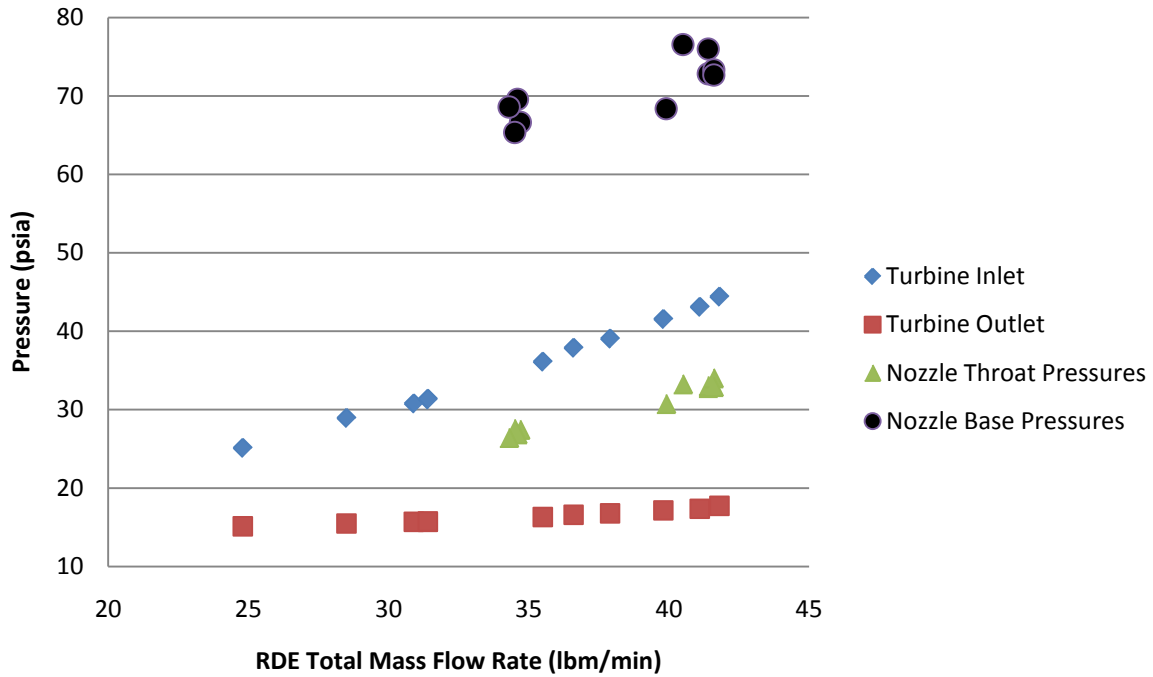


Figure 62. Turbine inlet and outlet pressure comparison with 1.17 in. nozzle pressure data

The turbine inlet pressures coincide with the nozzle throat pressure data more than the nozzle base pressure because the turbine inlet pressure measurement was taken one inch from the turbine stator vanes. The turbine outlet pressure varied little with the mass flow rate as compared to the turbine inlet pressure, but this occurs because the pressure difference correlates to more work being accomplished by the compressor, because the compressor mass flow rate and pressure ratio were dependant on the turbine inlet pressure, and thus the mass flow rate, as shown in Figure 63.

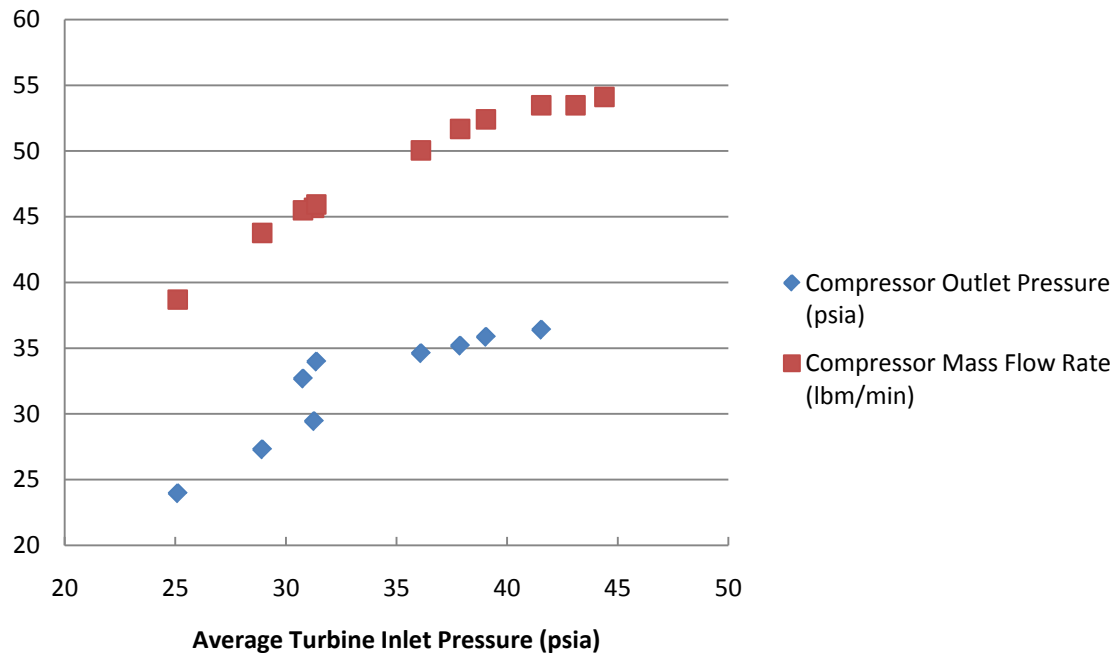


Figure 63. Compressor performance relation to turbine inlet pressure produced by RDE

The compressor outlet pressure is indicative of the compressor pressure ratio because the compressor inlet pressure remains constant at the ambient conditions of the test cell.

The compressor behaved steadily as compared to the turbine and RPM data, with a linear relationship of the compressor pressure ratio with respect to both the RDE total mass flow rate and compressor mass flow rate as seen in Figure 64. As is expected, the trend is much more pronounced for the compressor mass flow rate, with a direct correlation between the compressor mass flow rate and the compressor pressure ratio, showing that the compressor performs normally despite the unsteadiness of the RPM and turbine data.

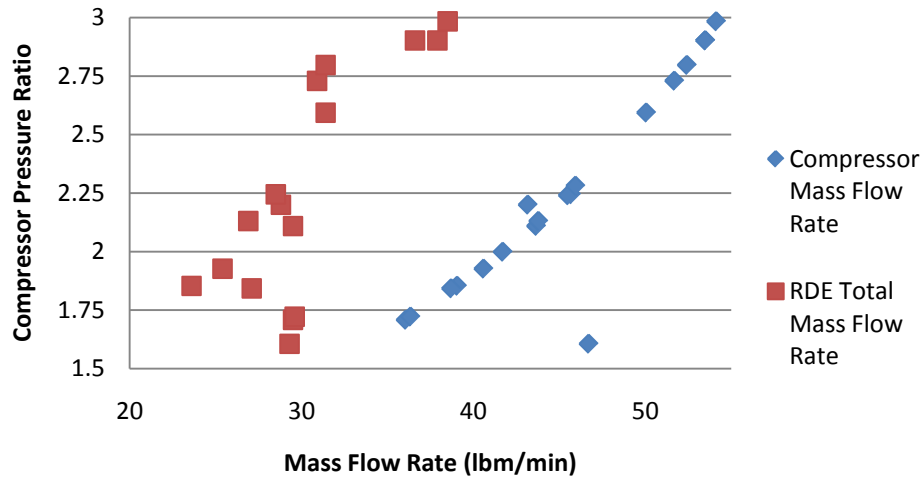


Figure 64. Compressor pressure ratio dependence on RDE and compressor mass flow rate

E. Engine RPM

The RPM data showed fluctuations due to the unsteadiness of the RDE exit flow, and because of this a moving average was taken of the RPM data to determine an average RPM for each test. A comparison of the raw RPM data with the moving average is shown in Figure 65.

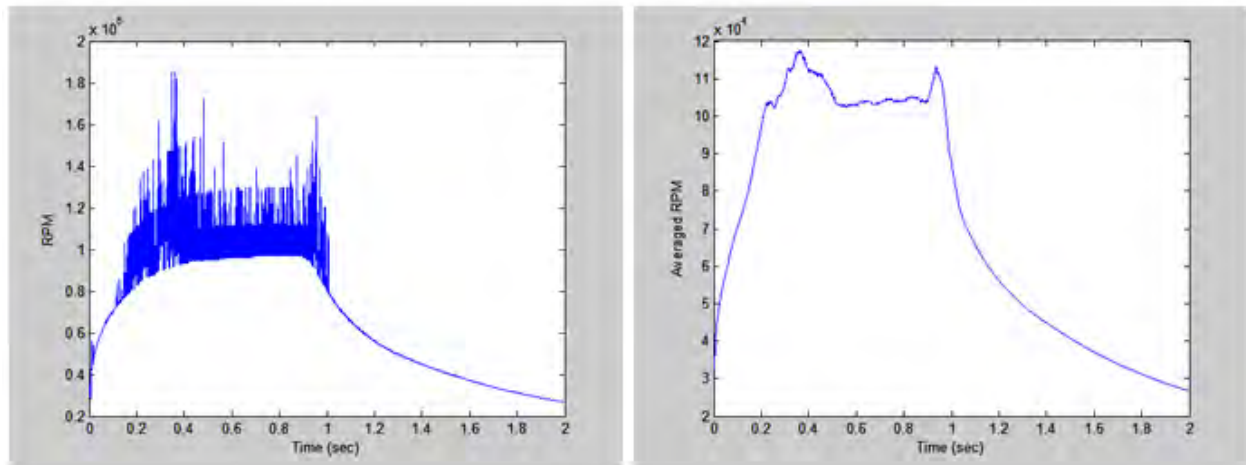


Figure 65. Comparison of unprocessed RPM data with RPM data using a 150 point moving average at $\dot{m}=39.8$ lbm/min and $\phi=1.38$

The average RPM for the run was calculated from the steady state RPM occurring near the end of the 1 second run. Although the RPM varied substantially over the run, the average

RPM stayed consistent after the initial transients. The compressor outlet pressure shown in Figure 61 has little variation once leveling off even though the RPM oscillates over the course of the run. Compressor performance also relies on the turbine inlet pressure, which oscillates along with the RPM. The compressor response, then, must primarily be dependent on the average RPM and average turbine inlet pressure because the compressor cannot respond quickly enough to the fast fluctuations of the turbine pressure and RPM.

F. Catastrophic Failure

The turbine ran seven full successful detonations with enriched air before experiencing a catastrophic failure. Each successful run was 1 second in length. The catastrophic failure occurred on the first test attempt for a 2 second run with enriched air, and the turbine experienced a catastrophic failure at 1.2 seconds into the run. The engine failure occurred for a RDE mass flow rate of 41.8 lbm/min and an equivalence ratio of 1.31. The previous run before failure had a mass flow rate of 41.3 lbm/min and an equivalence ratio of 1.34. In the failure, the shaft connecting the compressor and turbine broke at the turbine wheel and all 29 blades of the turbine sheared from the turbine wheel. The turbine wheel cut through the nozzle aft of the welded interface between the nozzle and the turbine casing, causing the turbine wheel to exit the turbine casing and leaving the turbine stator vanes exposed. Figure 66 shows the comparison of the turbine before and after the catastrophic failure.



Before Failure



After Failure

Figure 66. Comparison of the JetCat turbine before and after the catastrophic failure

The RPM data for the failure is shown in Figure 67.

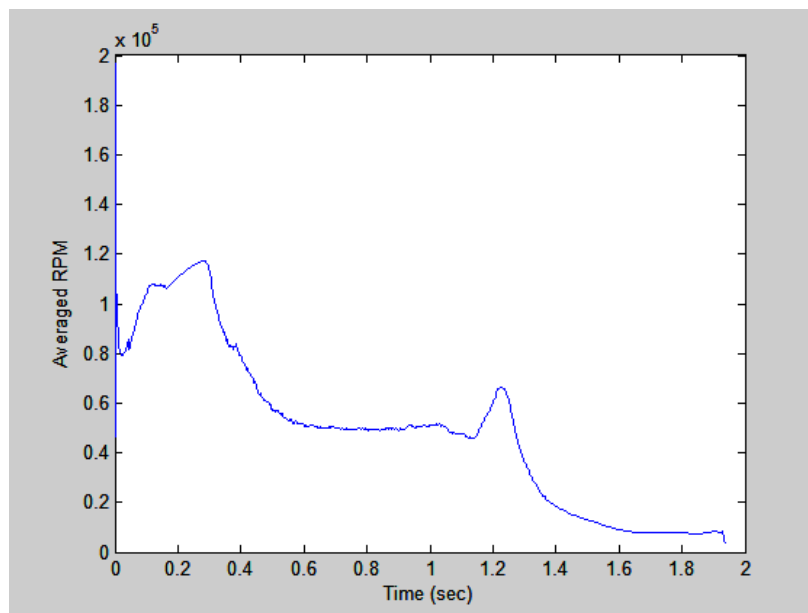


Figure 67. RPM 150 point moving average for catastrophic failure at $\dot{m}=41.8$ lbm/min and $\phi=1.31$

The RPM drops rapidly around 0.4 seconds, indicating that either the shaft bearings began to fail or the turbine blades began to contact the turbine casing due to thermal creep of the blades or instability in the shaft. The failure occurs at 1.2 seconds into the run, and is shown as

an increase in RPM because the RPM reading was taken from the compressor, which was free spinning upon the shaft shearing at the turbine. All other data from the catastrophic failure can be found in Appendix D. All data undergoes a substantial deviation at 1.2 seconds when the failure occurs.

V. Conclusions

The first ever RDE-axial turbine testing was performed in order to determine the feasibility and desirability of incorporating RDEs with conventional gas-turbine engine cycles. Prior to the turbine tests, nozzle testing was accomplished to determine the effects of back-pressurization on the RDE. Overall, this research served as a starting point for an exploration into the use of RDEs with the conventional gas-turbine engine cycle that may produce the next revolutionary leap in engine development.

Nozzle testing showed that, for both enriched and standard air, the addition of a nozzle increased the operational space of the RDE (for a given mass flow rate, a lower equivalence ratio could be achieved, or conversely, a lower mass flow rate was attainable for the same equivalence ratio) leading to the conclusion that back-pressurization enhances RDE operability. This conclusion is beneficial for gas-turbine integration, because placing objects behind the RDE will actually aid, not hinder, RDE operation. Occurrence of successful detonations showed a dependence on both the total mass flow rate and the equivalence ratio of the run, but the average wave speeds trended only with the equivalence ratio for the nozzle testing. Because a 100% increase in equivalence ratio leads to only a 10% increase in detonation velocity, RDEs should be operated at as low an equivalence ratio as is allowed for a given mass flow rate to minimize fuel burn. The detonation channel pressure increased linearly with increasing mass flow rate, potentially leading to the ability to throttle an RDE by changing the mass flow rate of the RDE as long as the operation remained in the detonable limits. The nozzle acts as an expander, accelerating the flow from a subsonic velocity at the RDE exit plane to a sonic velocity at the converged nozzle throat. Because the exit of the RDE is subsonic, all RDE exhaust will be

required to accelerate to a sonic velocity at the turbine stator vanes similarly to typical jet engine combustors today.

Turbine testing resulted in the first successful operation of a turbine by a RDE. The operability of the RDE with the turbine lined up well with the operability of the RDE with the nozzles, revealing that nozzles sized to match the choked conditions of the turbine can effectively simulate the impact of the turbine on RDE operation. Turbine pressure data and RPM data showed unsteadiness in the RDE exhaust, but this unsteadiness did not correlate to unsteadiness in the compressor since the compressor pressures and mass flow achieved near steady state values after a run time of only 1 second. The operation of the turbine with the RDE produced JetCat RPMs at or near the maximum RPM for most runs tested and achieved a maximum compressor mass flow rate and compressor pressure ratio during RDE-turbine testing of 53 lbm/min and 3, respectively. The JetCat P-200 maximum mass flow rate and compressor pressure ratio are 60 lbm/min and 4, respectively. The JetCat P-200 operated by the RDE performed below the JetCat published values, but still achieved similar values. Although more testing, especially looking at power and efficiency, are required, a preliminary conclusion can be drawn that the JetCat driven by the RDE performs as well or negligibly worse than the JetCat under normal operation. The turbine testing ended with a catastrophic failure of the turbine where the shaft ruptured near the turbine wheel and all of the turbine blades sheared from the turbine wheel. The failure occurred either due to over-spinning of the turbomachinery, since many of the runs had RPMs over 112,000, or due to thermal creep of the turbine blades that caused rubbing on the turbine casing until the turbine blades split from the turbine wheel. Although efforts were made to reduce the impact of the high turbine inlet temperature due to the use of hydrogen and air as propellants, the high turbine inlet temperature ultimately led to the

failure of the JetCat turbine. Failure potential may be reduced by using a mixture of bypass and RDE exhaust instead of full admission, or ensuring that the RDE exhaust will give a corrected mass flow rate closer to the corrected mass flow rate of the turbine. In spite of the catastrophic failure, the initial results of the turbine-RDE testing revealed that driving a turbine via RDE exhaust was possible, and produced results similar to that of the turbine run using deflagration.

Future Work

1. Turbine-RDE testing showed the feasibility of a turbine driven by a RDE, but future work should focus on survivability and operability of the turbine when run using RDE exhaust. Several research areas are extremely important in pursuit of these objectives. First, discovering a thermal management system for the RDE is paramount in developing the operability of the RDE with turbomachinery. Testing conducted with the turbine was limited to two second runs due to the high thermal loads of the RDE. Developing a better understanding of the RDE exhaust temperatures is critical in aiding integration with turbines, as this will determine the turbine inlet temperature and the turbine corrected mass flow rate, when also knowing the exit pressure. Improving the thermal management will also allow for longer run times, allowing for data to be taken that is not affected by the startup transients of the engine.

2. For future turbine testing, it may be beneficial to combine the RDE exhaust with bypass air to bring the peak temperatures and pressures down. Accomplishing this would be beneficial for gas-turbines as higher bypass ratios increase propulsive efficiency, so by utilizing bypass flow, the efficiency of the gas-turbine cycle increases.

3. Throttling the RDE will be important for future integration with gas-turbine engine cycles. Testing should be conducted on the effects of throttling in the RDE engine, focusing on RDE performance, such as the detonation wave speed of the RDE. Once detonations are

achieved, it would be of interest to determine whether operating conditions that cannot initiate a detonation could sustain a detonation when the RDE was throttled from a known operating condition that produces successful detonations. If the RDE could be throttled, a much better understanding of turbine operability when run using a RDE would be possible.

4. Although nozzle testing was performed primarily to understand the effects of the turbine on RDE operability for this research, there are many avenues for future work that can be performed using nozzles in conjunction with RDEs. Objects placed behind the 3 in. RDE, such as a nozzle or turbine, created a back-pressurization of the RDE that increased the RDE range of operability. This conclusion should be validated by using nozzles on other types of RDEs operating under different mass flow rates to ensure that this conclusion applies to all RDEs at all operations as opposed to the single RDE used for performing all testing for this research. Testing should also be accomplished using converging-diverging nozzles on the RDE, since the shock diamonds from all nozzle testing clearly indicate high pressures that could be expanded in a diverging nozzle to increase the thrust output of the RDE. Finally, for the test article used for this research, the only way to duct the RDE exhaust without completely dismantling and constructing the JetCat engine from scratch was to duct the flow from the RDE to the turbine. Future testing would produce more valuable results if the RDE exhaust could be directly exhausted into the turbine.

Appendix A. Sensitivity Analysis

1. Linear Sensitivity

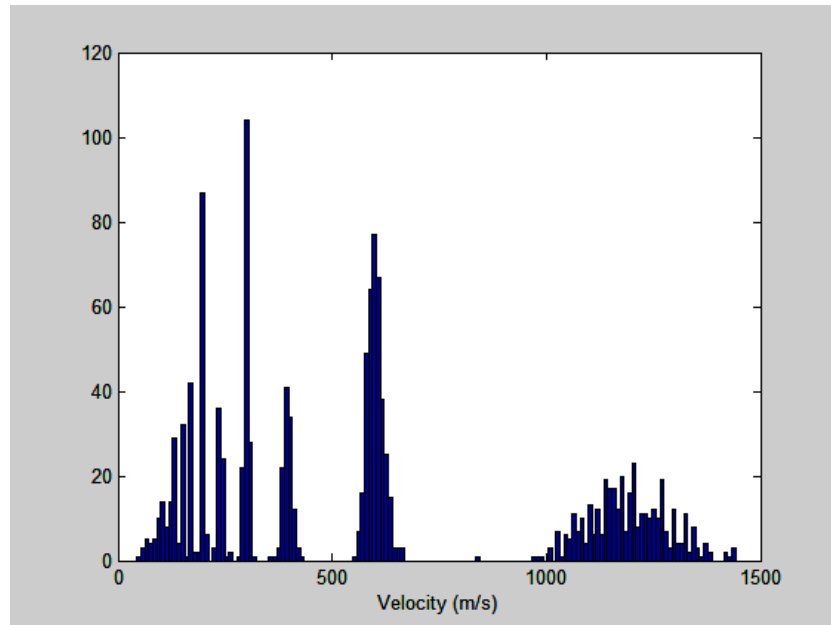


Figure 68. Velocity Histogram for PCB data for data reduction using 2 linear equations to normalize data

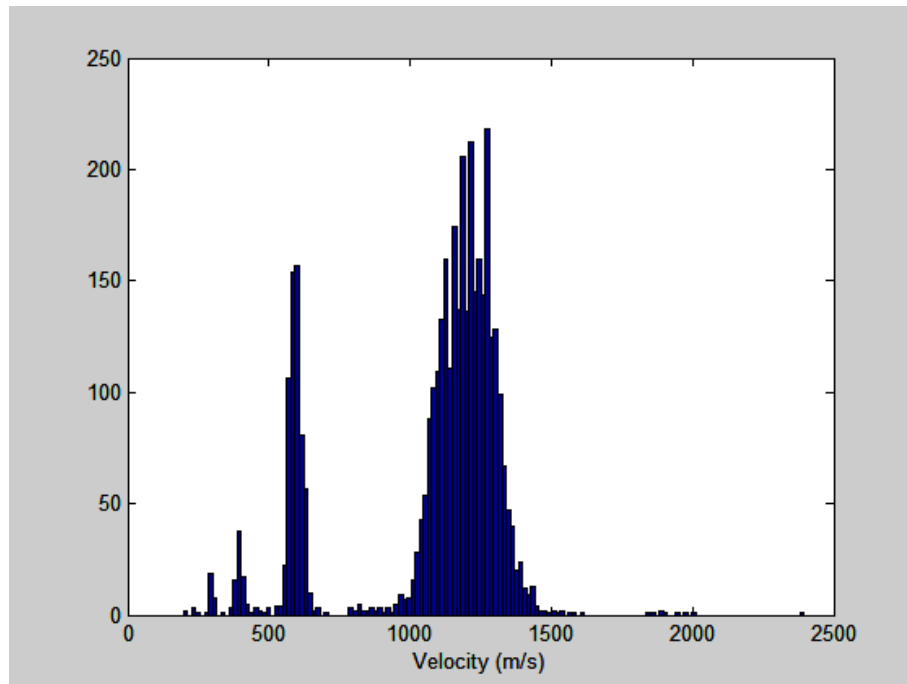


Figure 69. Velocity Histogram for PCB data for data reduction using 10 linear equations to normalize data

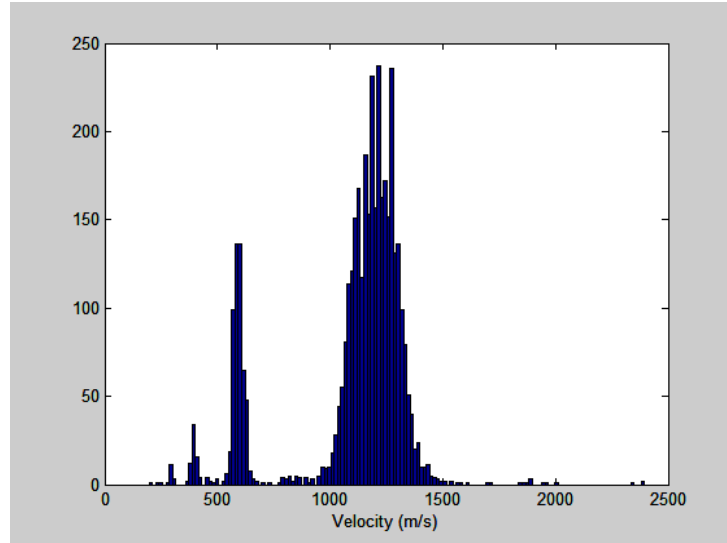


Figure 70. Velocity Histogram for PCB data for data reduction using 100 linear equations to normalize data2 Line Data Reduction of PCB data

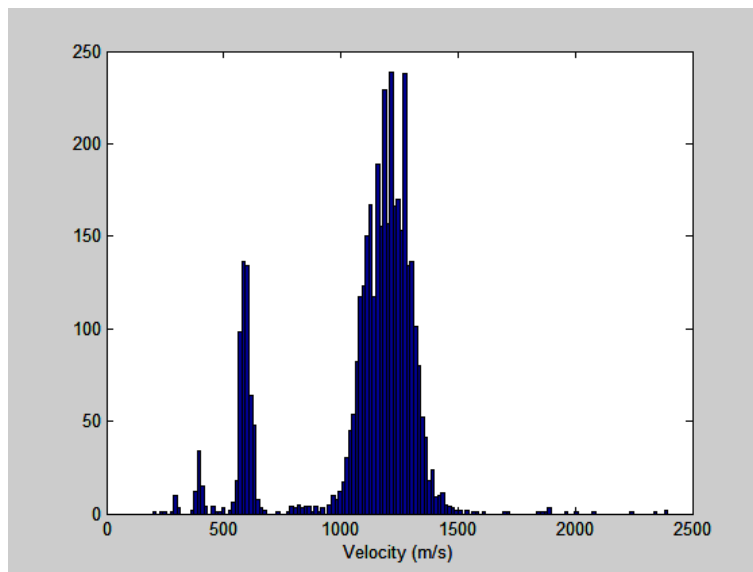


Figure 71. Velocity Histogram for PCB data for data reduction using 200 linear equations to normalize data2 Line Data Reduction of PCB data

As the number of linear equations used to normalize the PCB data increases from Figure 68 to Figure 71, the variations in the average wave speed decreases as well as the number of velocities measured in the 600 m/s band. However, as the number of linear equations increases from 100 to 200, there is practically no change in the histograms.

Table 5. PCB data linear normalization sensitivity analysis for MATLAB time of flight code

# Linear Equations	Average Speed (m/s)	Average Combustion Speed (m/s)	Average Detonation Speed (m/s)	Mode Detonation Speed (m/s)	Speed Ratio	% error
2	605.9	383.84	1194.7	1240.4	0.3213	131.77
10	1078.6	581.91	1208.1	1240.4	0.4817	50.97
100	1101.5	594.56	1208.8	1240.4	0.4918	46.71
200	1103.4	596.29	1209.1	1240.4	0.4932	46.45
2-200 % difference	45.09%	35.63%	1.19%	0.00%	34.85%	
10-200 % difference	2.25%	2.41%	0.08%	0.00%	2.33%	

Table 6. Kulite data linear normalization sensitivity analysis for MATLAB time of flight code

# Linear Equations	Average Speed (m/s)	Average Combustion Speed (m/s)	Average Detonation Speed (m/s)	Mode Detonation Speed (m/s)	Speed Ratio	% error
1	1196.3	803.7868	1204.8	1215.2	0.6672	18.51
10	1198.1	816.0246	1206.5	1215.2	0.6763	19.33
100	1198.1	815.9662	1206.5	1215.2	0.6763	19.33
1-100 % error	0.15%	1.49%	0.14%	0.00%	1.35%	

The number of linear equations used makes a large difference in the wave speed calculations. The number of linear equations sensitivity analysis was performed before changing the PAT value of the PCB data from 4 to 2, which is why the histograms still have the 600 m/s band and the percent error of the PCB data is so high (almost 50%) after applying the correct number of linear equations to normalize the data.

2. Sensitivity Analysis Data

Table 7. PCB Sensitivity Analysis Data

Standard Deviation	Time Hold (μs)	Points Above Threshold	Average Wave Speed (m/s)
0	80	2	2421.20
0	80	3	2119.80
0	80	4	1978.20
0	80	5	1884.20
0	100	2	1961.90
0	100	3	1756.10
0	100	4	1674.90
0	100	5	1606.10
0	120	2	1587.30
0	120	3	1361.20
0	120	4	1308.90
0	120	5	1281.30
1	80	2	1283.10
1	80	3	1208.50
1	80	4	1151.90
1	80	5	1061.90
1	100	2	1246.20
1	100	3	1205.40
1	100	4	1150.60
1	100	5	1061.90
1	120	2	1236.20
1	120	3	1203.60
1	120	4	1149.30
1	120	5	1059.70
2	80	2	1051.70
2	80	3	801.78
2	80	4	578.65
2	80	5	467.97
2	100	2	1050.30
2	100	3	801.78
2	100	4	578.65
2	100	5	467.97
2	120	2	1050.30
2	120	3	801.78
2	120	4	578.65
2	120	5	467.97

Table 8. Kulite Sensitivity Analysis Data

Standard Deviation	Time Hold (μ s)	Points Above Threshold	Average Wave Speed (m/s)
0	100	2	2132.4
0	100	3	2115.9
0	100	4	2098
0	100	5	2075
0	120	2	1653.4
0	120	3	1637.7
0	120	4	1614
0	120	5	1589
0	140	2	1361.2
0	140	3	1350.3
0	140	4	1334
0	140	5	1316
1	100	2	1305.9
1	100	3	1290.4
1	100	4	1276.7
1	100	5	1262.5
1	120	2	1200.4
1	120	3	1198.8
1	120	4	1198.1
1	120	5	1197.1
1	140	2	1193.7
1	140	3	1192.9
1	140	4	1192.9
1	140	5	1192.6
2	100	2	1141
2	100	3	1134.2
2	100	4	1122.1
2	100	5	1106.2
2	120	2	1137.5
2	120	3	1130.7
2	120	4	1120.1
2	120	5	1104.9
2	140	2	1135.9
2	140	3	1129.6
2	140	4	1119.6
2	140	5	1104.6

3. Kulite and PCB Data Comparison

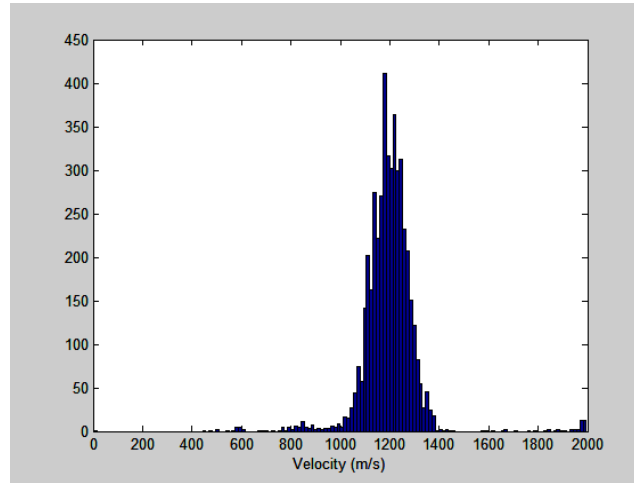


Figure 72. Velocity histogram for Kulite data for a $\dot{m}=48.3$ lbm/min and $\phi=0.87$ for a threshold of 1 standard deviation, a time hold of 120 μ s, and a PAT of 4

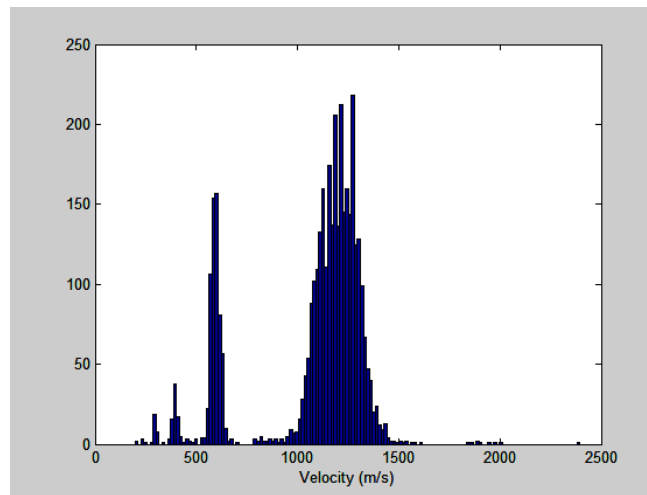


Figure 73. Velocity histogram for PCB data for a $\dot{m}=48.3$ lbm/min and $\phi=0.87$ for a threshold of 1 standard deviation, a time hold of 100 μ s, and a PAT of 4

The Kulite histogram (Figure 73) only has one primary band of values, whereas the PCB data (Figure 72) has two bands, one around 600 m/s and the other around 1200 m/s. As discussed previously, this was a result of aliasing in the data reduction coding and was corrected by reducing the PAT value for the PCB data to 2. The difference between the Kulite and PCB data is what motivated the in depth analysis of the data reduction methods.

Table 9. Percent Difference between the Kulite and the PCB values of wave speed for a points above threshold value of 4 for the PCB

Total Mass Flow Rate (lbm/min)	Equivalence Ratio	Average Speed	Average Combustion Speed	Average Detonation Speed
46.4	1.02	5.24%	18.39%	-0.54%
46.4	1.08	5.90%	27.16%	-0.46%
46.1	1.07	8.15%	29.48%	-0.38%
46	1.07	9.29%	16.58%	-0.43%
45.6	0.83	6.65%	8.56%	-0.53%
45.4	0.74	5.27%	6.82%	-0.37%
46.6	1.12	4.76%	31.05%	-0.33%
48.5	1.02	8.35%	31.14%	-0.41%
48.2	0.94	6.38%	23.82%	0.27%
48.3	0.87	10.91%	38.13%	-0.27%
48.4	0.8	14.91%	31.55%	-0.28%
47.9	0.77	16.84%	27.53%	-0.23%
48.2	0.74	15.62%	20.88%	-0.55%
Average		9.10%	23.93%	-0.35%
Standard Deviation		4.21%	9.31%	0.21%
Note: Positive %- Kulite Larger; Negative %- PCB larger				

The Kulite data had a higher average speed for every run compared. The PCB data had a secondary velocity band around 600 m/s while the Kulite did not, and this drove the average velocities of the run below the Kulite data. The combustion speed varied more widely in the magnitude of the percent difference, but once again the Kulite data had larger values for all runs. The average detonation velocities were nearly the same for both the PCB and the Kulite data, but the PCB data had a larger average for all runs. From analyzing the data, it was discovered that the PCB would read some extremely high velocities around the 2,500 m/s range whereas the Kulite would not, which accounts for the PCB data having a higher average detonation velocity than the Kulite data.

Table 10. Percent Difference between the Kulite and the PCB values of wave speed for a points above threshold value of 2 for the PCB

Total Mass Flow Rate (lbm/min)	Equivalence Ratio	Average Speed	Average Combustion Speed	Average Detonation Speed
46.4	1.02	-1.14%	-1.15%	-1.59%
46.4	1.08	0.05%	14.79%	-0.54%
46.1	1.07	-0.36%	7.94%	-1.06%
46	1.07	-1.33%	2.11%	-1.81%
45.6	0.83	-0.55%	-15.15%	-0.72%
45.4	0.74	-2.05%	-15.37%	-0.95%
46.6	1.12	-0.22%	8.57%	-0.66%
48.5	1.02	-1.12%	8.35%	-1.69%
48.2	0.94	-0.01%	-0.15%	-0.10%
48.3	0.87	-0.83%	8.99%	-1.30%
48.4	0.8	-0.63%	1.24%	-1.24%
47.9	0.77	-0.50%	-6.83%	-0.91%
48.2	0.74	-2.16%	-12.88%	-1.71%
Average		-0.83%	0.03%	-1.10%
Standard Deviation		0.70%	9.96%	0.52%
Note: Positive %- Kulite Larger; Negative %- PCB larger				

The average speed and standard deviation values were greatly reduced with the change of the PAT value from 4 to 2 for the PCB wave speed data reduction. The average combustion speed % difference average was lower than the original data with the standard deviation remaining similar to the original value, so the average combustion speeds also grew closer with a PCB PAT value of 2. Both the average percent difference and the standard deviation for the average detonation speed increased, but the increase was negligible when compared to the higher level of agreement of the average speed and average combustion speed between the Kulite and PCB data for the PCB PAT value of 2. Overall, the PCB data was much more consistent in producing quality data because it was more resistant to thermal changes, whereas the Kulite

pressure sensor, when heated too high, would either produce erroneous results or completely break.

4. Turbine Data PCB sensitivity

Because the scan rate had to be reduced, the data reduction techniques used for the nozzle testing had to be modified for turbine testing. This was accomplished by recognizing a pressure spike with two consecutive points placed one standard deviation above the average or a single point located two standard deviations above the average. The histograms below show the results of the changes. The combination of the two data reduction techniques produces similar percent errors and average wave speeds as the data taken at a scan rate of 1MHz for 1 second.

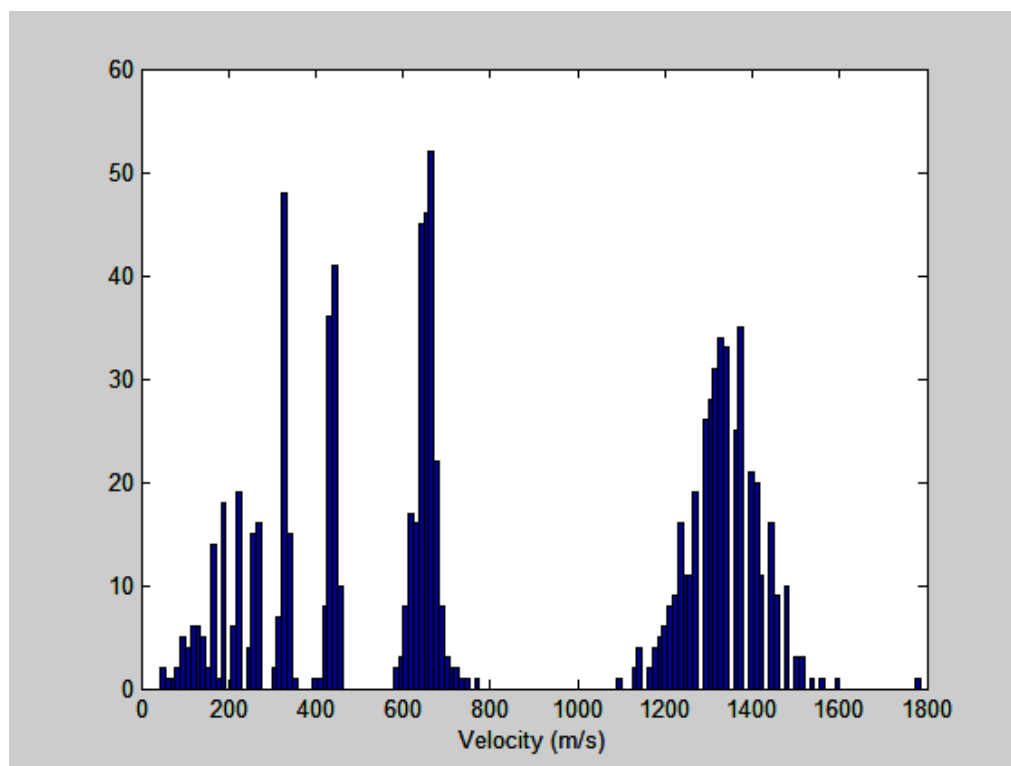


Figure 74. Average wave speed histogram for a threshold of 1 standard deviation, a points above threshold of 2, and a hold time of 120 μ s

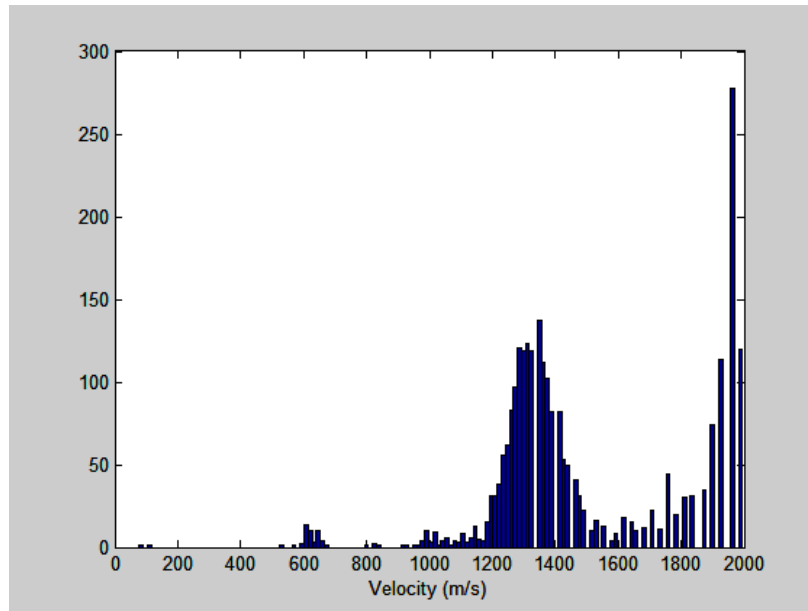


Figure 75. Average wave speed histogram for a threshold of 1 standard deviation, a points above threshold of 1, and a hold time of 120 μ s

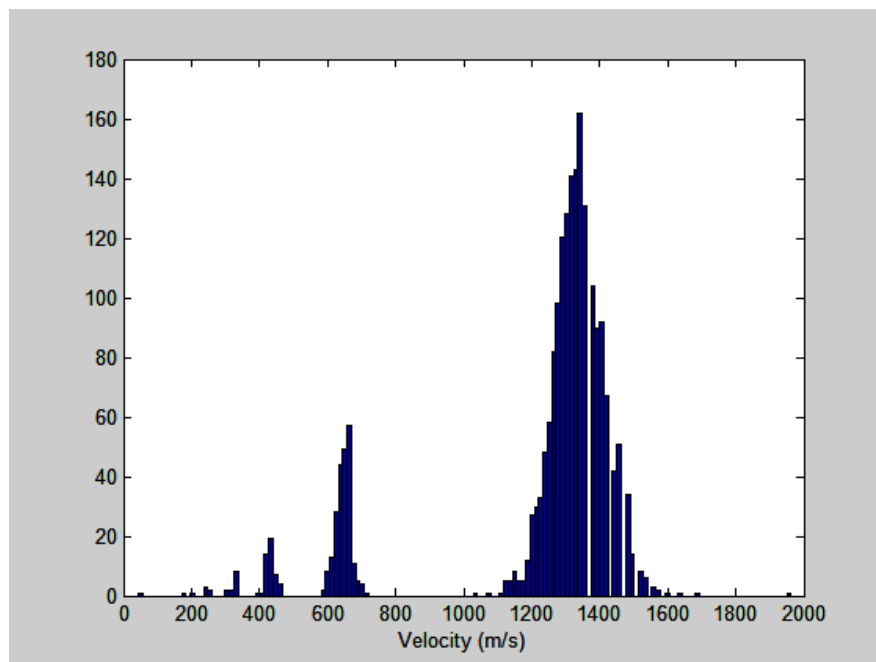


Figure 76. Average wave speed histogram for a points above the threshold value of 2 for a threshold of 1 standard deviation and a points above threshold of 1 for a threshold of 2 standard deviations, both using a hold time of 120 μ s

Appendix B. Uncertainty

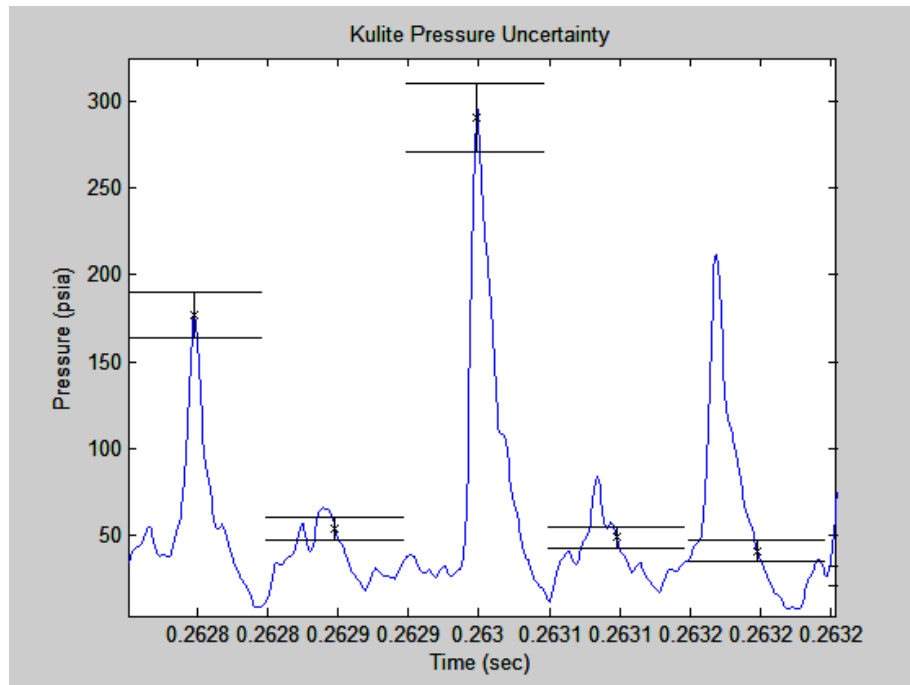


Figure 77. Kulite pressure total sample uncertainty represented via error bars

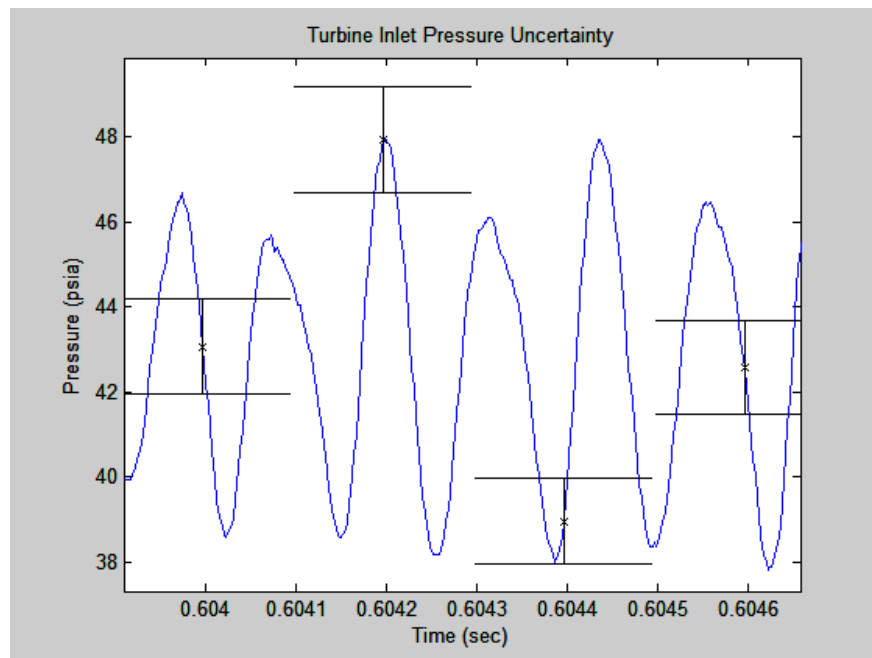


Figure 78. Turbine inlet total sample uncertainty represented via error bars

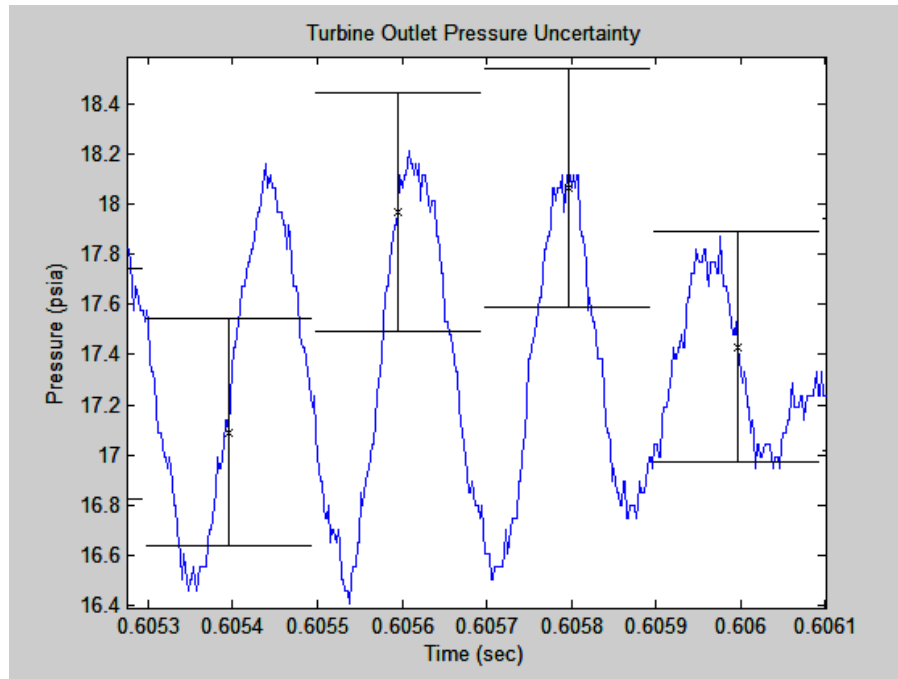


Figure 79. Turbine outlet pressure total sample uncertainty represented via error bars

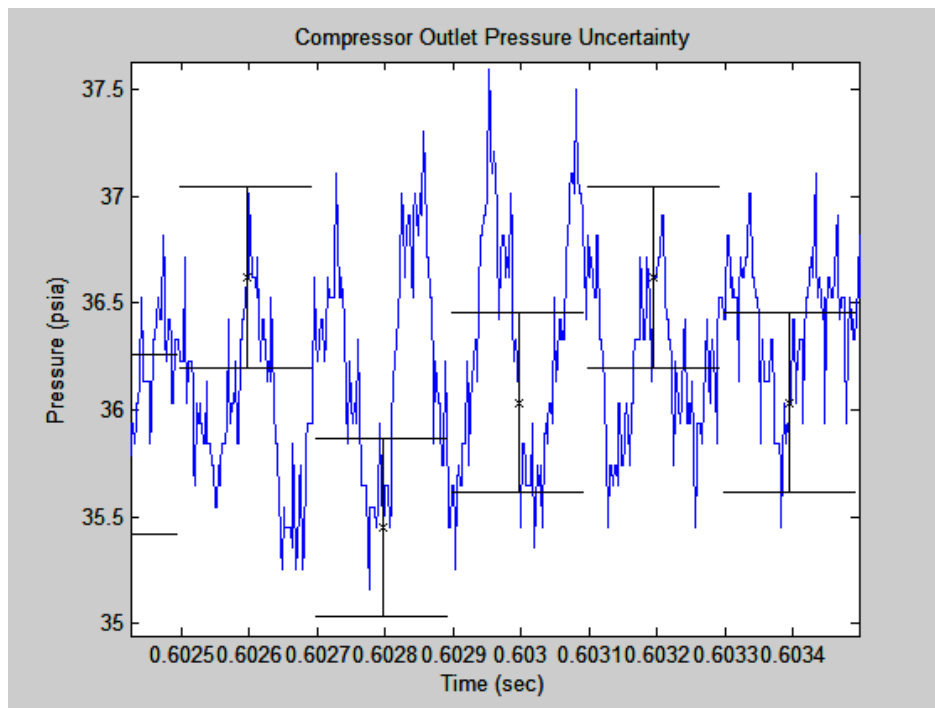


Figure 80. Compressor outlet total sample pressure uncertainty represented via error bars

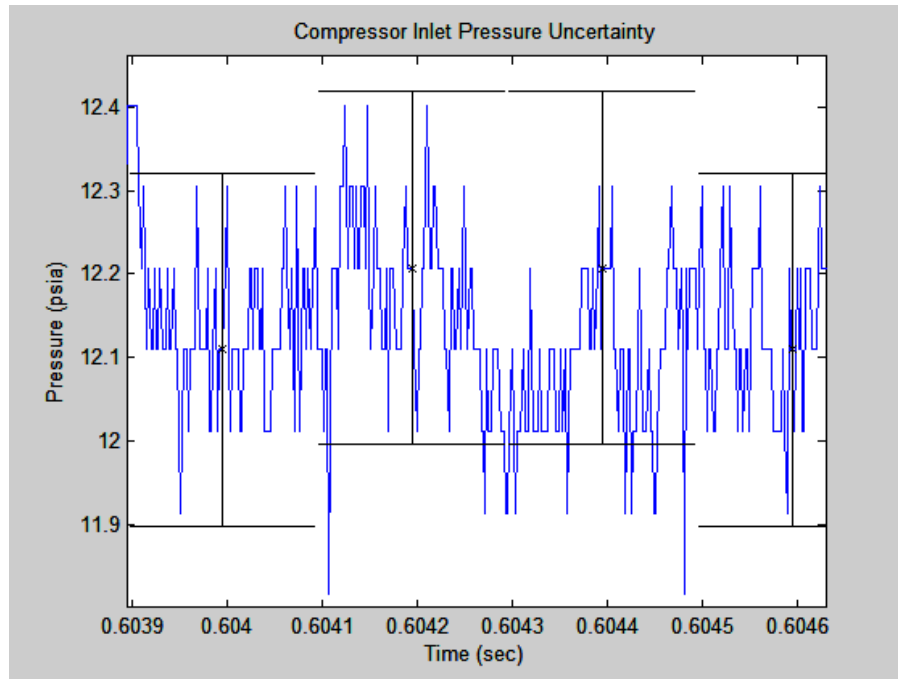


Figure 81. Compressor inlet pressure uncertainty represented via error bars

Table 11. 1.5 in. nozzle Kulite average wave speed error

Total Mass Flow Rate (lbm/min)	Equivalence Ratio	Average Wave Speed (m/s)	Percent Error
42.70	1.35	1306.30	16.90
44.80	1.26	1289.70	20.11
44.60	1.22	1266.00	17.02
46.40	1.02	1200.90	22.06
46.40	1.08	1250.40	19.61
46.10	1.07	1238.70	19.06
46.00	1.07	1226.90	17.13
45.60	0.83	1190.70	29.46
45.40	0.74	1157.70	34.05
46.60	1.12	1253.60	20.72
48.50	1.02	1223.70	19.82
48.20	0.94	1225.70	30.56
48.30	0.87	1200.40	20.62
48.40	0.80	1184.10	22.19
47.90	0.77	1175.50	31.94
48.20	0.74	1153.70	37.81

Table 12. Nozzle PCB data average wave speed error

Total Mass Flow Rate (lbm/min)	Equivalence Ratio	Average Wave Speed (m/s)	Percent Error
46.40	1.02	1212.50	31.87
46.40	1.08	1247.80	24.76
46.10	1.07	1242.00	27.19
46.00	1.07	1242.20	31.75
45.60	0.83	1189.50	29.33
45.40	0.74	1172.20	31.82
46.40	1.16	1260.40	22.96
46.00	1.13	1256.90	25.89
46.60	1.12	1254.30	25.19
48.50	1.02	1234.20	30.74
48.30	0.97	1222.30	22.70
48.20	0.94	1215.80	24.56
48.30	0.91	1208.10	23.41
48.40	0.88	1201.00	24.94
48.30	0.87	1206.30	29.73
48.40	0.80	1188.30	30.25
47.90	0.77	1172.90	32.13
48.20	0.74	1169.20	37.45
48.30	0.67	1141.80	39.43
48.30	0.63	1149.10	49.32
47.80	0.60	1137.80	53.05
37.30	1.02	1201.40	31.50
37.30	1.16	1170.30	45.94
37.60	1.35	1101.00	56.70
37.80	1.36	1101.00	56.70
42.00	0.91	1183.70	23.75
41.40	0.93	1178.60	22.48
41.90	0.92	1182.10	27.29
41.90	1.22	1220.90	27.91
44.80	1.14	1160.00	44.34
38.40	1.31	1158.90	33.49
47.10	1.25	1210.20	36.84
46.70	1.16	1211.20	50.09
47.20	1.51	1232.00	23.98
47.80	1.52	1205.00	29.03
41.80	1.46	1125.00	52.30
40.90	0.78	1037.20	62.37

Table 13. Turbine PCB data error and scan rate

Total Mass Flow Rate (lbm/min)	Equivalence Ratio	Average Wave Speed (m/s)	Percent Error	Scan Rate (kHz)
1.13	28.80	1011.10	77.40	250
1.11	29.30	1043.00	74.22	250
1.11	29.50	1033.70	76.85	250
1.28	29.50	1026.70	81.71	250
1.28	29.60	1068.80	72.65	250
1.29	29.30	1064.50	69.48	250
1.51	23.60	910.21	94.97	250
1.37	23.80	934.30	89.51	250
1.28	25.40	1062.50	79.92	250
1.22	26.80	995.64	86.17	250
1.36	27.10	1004.00	87.07	250
1.37	26.90	941.81	97.37	250
1.46	26.80	1520.80	45.92	250
1.70	24.80	940.92	88.34	250
1.47	28.50	965.40	84.99	250
0.94	31.40	959.12	73.18	250
1.13	30.90	1041.90	67.56	250
1.30	31.40	1026.40	77.50	250
1.15	35.50	1042.60	70.86	250
1.33	36.60	1102.10	74.53	250
1.28	37.90	1097.30	70.84	250
1.38	39.80	1227.70	44.38	500
1.34	41.10	1238.90	36.61	500
1.31	41.80	1156.40	62.49	500

For all uncertainty data, the lower the average wave speed, the higher the error of the run. Higher error occurs for lower average wave speeds because these runs often have a mixture of detonation wave speeds and non-detonation wave speeds, leading to higher variability than with successful detonation runs. For the turbine data, the lowest errors occurred for successful detonations with the highest scan rate.

Appendix C. Shock Diamond Analysis

A shock diamond analysis of the nozzled RDE exhaust estimated the total pressure at the exit of the nozzle. Determining the total pressure at the nozzle exit provided information on the total pressure that will be present at the turbine inlet, which helped determine whether the RDE could provide the pressures needed to drive the JetCat turbine. The high speed camera data was taken from an RDE run with a mass flow rate of 41.9 lbm/min, and a ϕ of 1.22. This mass flow rate was chosen because it lies comfortably in the operational space for the RDE with the 1.5 in. convergent nozzle (see Figure 42). The camera was set to a 500 μ s exposure. The static pressure was determined by measuring the angles and dimensions of the shock diamonds and exhaust plume. The exhaust plume contains a series of Prandtl-Meyer expansions and oblique shocks as shown in Figure 82, which shows the structure of an underexpanded flow exiting from a nozzle.

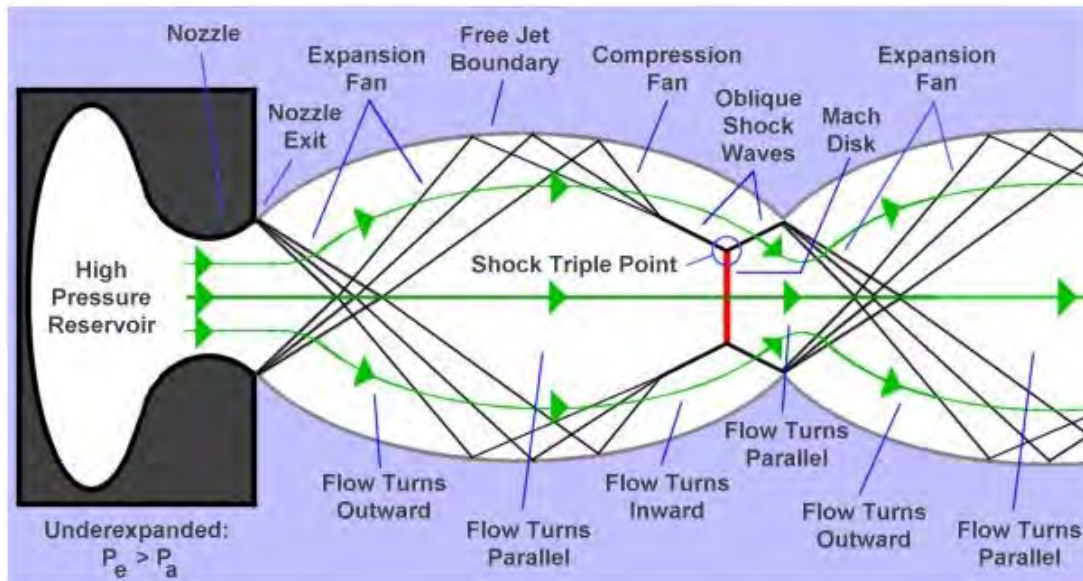


Figure 82. Wave structures and shock diamonds in an underexpanded flow (21)

By using the measured angles and dimensions of the flow, as well as utilizing the NASA oblique shocks calculator (22), Table 14 was constructed.

Table 14. Flow properties for Shock Diamond expansions and oblique shocks

	M _{in}	M _{out}	A/A*	P _{out} /P _{in}	Shock Angle (deg)	Pressure Ratios
Expansion	1.000	1.903	1.702	0.277		P ₁ /P _{th}
Oblique Shock	1.903	1.672		1.446	38.540	P ₂ /P ₁
Expansion	1.672	1.707	1.416	0.946		P ₃ /P ₂
Oblique Shock	1.707	1.547		1.276	40.928	P ₄ /P ₃
Expansion	1.547	1.566	1.263	0.972		P ₅ /P ₄
Oblique Shock	1.566	1.445		1.179	43.780	P _{amb} /P ₅

Area ratios were determined by assuming that the jet boundary expanded isentropically. The isentropic assumption also allowed for the pressure ratios across the expansion to be calculated from isentropic relations found in Mattingly (18) using Eq. 5.

$$\frac{P_1}{P_2} = \left(\frac{1 + \frac{\gamma-1}{2} M_2^2}{1 + \frac{\gamma-1}{2} M_1^2} \right)^{\frac{\gamma}{\gamma-1}} \quad (5)$$

The value for γ was assumed to be 1.2 because of the hot exhaust gases of the RDE and the use of hydrogen as fuel. The pressure ratio P_{th}/P_{amb} was calculated to be 1.8 by multiplying all of the pressure ratios together from the individual expansions and oblique shocks. This value is an approximation because only three of the five shock diamonds were able to be accurately resolved from the high speed camera footage to determine the angles and dimensions. Because not all of the shock diamonds could be analyzed, it was predicted that the throat-to-ambient pressure ratio would be greater than 1.8.

Appendix D. Catastrophic Failure Data

Fuel Establishing Time- 0.09 sec

Air Establishing Time- 2.5 sec

Fuel Operating Time- 1.75 sec

Air Operating Time- 2.0 sec

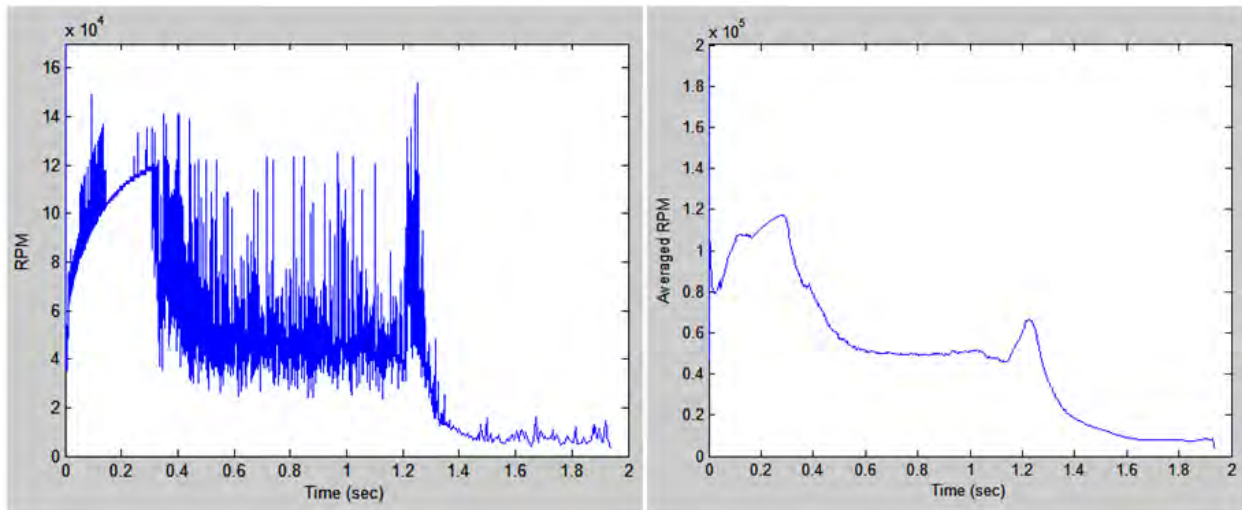


Figure 83. RPM data and 150 point moving average of RPM data for turbine catastrophic failure

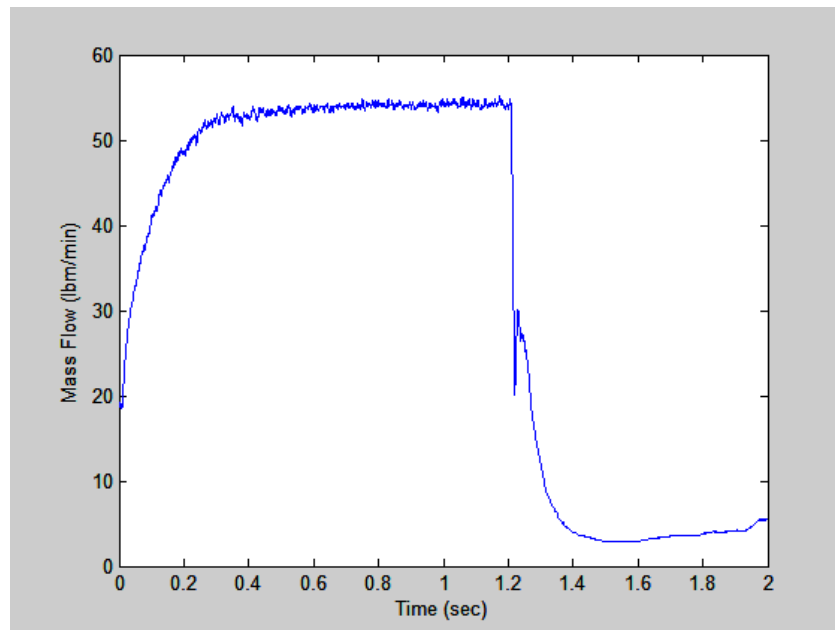


Figure 84. Compressor mass flow rate for turbine catastrophic failure

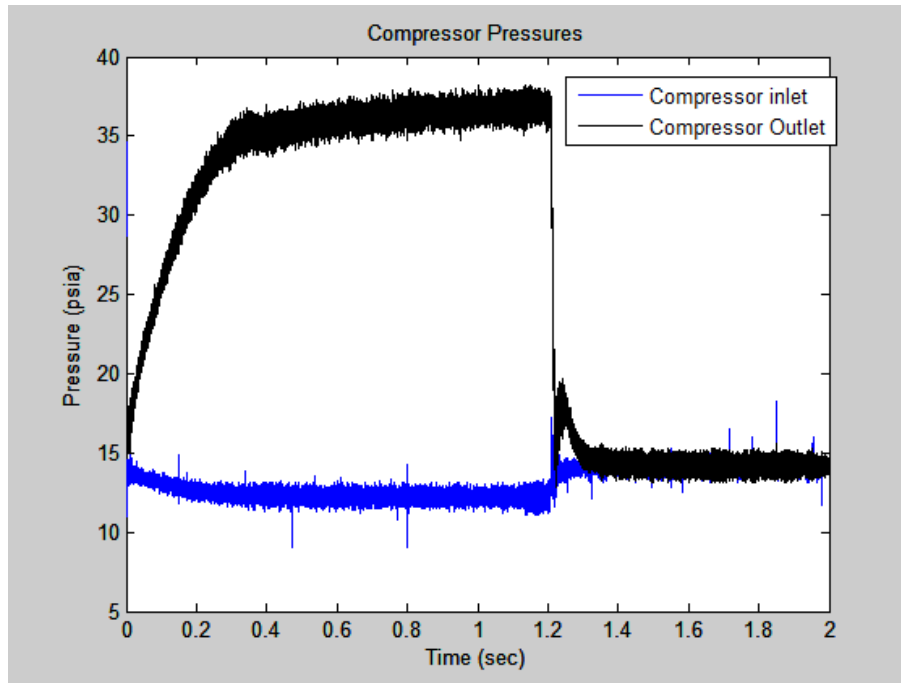


Figure 85. Compressor inlet and outlet pressures for turbine catastrophic failure

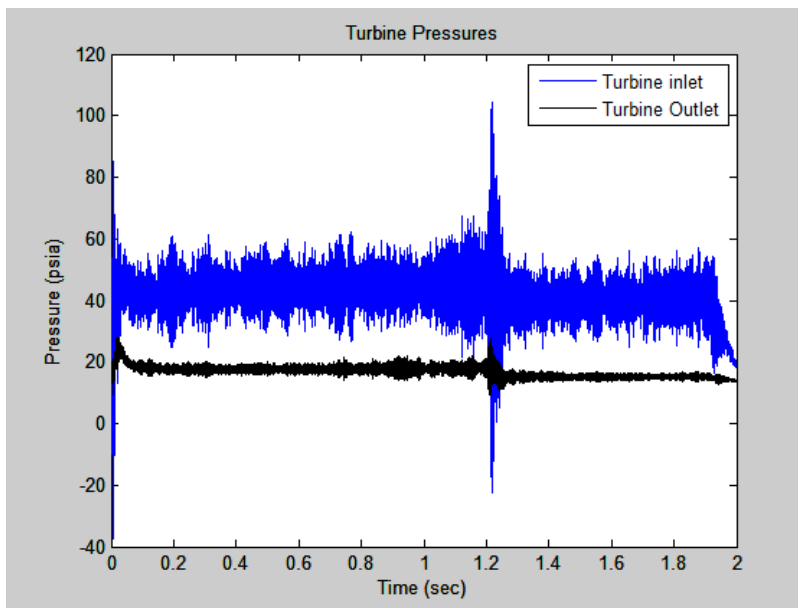


Figure 86. Turbine inlet and outlet pressures for turbine catastrophic failure

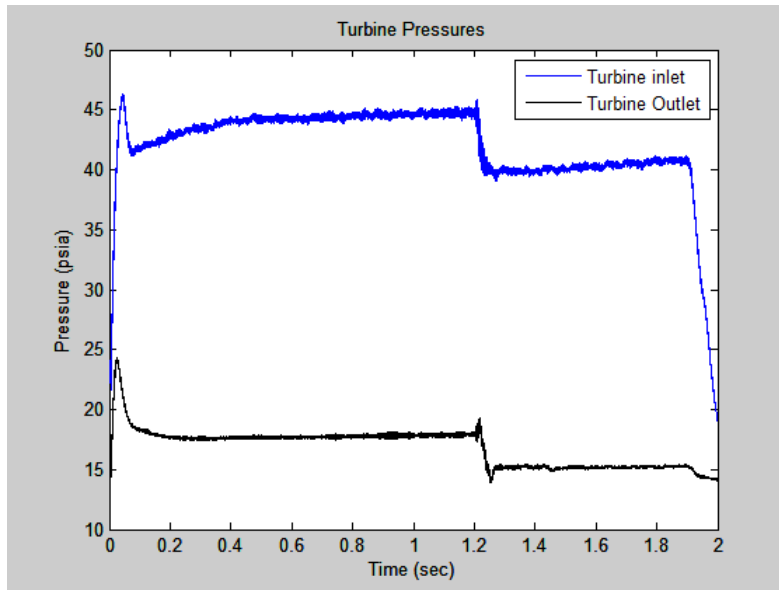


Figure 87. Averaged Turbine inlet and outlet pressures for turbine catastrophic failure

All of the data makes a sharp change at a little over 1.2 seconds into the run. All pressures decrease and the compressor mass flow rate drops nearly to zero immediately upon turbine failure because the compressor was free spinning and could not perform any work on the flow.

The time between runs was adjusted to cool the turbine in order to avoid thermal expansion of the turbine blades. The turbine inlet temperature at the beginning of every run is shown in Figure 88, where run 1 was the first run of the day and run 25 was the catastrophic failure run.

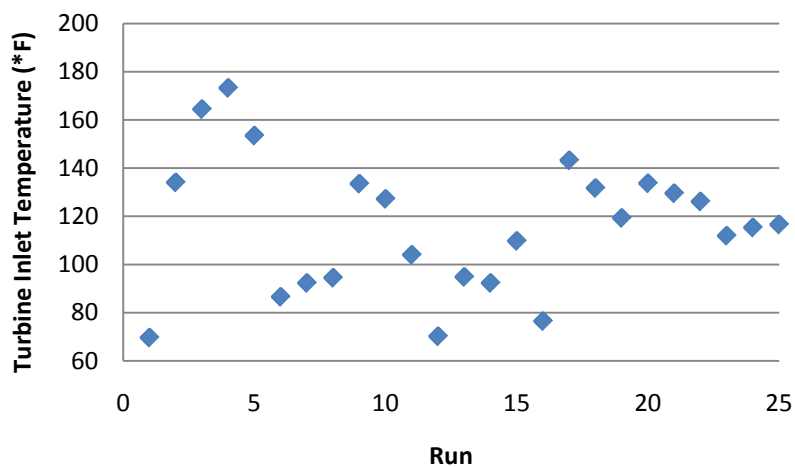


Figure 88. Initial turbine inlet temperature for every run conducted on the day of the catastrophic failure

All initial temperatures resided below 200 °F, indicating that the time allowed between each run allowed cooling of the turbine inlet temperature.

Appendix E. Thermocouple Data

Thermocouple data was taken using 1/8 in. diameter, grounded K type thermocouples in the turbine inlet and outlet, and 1/8 in. diameter, grounded T type thermocouples in the compressor inlet and outlet. The DaqView® program was used to take the thermocouple data, and the data was taken at 100 Hz for every run. For the one second runs, the thermocouples did not have enough time to reach a steady state value, and therefore the thermocouple data could not be used for testing. This is clearly seen in Figure 89, which shows the turbine inlet temperatures for all runs. The temperatures for the 2 second runs are substantially higher (>20%) than the thermocouple data from the 1 second runs, revealing that the thermocouple response time was not fast enough to capture the temperatures at the turbine inlet and outlet. Because the thermocouple response was not fast enough, no analysis, such as power or efficiency calculations were performed using the turbine temperature data.

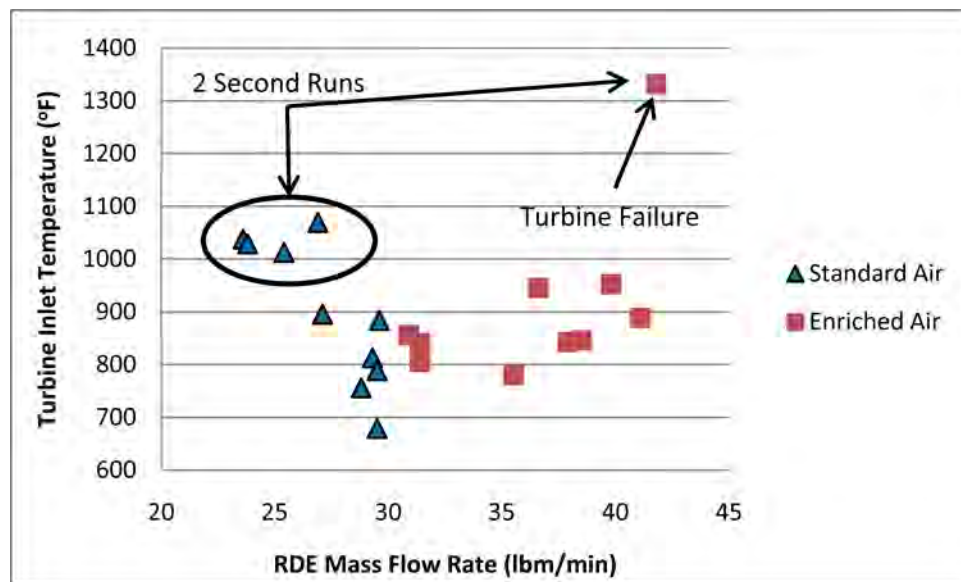


Figure 89. Maximum turbine inlet temperature reading for 1 and 2 second turbine runs using both standard and enriched air

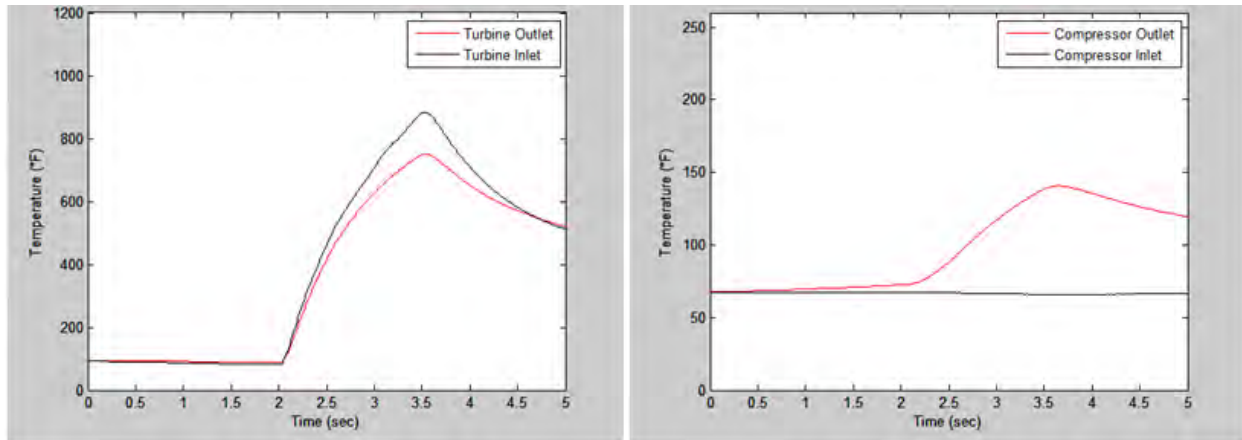


Figure 90. Compressor and turbine inlet and outlet temperatures for a 1 second, standard air run at $\dot{m}=23.8$ lbm/min and $\phi=1.37$

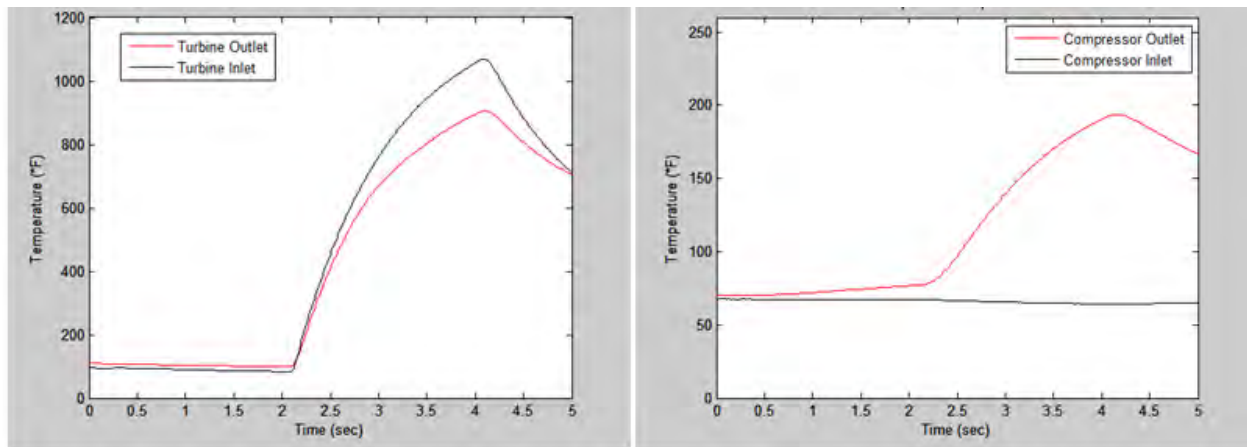


Figure 91. Compressor and turbine inlet and outlet temperatures for a 2 second, standard air run at $\dot{m}=28.5$ lbm/min and $\phi=1.47$

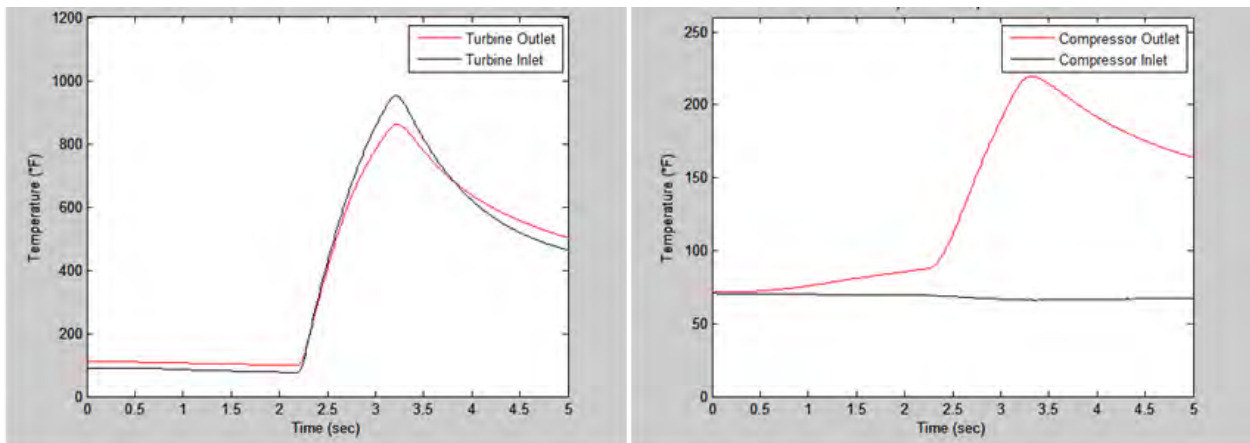


Figure 92. Compressor and turbine inlet and outlet temperatures for a 1 second, enriched air run at $\dot{m}=39.8$ lbm/min and $\phi=1.38$

Appendix F. Test Matrices

Table 15. Kulite data test matrix for 1.5 in. nozzle testing

Total Mass Flow Rate (lbm/min)	Equivalence Ratio	Average Wave Speed (m/s)	Average Combustion Speed (m/s)	Average Detonation Speed (m/s)
42.7	1.35	1304	790	1307.7
44.8	1.26	1286.1	800.86	1292.2
44.6	1.22	1265.7	701.28	1270.7
46.4	1	1198.7	721.97	1210
46.4	1.08	1248.4	747.65	1254.9
46.1	1.07	1237.5	780.45	1243.4
46	1.07	1225.7	712.87	1233.8
45.6	0.83	1182.9	671.77	1202.2
45.4	0.74	1148.2	672.6	1191.9
46.4	1.16	1233.7	531.47	1266.6
46	1.13	1218.3	512.298	1260.4
46.6	1.12	1251.6	786.64	1257.5
48.5	1.02	1220.4	815.897	1228.5
48.3	0.97	387.04	205.88	1556.3
48.2	0.94	1215.7	733.77	1226.6
48.3	0.91	607.745	330.46	1388.6
48.4	0.88	1121.5	455.75	1218.2
48.3	0.87	1196.3	803.78	1204.8
48.4	0.8	1180.8	740.37	1190.2
47.9	0.77	1167	740.84	1189.9
48.2	0.74	1144	714.128	1188.6

Table 16. PCB data test matrix for 1.5 in. nozzle testing

Total Mass Flow Rate (lbm/min)	Equivalence Ratio	Average Wave Speed (m/s)	Average Combustion Speed (m/s)	Average Detonation Speed (m/s)
42.70	1.35	1304.00	790.00	1307.70
44.80	1.26	1286.10	800.86	1292.20
44.60	1.22	1265.70	701.28	1270.70
46.40	1.02	1212.50	730.40	1229.50
46.40	1.08	1247.80	651.33	1261.70
46.10	1.07	1242.00	723.07	1256.70
46.00	1.07	1242.20	698.14	1256.50
45.60	0.83	1189.50	791.72	1210.90
45.40	0.74	1172.20	794.79	1203.30
46.40	1.16	1260.40	735.58	1271.50
46.00	1.13	1256.90	756.70	1269.20
46.60	1.12	1254.30	724.54	1265.90
48.50	1.02	1234.20	753.04	1249.60
48.30	0.97	1222.30	712.51	1231.30
48.20	0.94	1215.80	734.88	1227.80
48.30	0.91	1208.10	767.57	1219.60
48.40	0.88	1201.00	744.82	1214.70
48.30	0.87	1206.30	737.46	1220.70
48.40	0.80	1188.30	731.31	1205.10
47.90	0.77	1172.90	795.18	1200.80
48.20	0.74	1169.20	819.69	1209.30
48.30	0.67	1141.80	847.37	1196.60
48.30	0.63	1149.10	844.90	1215.80
47.80	0.60	1137.80	845.97	1217.20
37.30	1.02	1201.40	835.47	1231.90
37.30	1.16	1170.30	692.76	1258.70
37.60	1.35	1101.00	627.84	1273.00
37.80	1.36	1101.00	627.84	1273.00
42.00	0.91	1183.70	817.13	1192.80
41.40	0.93	1178.60	778.20	1189.80
41.90	0.92	1182.10	843.15	1203.20
41.90	1.22	1220.90	698.74	1237.90

Table 17. PCB and average detonation channel pressure data test matrix for 1.17 in. nozzle testing

Total Mass Flow Rate (lbm/min)	Equivalence Ratio	Average Wave Speed (m/s)	Average Combustion Speed (m/s)	Average Detonation Speed (m/s)	Detonation Channel Pressure (psia)
44.8	1.14	1160	618.19	1218.10	
38.4	1.31	1158.9	600.41	1212.70	
47.1	1.25	1210.2	617.67	1241.40	
46.7	1.16	1211.2	644.27	1258.00	
47.2	1.51	1232	640.68	1249.50	96
47.8	1.52	1205	625.99	1246.40	100
41.8	1.46	1125	626.53	1243.90	74.4
40.9	0.78	1037.2	573.75	1158.40	70
42.4	1	1034.3	595.07	1175.70	82.4
42.4	1.06	965.21	579.79	1194.40	79.2
46.6	0.95	909.78	542.18	1193.20	85.6
47.2	0.96	1001.4	583.73	1199.50	88.4
36.3	1.19	964.50	570.32	1237.60	68
36.3	1.19	969.00	586.52	1237.10	64
32.4	1.27	803.67	564.38	1261.40	62
32.6	1.14	777.85	543.46	1249.40	57.6
28.7	1.31	970.29	548.60	1250.10	55.47
28.8	1.31	948.62	562.20	1241.90	
24.6	1.28	954.68	560.65	1324.20	
24.6	1.12	906.83	586.49	1398.50	
24.4	1.19	854.822	566.84	1346.90	
34.5	1.24	1036.4	589.46	1246.30	
34.5	1.03	935.19	574.30	1221.60	65
34.5	1.06	912.48	571.81	1235.40	66.5
34.9	1.46	988.22	606.98	1242.40	67.58

** Not all runs measured the detonation channel pressure**

Table 18. PCB and nozzle pressure data test matrix for 1.17 in. nozzle testing

Total Mass Flow Rate (lbm/min)	Equivalence Ratio	Average Wave Speed (m/s)	Nozzle Base Pressure (psia)	Nozzle Throat Pressure (psia)	P_{throat}/P_{amb}
34.7	1.14	1152.6	66.63	27.45	1.87
34.5	1.25	1180.2	65.35	27.56	1.87
40.5	1.4	1202.9	76.56	33.26	2.26
41.4	1.36	1198.1	75.99	32.78	2.23
41.4	1.25	1176	72.84	33.04	2.25
41.6	1.05	1154.2	73.33	34.02	2.31
41.6	1	1143	72.67	32.91	2.24
39.9	0.86	1105.7	68.38	30.75	2.09
51.5	0.7	1089.9	81.67	36.48	2.48
51.9	0.69	1091.8	81.57	36.69	2.50
51.9	0.79	1109.5	88.37	38.76	2.64
51.7	1.03	1147.6	97.20	43.32	2.95
50.8	1.05	1150	94.57	42.85	2.92
50.2	1.14	1179.3	92.39	41.20	2.80
51	1.12	1161.4	103.24	41.21	2.80
34.6	1.13	1162.9	69.57	26.88	1.83
34.3	1.15	1164.8	68.60	26.42	1.80

Table 19. PCB and RPM data for turbine testing

Equivalence Ratio	RDE Total Mass Flow Rate (lbm/min)	Average RPM	Average Wave Speed (m/s)	Average Combustion Speed (m/s)	Average Detonation Speed (m/s)
1.28	29.5	104290	1026.7	617.0623	1312.8
1.28	29.6	102970	1068.8	649.0337	1295.1
1.29	29.3	105520	1064.5	648.6944	1274.2
1.51	23.6	90415	910.2059	569.1704	1303.2
1.37	23.8	94396	934.3041	578.9663	1278.3
1.28	25.4	97235	1062.5	642.7167	1328.7
1.22	26.8	111340	995.6438	614.2527	1313.4
1.36	27.1	121740	1004	586.0916	1321.1
1.37	26.9	110840	941.8075	554.3952	1320.5
1.7	24.8	117120	971.6748	610.5967	1232.9
1.47	28.5	103780	1045.3	596.8578	1250.9
0.94	31.4	114770	1070.5	797.0797	1205
1.13	30.9	118120	1135.5	705.9122	1227.3
1.3	31.4	114730	1199.8	702.8281	1285.3
1.15	35.5	111090	1200	766.3495	1268.2
1.33	36.6	113580	1162.2	614.4929	1337.4
1.28	37.9	110980	1181.9	637.4767	1320.9
1.38	39.8	113080	1277.3	618.8786	1333.8
1.34	41.1	122230	1281	629.3633	1310.8
1.31	41.8	51931	1154.3	611.3701	1336.4

Table 20. Compressor inlet and outlet pressures, compressor mass flow rate, and turbine inlet and outlet pressure for turbine testing

Equivalence Ratio	RDE Total Mass Flow Rate (lbm/min)	Average Compressor Mass Flow Rate (lbm/min)	Average Compressor Outlet Pressure (psia)	Average Compressor Inlet Pressure (psia)	Average Turbine Outlet Pressure (psia)	Average Turbine Inlet Pressure (psia)
1.28	29.5	43.1569	28.8382	13.1544		
1.28	29.6	46.6972	20.6762	12.9365		
1.29	29.3	43.6453	27.4874	13.1427		
1.51	23.6	36.0544	22.8969	13.5173		
1.37	23.8	36.3327	22.9898	13.4959		
1.28	25.4	39.0429	24.6061	13.3772		
1.22	26.8	40.8152	25.6614	13.2859		
1.36	27.1	41.6992	25.873	13.2636		
1.37	26.9	40.5803	25.3659	13.2691		
1.7	24.8	38.6949	23.9622	13.3756	25.1116	15.1247
1.47	28.5	43.7706	27.3023	13.1127	28.9277	15.4794
0.94	31.4	45.6744	28.8389	12.9412	31.2704	15.6927
1.13	30.9	45.4891	28.9201	12.9574	30.7732	15.6952
1.3	31.4	45.9306	29.446	12.9141	31.378	15.7308
1.15	35.5	50.0467	32.6824	12.6112	36.1023	16.3085
1.33	36.6	51.6818	33.9741	12.4655	37.8733	16.5951
1.28	37.9	52.4126	34.6121	12.4044	39.0432	16.7798
1.38	39.8	53.4793	35.8554	12.2708	41.5429	17.155
1.34	41.1	53.4793	36.5465	12.2177	43.093	17.3569
1.31	41.8	54.1168	36.4009	12.2292	44.3981	17.7358

Testing for first half of data used 1/16 in. diameter, 3.5 ft length stand-off tubing for the turbine inlet and outlet pressures, which did not allow for a rapid enough response for the turbine pressures for a one second run. The stand-off tubing was switched to 1/8 in. diameter, 3.5 ft length tubing for the remainder of turbine testing.

Appendix G. Turbine Testing Data

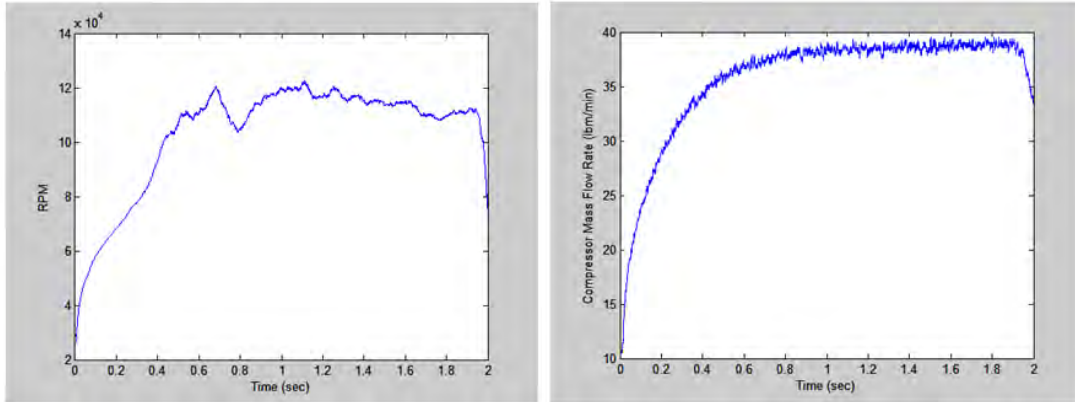


Figure 93. RPM 150 point moving average and compressor mass flow rate 100 point moving average for a 2 second, standard air run at $\dot{m}=24.8$ lbm/min and $\phi=1.7$

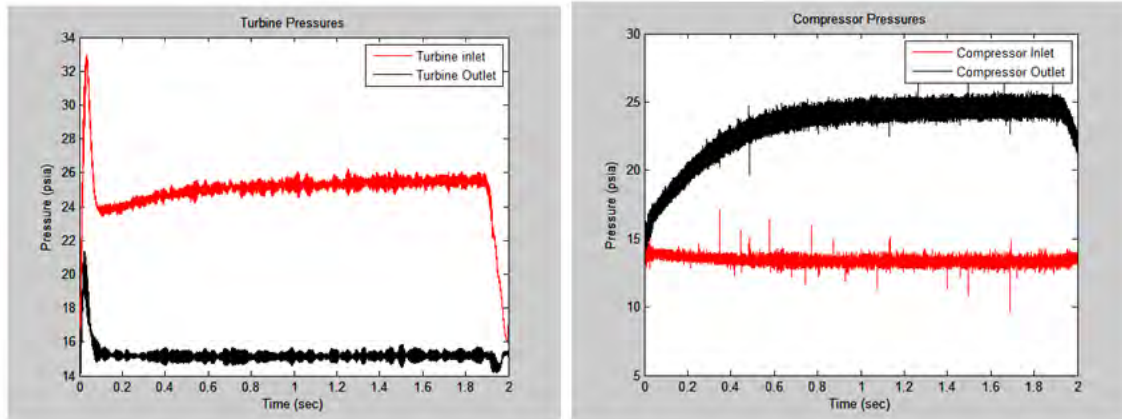


Figure 94. Compressor inlet and outlet pressures and 150 point moving average of turbine inlet and outlet pressures for a 2 second, standard air run at $\dot{m}=24.8$ lbm/min and $\phi=1.7$

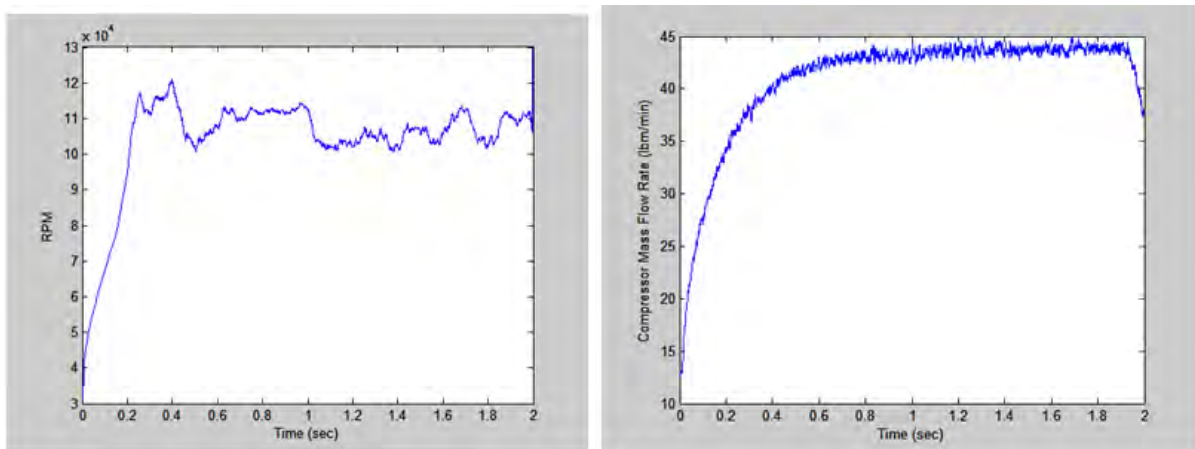


Figure 95. RPM 150 point moving average and compressor mass flow rate 100 point moving average for a 2 second, standard air run at $\dot{m}=28.5$ lbm/min and $\phi=1.47$

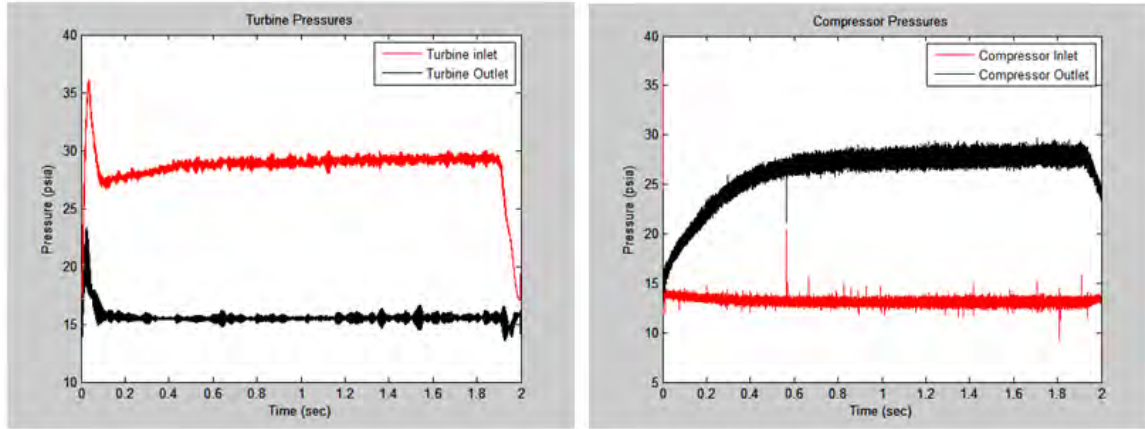


Figure 96. Compressor inlet and outlet pressures and 150 point moving average of turbine inlet and outlet pressures for a 2 second, standard air run at $\dot{m}=28.5$ lbm/min and $\phi=1.47$

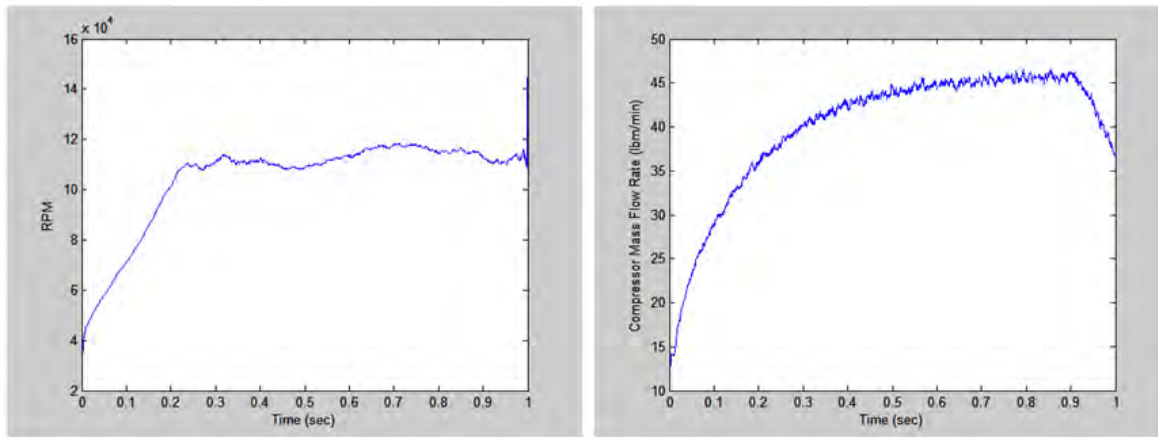


Figure 97. RPM 150 point moving average and compressor mass flow rate 100 point moving average for a 1 second, enriched air run at $\dot{m}=31.4$ lbm/min and $\phi=0.94$

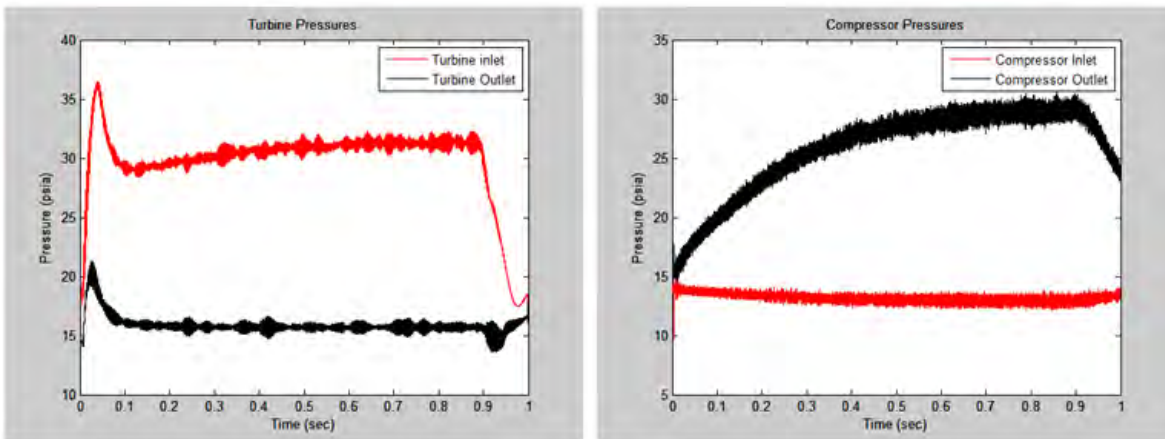


Figure 98. Compressor inlet and outlet pressures and 150 point moving average of turbine inlet and outlet pressures for a 1 second, enriched air run at $\dot{m}=31.4$ lbm/min and $\phi=0.94$

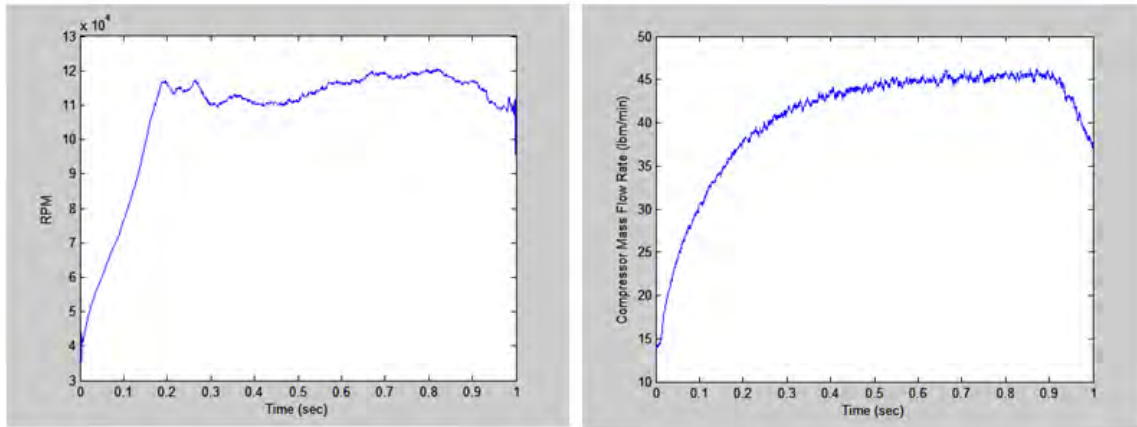


Figure 99. RPM 150 point moving average and compressor mass flow rate 100 point moving average for a 1 second, enriched air run at $\dot{m}=30.9$ lbm/min and $\phi=1.13$

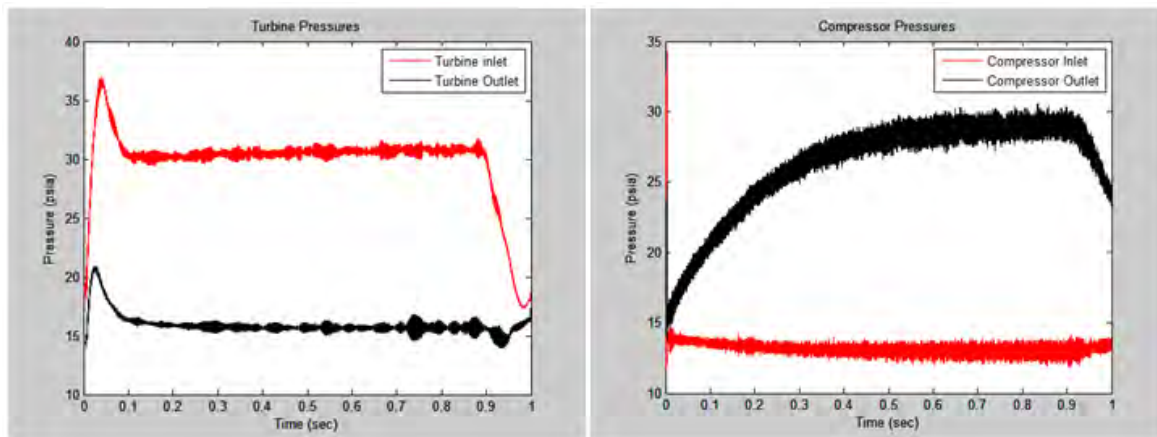


Figure 100. Compressor inlet and outlet pressures and 150 point moving average of turbine inlet and outlet pressures for a 1 second, enriched air run at $\dot{m}=30.9$ lbm/min and $\phi=1.13$

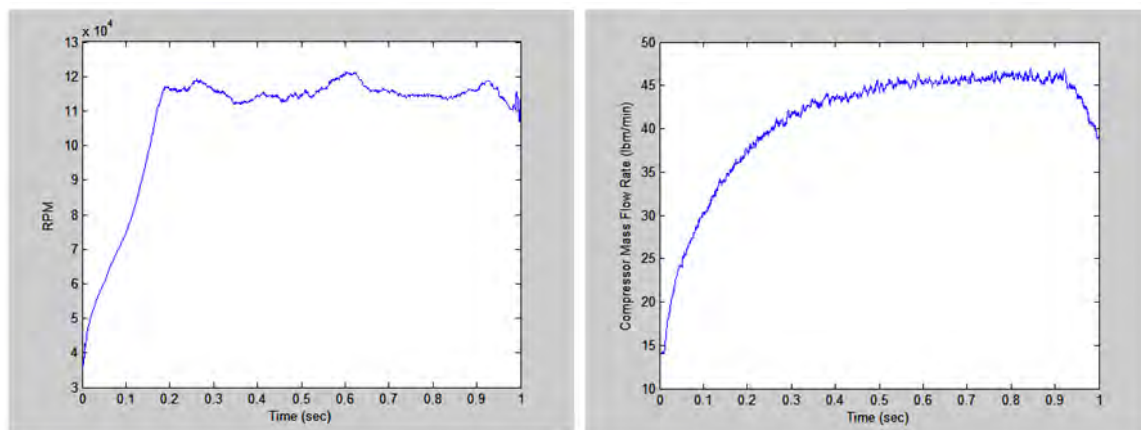


Figure 101. RPM 150 point moving average and compressor mass flow rate 100 point moving average for a 1 second, enriched air run at $\dot{m}=31.4$ lbm/min and $\phi=1.3$

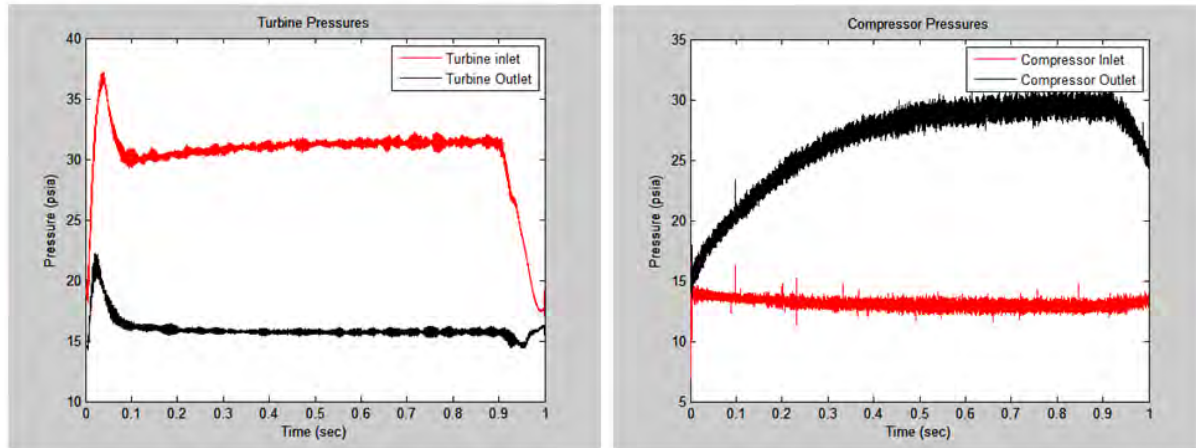


Figure 102. Compressor inlet and outlet pressures and 150 point moving average of turbine inlet and outlet pressures for a 1 second, enriched air run at $\dot{m}=31.4$ lbm/min and $\phi=1.3$

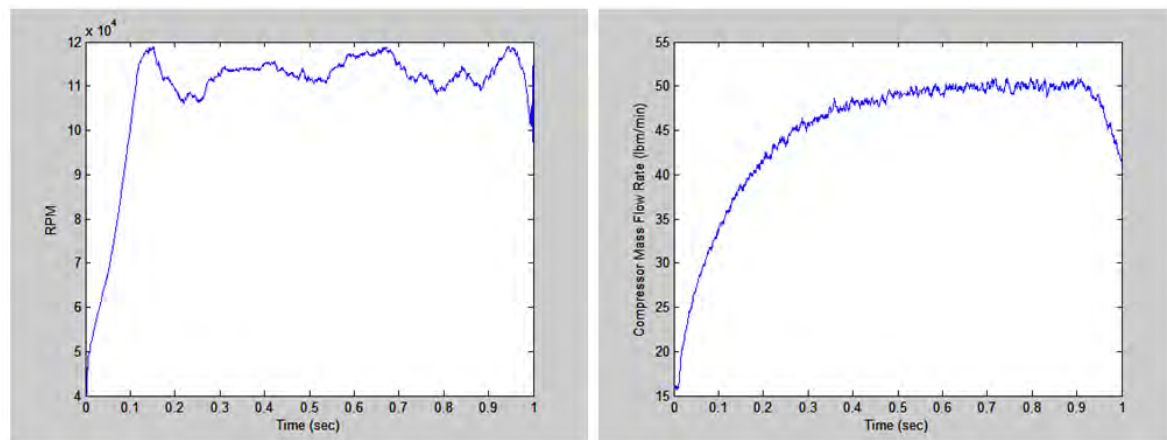


Figure 103. RPM 150 point moving average and compressor mass flow rate 100 point moving average for a 1 second, enriched air run at $\dot{m}=35.5$ lbm/min and $\phi=1.27$

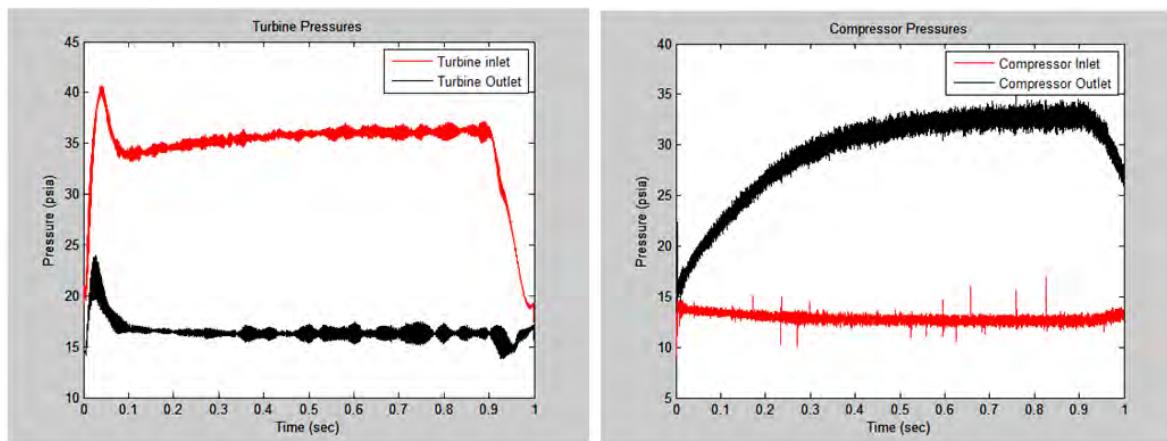


Figure 104. Compressor inlet and outlet pressures and 150 point moving average of turbine inlet and outlet pressures for a 1 second, enriched air run at $\dot{m}=35.5$ lbm/min and $\phi=1.27$

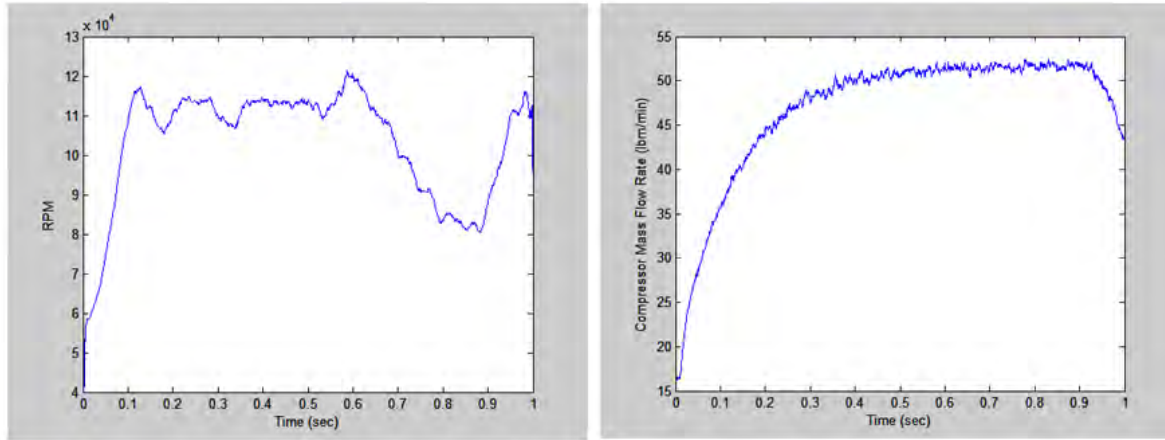


Figure 105. RPM 150 point moving average and compressor mass flow rate 100 point moving average for a 1 second, enriched air run at $\dot{m}=36.6$ lbm/min and $\phi=1.33$

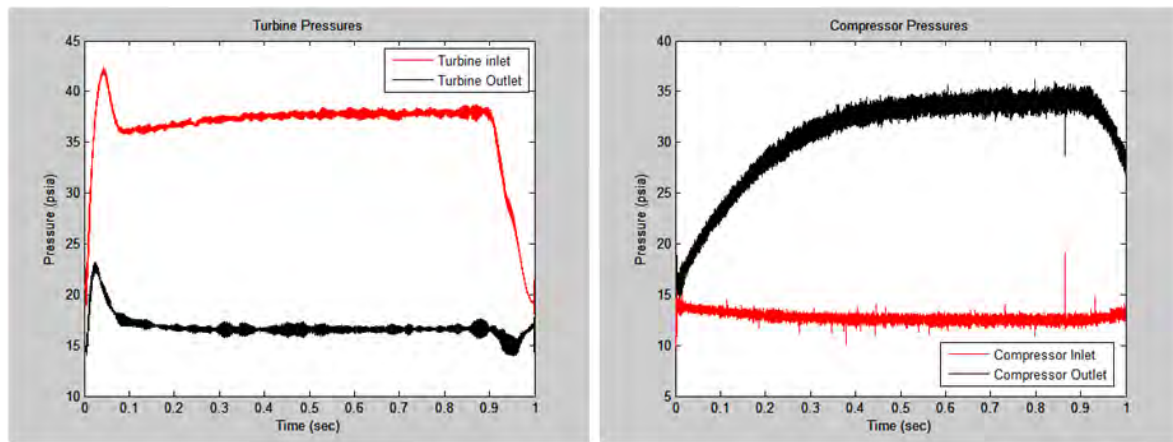


Figure 106. Compressor inlet and outlet pressures and 150 point moving average of turbine inlet and outlet pressures for a 1 second, enriched air run at $\dot{m}=36.6$ lbm/min and $\phi=1.33$

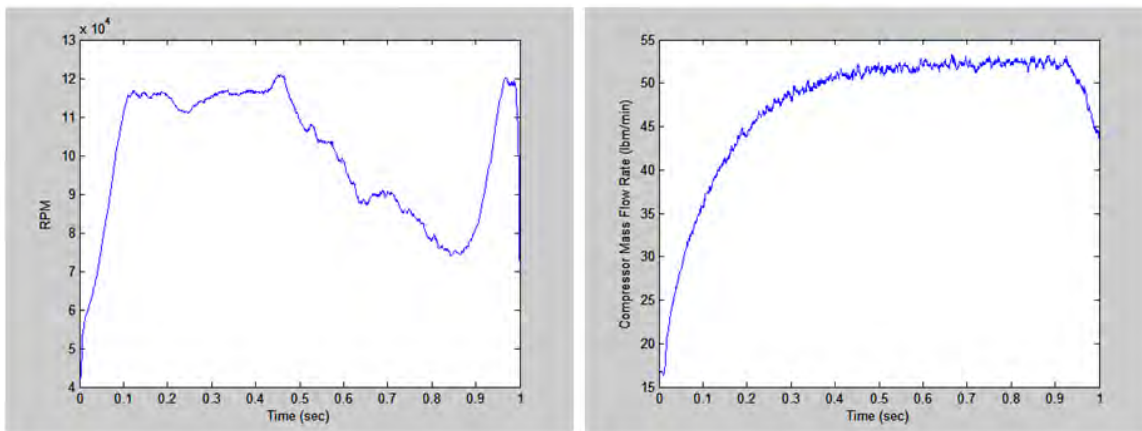


Figure 107. RPM 150 point moving average and compressor mass flow rate 100 point moving average for a 1 second, enriched air run at $\dot{m}=37.9$ lbm/min and $\phi=1.28$

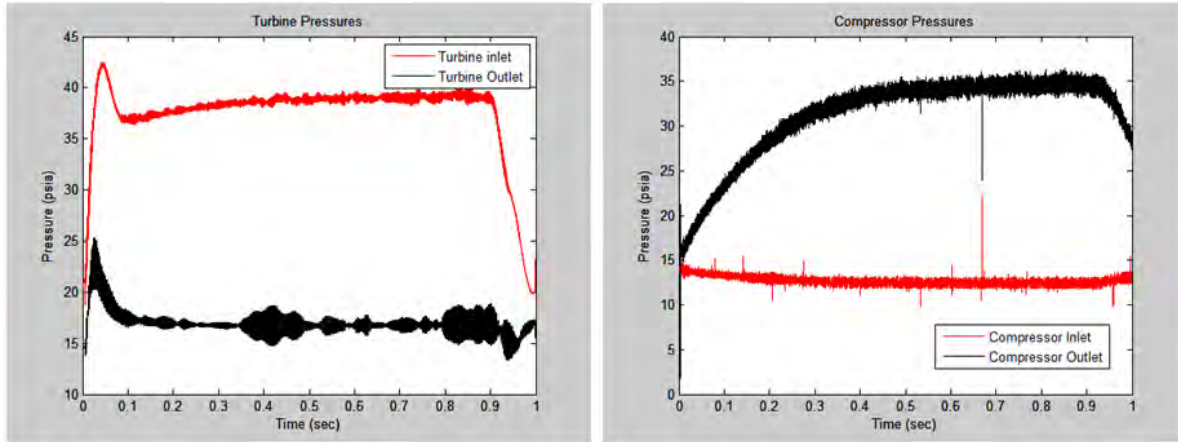


Figure 108. Compressor inlet and outlet pressures and 150 point moving average of turbine inlet and outlet pressures for a 1 second, enriched air run at $\dot{m}=37.9$ lbm/min and $\phi=1.28$

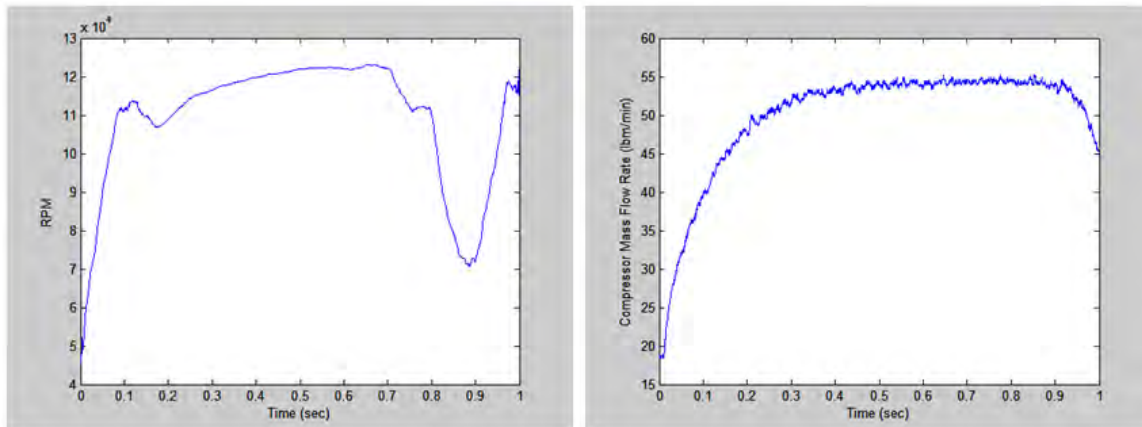


Figure 109. RPM 150 point moving average and compressor mass flow rate 100 point moving average for a 1 second, enriched air run at $\dot{m}=41.1$ lbm/min and $\phi=1.34$

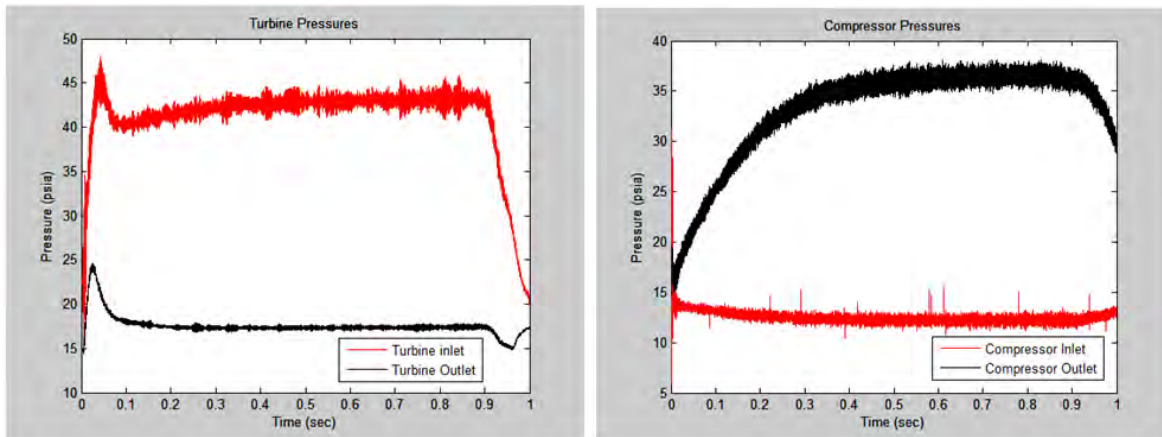


Figure 110. Compressor inlet and outlet pressures and 150 point moving average of turbine inlet and outlet pressures for a 1 second, enriched air run at $\dot{m}=41.1$ lbm/min and $\phi=1.34$

References

1. Turns, Stephen R. *An Introduction to Combustion: Concepts and Applications*. Boston : McGraw-Hill, 2006.
2. Russo, Rachel M. *Operational Characteristics of a Rotating Detonation Engine using Hyrdrogen and Air*. AFIT/GAE/ENY/11-J03. Department of Aeronautics and Astronautics, Air Force Institute of Technology (AU), WPAFB, OH, June 2011.
3. Petters, D. and Felders, J. "Engine System Performance of Pulsed Detonation Concepts Using the NPSS Program," 38th AIAA/ASME/SAE/ASEE Joint Propulsion Conference and Exhibit, AIAA 2002-3910. Indianapolis, IN: 2002.
4. Schauer, Fred, Bradley, Royce and Hoke, John. "Interaction of a Pulsed Detonation Engine with a Turbine," 41st Aerospace Sciences Meeting and Exhibit. AIAA 2003-0891. Reno, NV: 2003.
5. Glaser, Aaron J, Caldwell, Nicholas and Gutmark, Ephraim. "Performance of an Axial Flow Turbine Driven by Multiple Pulse Detonation Combustors," 45th AIAA Aerospace Sciences Meeting and Exhibit. AIAA 2007-1244. Reno, NV :2007.
6. Thomas, Levi M, et al. "Buildup and Operation of a Rotating Detonation Engine," 49th AIAA Aerospace Sciences Meeting. AIAA 2011-0602. Orlando, FL : 2011.
7. Schauer, Fred, et al. "Integration of a Pulsed Detonation Engine with an Ejector Pump and with a Turbo-Charger as Methods to Self-Aspirate," 40th AIAA Aerospace Sciences Meeting. AIAA 2002-0615. Reno, NV : 2002.
8. Caldwell, Nicholas, Glaser, Aaron and Gutmark, Ephraim. "Performance Measurements of a Pulsed Detonation Engine Array Integrated with a Turbine," 42nd AIAA/ASME/SAE/ASEE Joint Propulsion Conference and Exhibit. AIAA 2006-4307. Sacramento, CA: 2006.
9. Glaser, Aaron J, Caldwell, Nicholas and Gutmark, Ephraim. "Performance Measurements of a Pulse Detonation Combustor Array Integrated with an Axial Flow Turbine," 44th AIAA Aerospace Sciences Meeting. AIAA 2006-1232. Reno, NV: 2006.
10. Rouser, Kurt P, et al. "Parametric Study of Unsteady Turbine Performance Driven by a Pulse Detonation Combustor," 46th AIAA/ASME/SAE/ASEE Joint Propulsion Conference and Exhibit. AIAA 2010-6536. Nashville, TN: 2010.
11. Rouser, Kurt, et al. "Unseady Performance of a Turbine Driven by a Pulse Detonation Engine," 48th AIAA Aerospace Sciences Meeting. AIAA 2010-1116. Orlando, FL: 2010.

12. Braun, Eric M, et al. "Airbreathing Rotating Detonation Wave Engine Cycle Analysis," 46th AIAA/ASME/SAE/ASEE Joint Propulsion Conference and Exhibit. AIAA 2010-7039. Nashville, TN: 2010.
13. Suchocki, James A. *Operational Space and Characterization of a Rotating Detonation Engine Using Hydrogen and Air*. Graduate Program in Mechanical Engineering, Ohio State University, Columbus, OH, January 2012.
14. Shao, Yetao, Meng, Liu and Jianping, Wang. "Continuous Detonation Engine and Effects of Different Types of Nozzle on Its Propulsion Performance," *Chines Journal of Aeronautics*, 23:647-652 (August 2010)
15. Bykovskii, F. A., Zhdan, S. A. and Vedernikov. "Continuous Spin Detonation of Fuel-Air Mixtures," *Combustion, Explosion, and Shock Waves*, 42:463-41 (June 2005)
16. Lee, John H.S., Knystautas, R. and Freiman, A. "High Speed Turbulent Deflagrations and Transition to Detonation in H₂-Air Mixtures," *Combustion and Flame*, 56:870-881 (December 1983)
17. Karnesky, James, et al. "Pulsed Detonation Engines in the Choked Flame Regime," 50th AIAA Aerospace Sciences Meeting. AIAA 2012-0616. Nashville, TN: 2012.
18. Mattingly, Jack, and Ohain, H. von. *Elements of Propulsion: Gas Turbines and Rockets*. Reston, VA: AIAA, 2006.
19. Wheeler, Anthony J and Ganji, Ahmad R. *Introduction to Engineering Experimentation*. Upper Saddle River, NJ : Pearson Education, Inc., 2004.
20. Mattingly, Jack D., Heiser, William H. and Pratt, David T. *Aircraft Engine Design*. Reston, VA: AIAA, 2002.
21. Scott, Jeff. "Shock Diamonds and Mach Disks." Excerpt from unpublished article. n. pag. <http://www.aerospaceweb.org/question/propulsion/q0224.shtml>
22. Shock Modeler, Software Package, Ver. 1.3a, NASA Glenn Research Center, Cleveland, OH, 2011. <http://www.grc.nasa.gov/WWW/k-12/airplane/mshock.html>

REPORT DOCUMENTATION PAGE			Form Approved OMB No. 0704-0188	
The public reporting burden for this collection of information is estimated to average 1 hour per response, including the time for reviewing instructions, searching existing data sources, gathering and maintaining the data needed, and completing and reviewing the collection of information. Send comments regarding this burden estimate or any other aspect of this collection of information, including suggestions for reducing this burden to Department of Defense, Washington Headquarters Services, Directorate for Information Operations and Reports (0704-0188), 1215 Jefferson Davis Highway, Suite 1204, Arlington, VA 22202-4302. Respondents should be aware that notwithstanding any other provision of law, no person shall be subject to any penalty for failing to comply with a collection of information if it does not display a currently valid OMB control number. PLEASE DO NOT RETURN YOUR FORM TO THE ABOVE ADDRESS.				
1. REPORT DATE (DD-MM-YYYY) 22-03-2012		2. REPORT TYPE Master's Thesis		3. DATES COVERED (From — To) Oct 2010- Mar 2012
4. TITLE AND SUBTITLE Build Up and Operation of an Axial Turbine Driven by a Rotary Detonation Engine			5a. CONTRACT NUMBER	
			5b. GRANT NUMBER	
			5c. PROGRAM ELEMENT NUMBER	
6. AUTHOR(S) Jonathan R. Tellefsen, 2d Lt, USAF			5d. PROJECT NUMBER	
			5e. TASK NUMBER	
			5f. WORK UNIT NUMBER	
7. PERFORMING ORGANIZATION NAME(S) AND ADDRESS(ES) Air Force Institute of Technology Graduate School of Engineering and Management (AFIT/ENY) 2950 Hobson Way WPAFB OH 45433-7765			8. PERFORMING ORGANIZATION REPORT NUMBER AFIT/GAE/ENY/12-M39	
9. SPONSORING / MONITORING AGENCY NAME(S) AND ADDRESS(ES) Attn: Dr. Frederick Schauer Air Force Research Laboratory Propulsion Directorate, Turbine Engine Division, Combustion Branch Bldg 71A, D-Bay 7 th St. Wright Patterson AFB, OH 45433-7251 DSN 785-6462. Frederick.schauer@wpafb.af.mil			10. SPONSOR/MONITOR'S ACRONYM(S) AFRL/RZTC	
			11. SPONSOR/MONITOR'S REPORT NUMBER(S)	
12. DISTRIBUTION / AVAILABILITY STATEMENT APPROVED FOR PUBLIC RELEASE; DISTRIBUTION UNLIMITED				
13. SUPPLEMENTARY NOTES This material is declared a work of the U.S. Government and is not subject to copyright protection in the United States.				
14. ABSTRACT Detonation combustors provide advantages over current deflagration combustors due to their pressure gain and simplicity of design. Rotary detonation engines (RDEs) offer advantages over pulsed detonation engines (PDEs) due to a steadier exhaust and fewer total system losses. All previous research on turbine integration with detonation combustors has focused on utilizing PDEs to drive axial and centrifugal turbines. The objective of this thesis was the integration and testing of an axial turbine driven by a rotary detonation engine (RDE) to determine turbine operability. In pursuit of this objective, convergent nozzle sections were placed on the RDE to simulate the back-pressurization that would occur when placing the turbine behind the RDE. Nozzle testing showed that back-pressurizing the RDE increases the operational space of the RDE. Results from the nozzle testing were used to properly integrate the turbine with the RDE. The turbine was driven by the RDE with successful detonation runs, showing turbine operation with RDEs is possible. The RDE operated similarly for both nozzle and turbine testing, demonstrating that a nozzle can properly simulate the presence of a turbine behind a RDE.				
15. SUBJECT TERMS Rotary, Detonation, Engine, Turbine, JetCat, Nozzle,				
16. SECURITY CLASSIFICATION OF: Unclassified			17. LIMITATION OF ABSTRACT UU	18. NUMBER OF PAGES 146
a. REPORT U	b. ABSTRACT U	c. THIS PAGE U		

Standard Form 298 (Rev. 8-98)
Prescribed by ANSI Std. Z39.18